Grant Agreement N°763990

UPWARDS

Deliverable D5.3

Unified fatigue damage model and software implementation in SAMCEF

WP	5	Material failure models
Task	5.3	Unified fatigue damage model (inter- and intra-laminar) including interaction criteria between damage modes

Dissemination level[1]	PU	**Due delivery date**	30/09/2020 (31/04/2021)
Nature[2]	R	**Actual delivery date**	15/05/2021

Lead beneficiary	**Aalborg University**
Contributing beneficiaries	SAMTECH SA

Document Version	**Date**	**Author**	**Comments**[3]
1	31/04/2021	Laura Carreras (AAU), Brian Bak (AAU), Esben Lindgaard (AAU), Cédric Lequesne (SAMCEF), Hu Xiong (SAMCEF)	Creation

[1] Dissemination level: **PU** = Public, **PP** = Restricted to other programme participants (including the JU), **RE** = Restricted to a group specified by the consortium (including the JU), **CO** = Confidential, only for members of the consortium (including the JU)

[2] Nature of the deliverable: **R** = Report, **P** = Prototype, **D** = Demonstrator, **O** = Other

[3] Creation, modification, final version for evaluation, revised version following evaluation, final

Deliverable abstract

Laminated composite materials are used extensively in wind turbine blades due to their high mechanical performances and good fatigue resistance compared to metals. However, the occurring damage mechanisms are more complex in composite materials due to anisotropy, heterogeneity and defects (due to their nature but also due to the manufacturing process). In order to be able to design safe structures made of composite materials, understanding and predicting the occurrence of damage events and their interplay is essential. This work focusses on the interaction between damage mechanisms occurring at the intra- and inter-laminar regions of the laminate under both static and fatigue loading. A dedicated formulation is developed in order to initiate delamination (inter-laminar damage) from matrix cracking (intra-laminar damage) in the numerical framework implemented in the Simcenter Samcef solver. To this end, the inter- and intra-laminar damage models presented in tasks 5.1 and 5.2 are coupled and synchronized in terms of fatigue cycles. The unified numerical tool is employed to exemplify the predicted mechanical behaviour in an open hole specimen. The results show that the interfacial stiffness is reduced to zero at the regions with high intra-laminar damage, thus modelling a delamination caused by the coalescence of micro-delaminations arising at the crack tips of transverse matrix cracks.

Deliverable Review

	Reviewer #1: /Coordinator			Reviewer #2:		
	Answer	**Comments**	**Type***	**Answer**	**Comments**	**Type***
1. Is the deliverable in accordance with						
(i) The Description of Work?	☒ Yes ☐ No		☐ M ☐ m ☐ a	☐ Yes ☐ No		☐ M ☐ m ☐ a
(ii) The international State of the Art?	☐ Yes ☐ No	*Not applicable for this deliverable*	☐ M ☐ m ☐ a	☐ Yes ☐ No	*Not applicable for this deliverable*	☐ M ☐ m ☐ a
2. Is the quality of the deliverable in a status						
(i) That allows it to be sent to European Commission?	☒ Yes ☐ No		☐ M ☐ m ☐ a	☐ Yes ☐ No		☐ M ☐ m ☐ a
(ii) That needs improvement of the writing by the originator of the deliverable?	☐ Yes ☒ No		☐ M ☐ m ☐ a	☐ Yes ☐ No		☐ M ☐ m ☐ a
(iii) That needs further work by the Partners responsible for the deliverable?	☐ Yes ☒ No		☐ M ☐ m ☐ a	☐ Yes ☐ No		☐ M ☐ m ☐ a

* Type of comments: M = Major comment; m = minor comment; a = advice

Table of Contents

1 Introduction 4
1.1 Background 6
1.2 Objectives 7
2 Theoretical framework 8
2.1 The physical problem 8
2.2 Existing modelling strategies 9
2.3 Summary of the intra-laminar fatigue damage model implemented in Simcenter Samcef 12
2.3.1 Behaviour law 13
2.3.2 Fatigue failure indices 14
2.3.3 Evolution law of the fatigue damage in a unidirectional ply 16
2.4 Summary of the inter-laminar damage model implemented in Simcenter Samcef 17
2.4.1 Evolution law of the fatigue damage at the interface 18
3 Experimental observations from Task 5.2 20
4 Unified model intra- and inter- laminar damage 25
4.1 Objective 25
4.2 Interaction criterion 26
5 Implementation into Simcenter Samcef 29
5.1 Communication of intra-laminar damage to interface element 29
5.2 Integration of the behavior law 29
5.3 Keywords 30
5.4 Post processing 31
5.5 Shared cycle jump strategy 31
6 Numerical case studies 34
6.1 Unit Test 34
6.2 Open hole tensile test 39
7 Conclusions 59
8 References 60

1 Introduction

Failure in laminated composites is usually caused by inter-laminar fractures, such as delamination or adhesive joint debonding, promoted by or coexisting with intra-laminar damage mechanisms, like matrix cracking and fibre failure (see Figure 1-1).

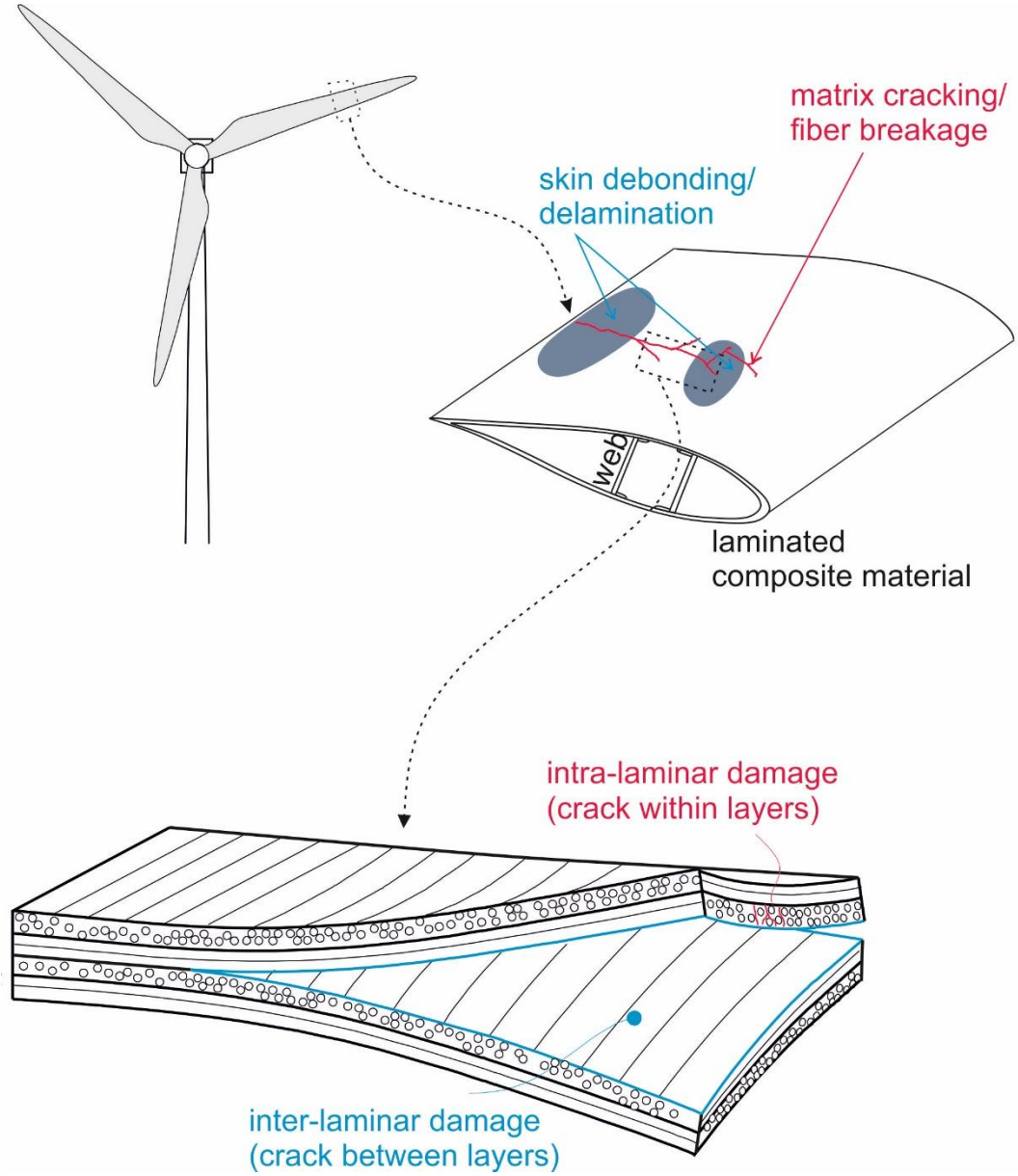

Figure 1-1. Inter-laminar and intra-laminar damage in wind turbine blades made of a laminated composite material.

Fatigue failure prediction, despite of being crucial for an a safe and efficient design, an accurate assessment of the service life of composite structures and as a planning tool for maintenance actions, remains far from mature. The interaction between different failure mechanisms and the complexity of realistic loading spectra, spanning with varying amplitude and frequency, is currently not possible to predict with the state-of-the-art material damage models. The objectives of WP5 are the development of (i) progressive material damage models for both inter- and intra-laminar fracture and (ii) simulation tools for static and fatigue-driven damage development in laminated composite wind turbine blades in order to evaluate the structural performance and integrity.

First, independent inter- (T5.1) and intra-laminar (T5.2) fatigue damage models are developed. Then, a unified numerical framework is implemented in the Simcenter Samcef solver, including interaction

between both models (T5.3). Then, the effect of fatigue loading history on damage development is studied and incorporated in the numerical tool (T5.4). Finally, the method is validated against experimental testing on a wind turbine (WT) blade substructure (T5.5). The described workflow is illustrated in Figure 1-2.

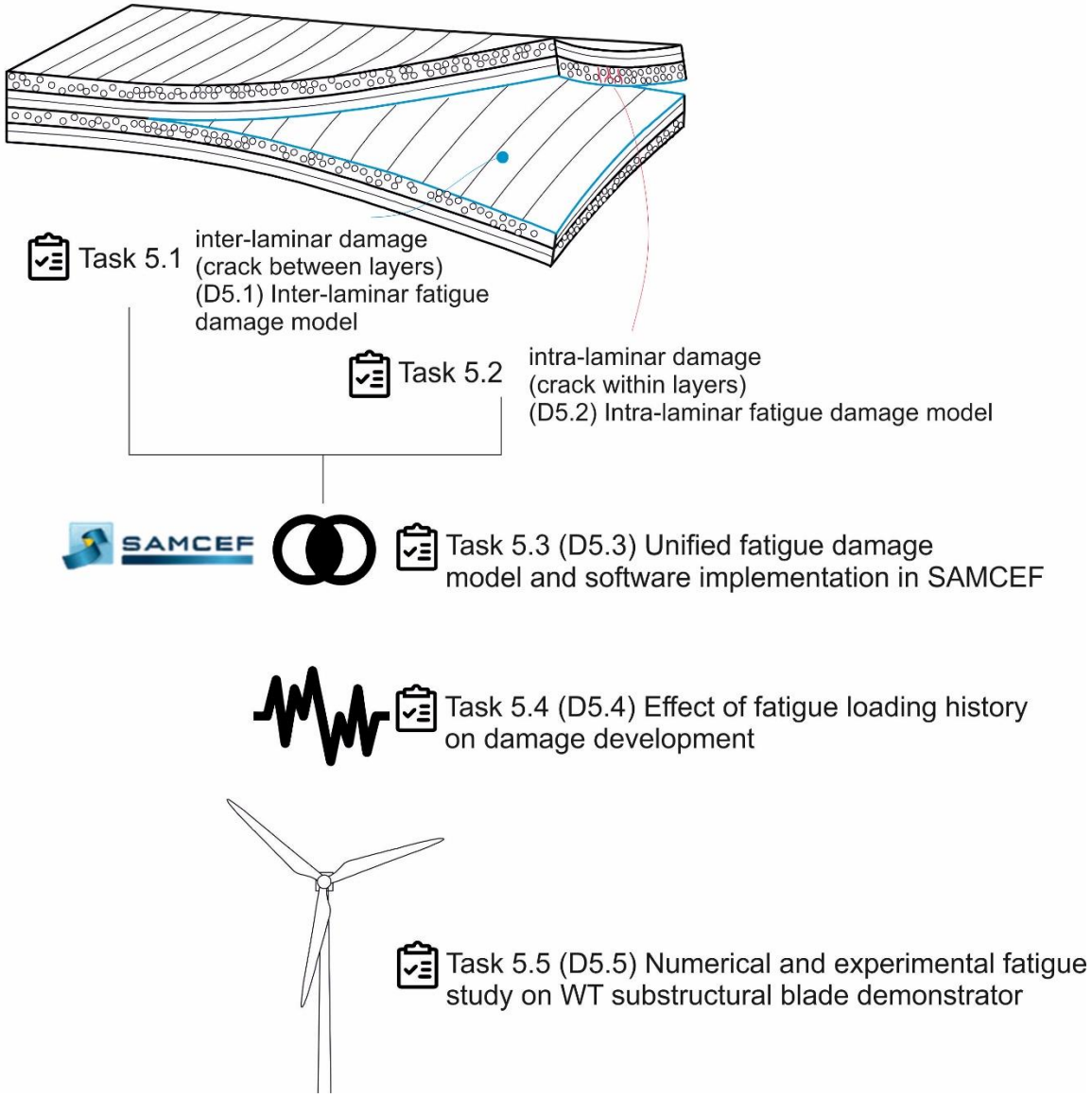

Figure 1-2. Overview of tasks in work package WP5.

This document describes the work carried out in Task 5.3 about the development of an interaction criterion between the inter- and intra-laminar progressive fatigue damage models developed and implemented in Task 5.1 and Task 5.2, respectively. First, inspiration from the current state-of-the-art is sought. In order to focus on the material system used in the UPWARDS project, the results of the tests carried out in Task 5.2 are revisited. The occurrence of delamination (inter-laminar damage) triggered by the accumulation of intra-laminar damage (mainly matrix cracking) is observed. Based on the experimental evidences, the objectives of the interaction are set: the development of damage within the ply should lead to the initiation of damage at the neighbouring interfaces. A criterion to capture this sequence of damage occurrence with the modelling framework implemented in the Simcenter Samcef solver is developed. In addition, a shared cycle jump strategy with the purpose to synchronize the number of fatigue cycles simulated by both models is designed.

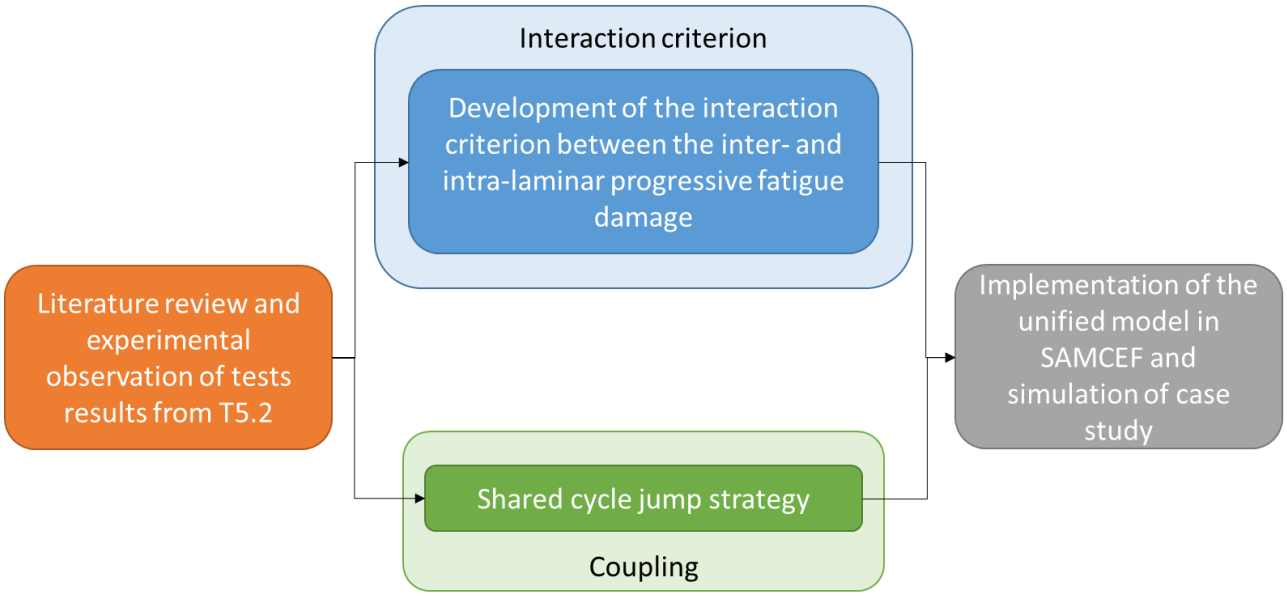

Figure 1-3. Workflow in Task 5.3.

This deliverable D5.3 is structured as follows: In Section 1.1, the background and what this study proposes to accomplish is described. In Section 1.2, the specific objectives of this deliverable are outlined. In Section 2.1, the physical problem of the interaction between different damage mechanisms is described. In Section 2.2, the existing modelling strategies in the literature are reviewed. In sections 2.3 and 2.4, the main points from the inter- and intra-laminar models presented in tasks 5.1 and 5.2, respectively, are outlined. In Section 3, the main experimental observations done on the tests results from task 5.2 are reported. In section 4.1, the behaviour aimed to capture with the coupling strategy is described. In Section 4.2, the formulation for the damage interaction is presented. In Section 5, the main points and keywords of the implementation of the formulation in the Simcenter Samcef solver are listed. Verification tests on the implementation of the developed formulation are presented in Section 6. The capabilities of the developed formulation are also exemplified in Section 6. Finally, in Section 7, the main conclusions of this work are highlighted.

1.1 Background

The estimation of the load carrying capabilities of laminated composite structures is challenged by the heterogeneity and intricate arrangement of the material components. The main reason that hinders the prediction of the mechanical response of laminated composite structures is the failure process that is driven by complex and interacting damage mechanisms. At the macroscopic level, a progressive damage approach needs to model the material degradation at two clearly differentiated regions: the intra-laminar that refers to the damage occurring inside the ply and the inter-laminar that refers to the separation of adjacent plies.

A common strategy to perform structural analysis of laminated composite constructions is using the finite element method (FEM). Usually, the intra- and inter-laminar regions are modelled independently. Thus, different models are used for each region without a direct coupling between them: a local continuum damage model (CDM) is used for describing damage at the intra-laminar region, while cohesive zone models (CZM) are employed for describing delamination. However, the interchange of damage information between both regions becomes essential to model complex failure scenarios, such as matrix crack-induced delamination. This interaction has been considered in the literature (see Section 2.2 for a brief summary of the past and recent investigations on this topic), however very few contributions can be found concerning fatigue loading.

This work focusses on fatigue-driven damage in composite materials. It takes point of departure in the already implemented models for inter- and intra-laminar fatigue damage developed during tasks 5.1 and 5.2, respectively.

1.2 Objectives

The overall objectives of Task 5.3 are:

- To investigate the existing modelling strategies, with special attention to the ones that use a CDM to model intra-laminar damage and a CZM to model inter-laminar damage.
- To develop an interaction criterion to couple the already implemented fatigue damage models in the Simcenter Samcef solver during tasks 5.1 and 5.2.
- To implement the coupling formulation, together with a shared cycle jump strategy, and verify the implementation by running a numerical example of an open hole specimen.

2 Theoretical framework

2.1 The physical problem

In this work**,** the attention is focused on laminates with an arbitrary number of layers that have different fibre orientations. It is reported in references[1–4] that, in symmetric cross-ply $[0_m/90_n]_s$ laminates (see Figure 2-1.a) subjected to quasi-static loading, matrix cracking is the first damage event to come into sight (see Figure 2-1.b). It is followed by the onset of delamination at the 0°/90° layer interfaces, arising from the tip of transverse cracks and perpendicular to them (see **Error! Reference source not found.**.c). Once delamination is initiated, it is usually confined to propagate at the interface between layers because the interface is usually a resin-rich area that is less tough than the ply containing the fibres (see Figure 2-1.d). This sequence of events and their interrelation is also reported to occur under fatigue loading[5,6,7].

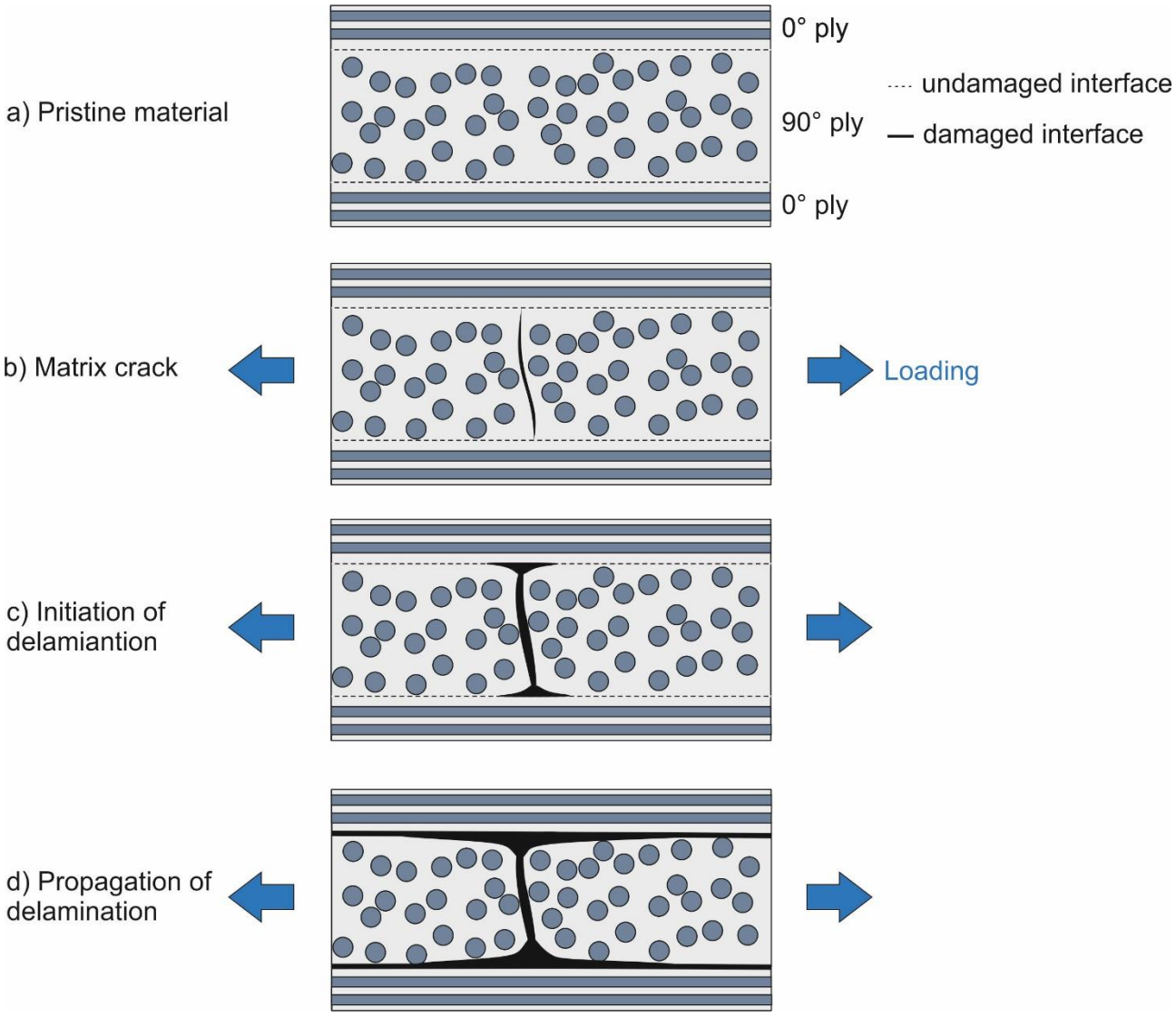

Figure 2-1. Schematic representation a matrix crack-induced delamination

At those regions where the density of matrix cracks is high, the neighbouring micro-delaminations arising from the tips of the matrix cracks coalesce forming a single macroscopic delamination (see Figure 2-2.a). Thus, the interface factures and the adhesion between layers is lost. The effect of the macroscopic delamination induced by matrix-cracking is comparable to that of an initial interfacial pre-crack. Eventually, load cases or events that entail out-of-plane stresses will cause the growth of the delaminated area due to stress concentration at the pre-crack front line (see Figure 2-2.b).

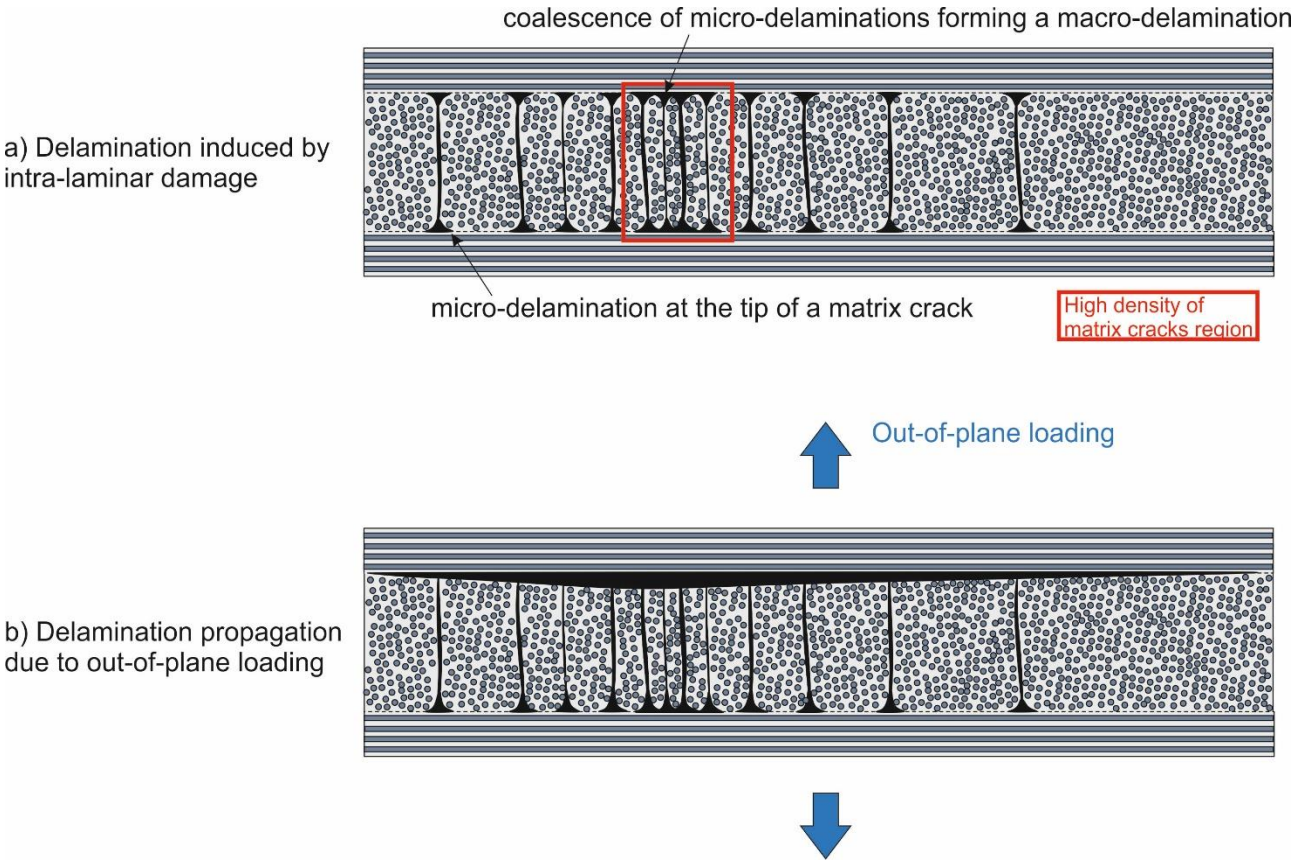

Figure 2-2. Schematic representation of the damage evolution in a cross-ply laminate

2.2 Existing modelling strategies

One of the most detrimental single failure modes in laminated composite structures is delamination since it reduces dramatically the load carrying capability. The abrupt reduction in the mechanical performance of the laminated material made delamination the most feared single failure mode for composite designers[8]. Out-of-plane loads may initiate delaminations at free edges or propagate them from already existing interfacial damage such as defects introduced during manufacturing or by other events such as impacts. However, the failure process is even more severe when the delamination is promoted by matrix cracks because it occurs at lower stress levels[6]. Thus, the interaction between matrix cracks and delamination[9–11] can significantly rush the failure process. In order to achieve good failure predictions, the sequence of damage events and their interplay has to be considered.

The most common methods for predicting delamination under static loading can be divided into two main approaches. The first approach is based purely on fracture mechanics. Usually, an extraction method for the energy release rate G, such as VCCT [12,13], is combined with a local Griffith's criterion[14] to predict delamination growth when the $G \geq G_c$, being G_c the inter-laminar fracture toughness. The second approach is based on the concept of the cohesive zone model (CZM) or interface element technique[15,16], which combines the framework of fracture mechanics and damage mechanics. With this approach, the progressive deterioration of the interface properties due to a multitude of microscopic types of damage is modelled until their coalescence and final loss of cohesion between layers. Both VCCT and cohesive elements have successfully been applied to the case of delaminations arising from a free edge[17,18] or from an initial defect[19,20]. However, it is still challenging to account for delamination promoted by matrix cracks in a meso-scale model that results in efficient computations for the analysis of composite structures[21].

The main modelling strategies to matrix crack-induced delamination available in the literature[22] can be classified into two main approaches: i) the explicit methods and ii) the implicit methods to model damage within the ply, also referred to as smeared damage models, combined with interface elements.

The first approach consists on explicitly discretize the cracks (both matrix cracks within the ply and delaminations between plies). With this modelling strategy, kinematics plays an important role in the behaviour of the discontinuity. The displacement jumps and out-of-plane stresses at the interface caused by matrix cracks are accurately described. Thus, they are suited for predicting the actual mode of failure, damage events and their sequence in a discontinuous media. Some of the methods available in the literature include the extended finite element method (XFEM)[23,24], the floating node method (FNM)[25–28], and the use of cohesive elements inside plies[21,29] to promote matrix cracks at predefined locations. The main disadvantage of these methods is that they require fine meshes to model the discontinuity (CZM), or to circumvent the need for fine meshes either by adding "floating" nodes to divide the original elements into sub-elements (FNM), or introducing extra degrees of freedom and enriched shape functions to accurately describe the displacement jump near the crack (XFEM)[30,31].

It is worth mentioning that experimental results showed that the strain level at which transverse matrix cracks are fully developed is lower than that at which delamination propagation starts[6]. Thus, the use of cohesive elements inside the plies to model matrix cracking can be avoided if one only aims to analyse the interaction between both damage mechanisms. As an efficient approach, Reference[6] proposes to introduce embedded splits within the plies modelling the matrix cracks according to the fibres direction and use cohesive elements only at the interfaces. With this strategy, the computational effort related to the use of cohesive elements inside the plies is avoided but still accurate prediction of failure is obtained. The study is limited to a single split at the centre of the specimen within each ply since the authors postulate that there is a single critical matrix crack inducing delamination according to experimental tests.

The second approach is to homogenize the material degradation process in the ply using CDM[32]. The main advantage is that continuum damage formulations can be implemented into regular nonlinear finite elements and they do not need accurate description of the kinematics of discrete cracks. The damage at the interface, in turn, is modelled using interface cohesive elements. Thus, each region (ply and interface) is modelled as a separated damageable inelastic continuum[32,33] and different damage variables are defined for each constituent. This strategy implies that the main mechanism for initiating damage at the cohesive elements, which is out–of-plane stress concentration, is smoothed due to averaged description of the deformation process occurring at the microscale. An approach to surrogate the effect of stress singularities on delamination initiation is to add an interdependence between the damage variable at the adjacent plies and the damage state at the cohesive element.

The current version of the Simcenter Samcef solver uses the second approach to model damage in laminated composite materials under quasi-static loading. The implemented formulation is based on the model presented in Reference[34] to model intra-laminar damage. Based on experimental observations on quasi-static testing, different damage mechanisms acting at the microscale are identified:

- At the ply: i) transverse matrix cracking and ii) diffuse intra-laminar damage due to fiber/matrix debonding or matrix fracture between fibres

- At the interface: iii) local delamination at crack tips of transverse matrix cracks and iv) diffuse interface damage

A CDM formulation is used to model microscale damage both at the plies and at interfaces. A damage variable is defined for each degradation mechanism acting at the microscale and it is assumed to be constant throughout the thickness of the ply. The crack density is used to quantify

damage states produced by discrete cracks (i and iii), while the loss of stiffness is a measure of the diffused damage (ii and iv). In turn, a CZM approach is used to model mesoscale delamination at the interfaces. Damage is triggered by out-of-plane stresses and it is decomposed into tensile (mode I) and shear (modes II and III).

The two-scale quasi-static damage models are related by an equivalence relation between the meso- and the micro-damage variables. Thus, the description of the meso-damage state includes the microstructure-dominated behaviour. The impact of transverse micro-cracking of the adjacent plies on the mesoscale delamination is represented by coupling the shear damage variables of the meso-scale delamination and the mean value of the rate of transverse micro-cracking at the adjacent plies.

In order to avoid the need of accessing the updated rate of transverse micro-cracking at the adjacent plies to modify the damage state of the interface cohesive element (non-local coupling), Reference[5] assumes that the in-plane deformation of the interface element is very similar to that of the adjacent ply and it can be used to estimate the crack density. The authors propose to use the in-plane strains at the top and bottom surfaces of the cohesive element to directly impact the calculations of the cohesive law. In this way, a local approach is used. So far, the calibration of the coupling parameters is based on experimental observations limited to specimens with the specific configuration of $[0_6||0_2/90_2]_s$ under mode I loading conditions.

Regarding the fatigue modelling of FRP, the main approaches available in the literature can be classified into three main categories[35]: i) fatigue life models that use a failure criterion based on S-N curves or Goodman-type diagrams, ii) residual stiffness/strength models and iii) progressive damage models, which allow modelling of the gradual deterioration of the composite material and the successive damage states.

In the last decade, multiple methods based on the CZM approach have been successfully applied to the simulation of fatigue-driven delamination propagation from an initial defect or high stress concentration points[36–39]. The fatigue progressive damage formulations are usually extensions of the models developed for quasi-static loading combined with a phenomenological description of crack propagation rate, such as a Paris' law-based curve[40]. These formulations are based on the calculation of the energy release rate using the cohesive quantities to predict the damage accumulation rate.

In the case of matrix crack-induced delamination, the main driving force for creating local delamination is the high stress concentration at the ply constituent. Since the stress singularities are produced outside the cohesive domain, the miscalculation of the energy release rate results in high under-estimation of the damage accumulation rate. Some models have been further developed to describe the nucleation of a macroscopic delamination in undamaged composites using interface cohesive elements[41,42]. A damage initiation law based on SN-curves is combined with the damage propagation law based on the crack growth rate, allowing modelling of the whole fatigue life in a single analysis. However, the identification of the damage onset is still based on the maximum load in the interface domain. In order to capture the effect of matrix cracks on delamination initiation, the intra-laminar damage state needs to play a role in the cohesive behaviour. To this end, a coupling mechanism between the intra- and inter-laminar fatigue damage models needs to be incorporated.

The current version of the Simcenter Samcef solver uses the model presented in Reference[43] to model intra-laminar damage and the model presented in Reference[36] to model inter-laminar damage under fatigue loading. An interaction model between these two models has been developed and presented in Section 4 of this document. In the following, the two independent models are briefly described.

2.3 Summary of the intra-laminar fatigue damage model implemented in Simcenter Samcef

The semi-empirical modelling approach utilized in this report is based on the stiffness degradation laws developed by van Paepegem and Degrieck[43]. The overarching aim of this fatigue damage model is to predict the different stages of the stiffness degradation curve for a wide range of FRP materials. Figure 2-3 illustrates the typical fatigue curve for a wide range of FRP materials. Stage I corresponds to a rapid albeit small initial drop in stiffness, which is dominated by the onset of transverse matrix cracking and progresses non-linearly with the number of cycles. Stage II corresponds to a prolonged albeit small drop in stiffness, which progresses approximately linearly with respect to the number of cycles. The damage manifested during this stage is mainly the growth of longitudinal matrix cracks along 0° fibres and small delamination cracks at the coupon edges. Lastly, stage III corresponds to a transition from matrix damage to fibre damage and a precipitous non-linear final drop in stiffness, which accounts for the in-plane laminate stiffness.

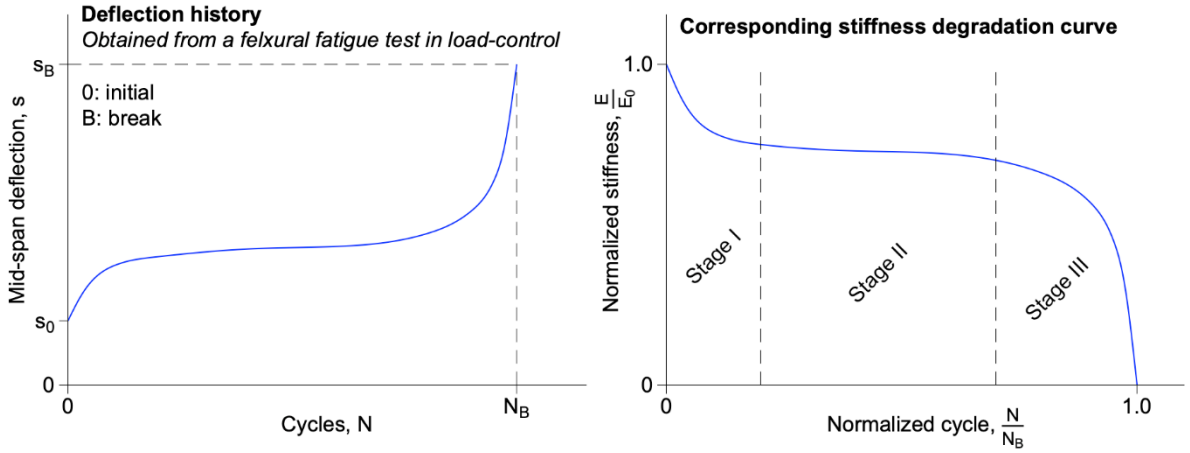

Figure 2-3. Typical fatigue curves for a wide range of FRP materials (adapted from Reference[43]).

Three damage variables are defined to capture the different types of intra-laminar damage: longitudinal (i.e. along to the fibre direction), D_{11}; transverse (i.e. in-plane normal to the fibre direction), D_{22}; and in-plane shear, D_{12}. These damage variables directly affect the lamina stiffness response. The 1-2-3 Cartesian axes correspond to the fibre, transverse, and through-thickness ply orientations, respectively, i.e. the on-axis reference frame. First, they are assembled into the diagonal damage stiffness matrix:

$$\mathrm{diag}\left(\underline{\underline{D}}\right) = < D_{11} \quad D_{22} \quad 0 \quad D_{12} \quad 0 \quad 0 > \qquad \text{Eq. 2-1}$$

Damage is either caused by static or fatigue loading. These two types of damage types are combined into a single damage matrix:

$$\underline{\underline{D}} = \underline{\underline{D}}^s + \underline{\underline{D}}^f \qquad \text{Eq. 2-2}$$

where $\underline{\underline{D}}_s$ and $\underline{\underline{D}}_f$ represent the static and fatigue damage components, respectively. However, the fatigue behaviour law used herein does not capture the onset and evolution of static damage. An initial value can instead be considered:

$$\dot{\underline{\underline{D}}} = \dot{\underline{\underline{D}}}^f, \text{ where: } \underline{\underline{D}}(t=0) = \underline{\underline{D}}^s \qquad \text{Eq. 2-3}$$

Each damage term is a unit ratio between 0 and 1 with a value of 0 signifying an undamaged material and a value of 1 signifying complete failure. In practice, the failure value is limited and set very close to but not exactly 1 to avoid numerical issues, i.e. a singular stiffness matrix:

$$D_{ij} = \min(D_{ij}, d_{max}), \text{ where: } d_{max} \leq 0.999 \qquad \text{Eq. 2-4}$$

The effect of fatigue damage on the lamina stiffness differs between tensile and compressive loading state. Crack closure can occur during the latter. The fatigue damage tensor is computed as follows. The function $\langle \sigma_{ij} \rangle$ filters positive values of σ_{ij}:, which is used to compute the effect of the damage state on the stress tensor over the current time step. The fatigue damage matrixes, $\underline{\underline{D}}^{f+}$ and $\underline{\underline{D}}^{f-}$, represent the fatigue damage effect in case of tensile and compressive state, respectively.

Instances of the fatigue damage matrix, $\underline{\underline{D}}^{f+}$ and $\underline{\underline{D}}^{f-}$, represent the fatigue damage due to tensile and compressive loading states, respectively. They are computed as follows:

$$\begin{aligned} D_{ij}^{f+} &= d_{ij}^{+} + d_{ij}^{-} \\ D_{ij}^{f-} &= h d_{ij}^{+} + d_{ij}^{-} + (1-h)\delta_{i4}\delta_{4j}d_{12}^{+} \end{aligned} \qquad \text{Eq. 2-5}$$

where h is a material coefficient that differentiates the impact of the damage in case of tensile or compressive stress and characterizes the crack closure effect. It can be fixed at $h = 0.2$ according to Reference[44]. In turn, the components d_{ij}^{+} and d_{ij}^{-} correspond of the damage due to tensile and compressive state. Figure 2-4 illustrates the difference in fatigue damage evolution over a single cycle between damage components depending on whether the corresponding stress is positive or negative. It is a simplified case meant to illustrate the reasoning for separating the tensile and compressive damage states given the different damage modes. It should be noted that no such difference exists in the case of in-plane shear.

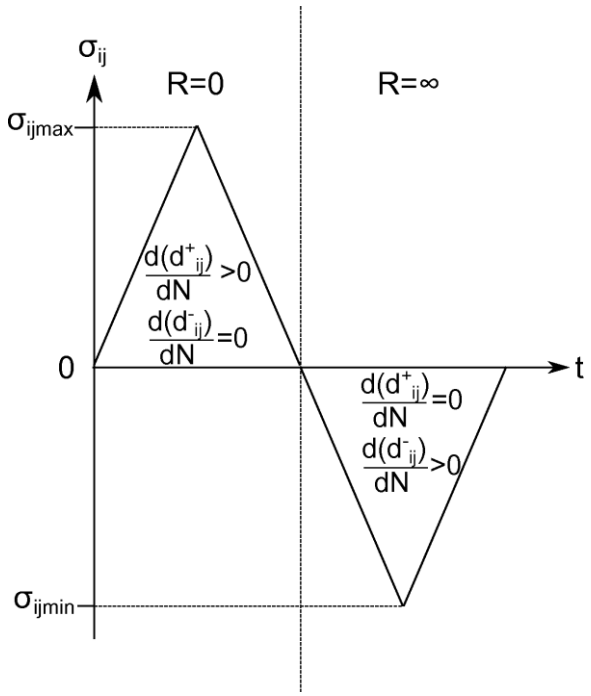

Figure 2-4 : Interpretation of the tension-compression fatigue loading cycle

2.3.1 Behaviour law

The fatigue behaviour law is formulated as follows:

$$\underline{\sigma} = \underline{\underline{C}}\underline{\varepsilon}^{e} = \underline{\underline{H}}\,\underline{\underline{S}}^{-1}\underline{\underline{H}}\left(\underline{\varepsilon} - \underline{\varepsilon}^{p}\right) \qquad \text{Eq. 2-6}$$

where $\underline{\underline{S}}$ and $\underline{\underline{H}}$ are the stiffness and on-to-off axis transformation matrices, respectively:

$$\underline{\underline{S}} = \begin{bmatrix} \frac{1}{E_1^0} & -\frac{\nu_{12}^0}{E_1^0} & -\frac{\nu_{13}^0}{E_1^0} & 0 & 0 & 0 \\ -\frac{\nu_{12}^0}{E_1^0} & \frac{1}{E_2^0} & -\frac{\nu_{23}^0}{E_2^0} & 0 & 0 & 0 \\ -\frac{\nu_{13}^0}{E_1^0} & -\frac{\nu_{23}^0}{E_2^0} & \frac{1}{E_3^0} & 0 & 0 & 0 \\ 0 & 0 & 0 & \frac{1}{G_{12}^0} & 0 & 0 \\ 0 & 0 & 0 & 0 & \frac{1}{G_{23}^0} & 0 \\ 0 & 0 & 0 & 0 & 0 & \frac{1}{G_{13}^0} \end{bmatrix} \qquad \text{Eq. 2-7}$$

$$\text{and } \underline{\underline{\mathrm{H}}} = \sqrt{\underline{\underline{I}} - \underline{\underline{D}}}$$

and where: σ_{ij} are the stress tensor components along the x-y-z global axes; $\mathrm{E}_1^0, \mathrm{E}_2^0 \text{ and } \mathrm{E}_3^0$ are the initial Young's moduli; $\nu_{12}^0, \nu_{23}^0 \text{and } \nu_{13}^0$ are the initial Poisson's ratios; G_{12}^0, G_{13}^0 and G_{23}^0 are the initial shear moduli; and $\underline{\varepsilon}^{\mathrm{p}}$ is plastic (also permanent) strain tensor defined in Reference[44]. It should be noted that in this case, the square root is one in the same as the component-wise square root given that the matrices are diagonal. The stiffness matrix is that of the on-axis lamina response and is aligned along the 1-2-3 material axes.

2.3.2 Fatigue failure indices

The fatigue failure indices describe a reserve to failure based on the effective stresses and a failure surface.

2.3.2.1 Definition of the effective stress

The effective stress tensor,$\underline{\tilde{\sigma}}$, is defined by

$$\underline{\tilde{\sigma}} = \left(\underline{\underline{I}} - \underline{\underline{D}}\right)^{-1}\underline{\sigma} \qquad \text{Eq. 2-8}$$

where the tensor $\underline{\underline{\mathrm{I}}}$ is the identity tensor.

2.3.2.2 Strength coefficients

the in-plane longitudinal and transverse lamina strengths, X and Y, are computed according to the stress components, with subscripts $_{\mathrm{C}}$ and $_{\mathrm{T}}$ indicating a compression and tension, respectively:

$$X = X_T\frac{\langle\sigma_{11}\rangle}{|\sigma_{11}|} + X_C\frac{\langle-\sigma_{11}\rangle}{|\sigma_{11}|}$$
$$Y = Y_T\frac{\langle\sigma_{22}\rangle}{|\sigma_{22}|} + Y_C\frac{\langle-\sigma_{22}\rangle}{|\sigma_{22}|} \qquad \text{Eq. 2-9}$$

where: $\{X_C, Y_C\} \geq 0$

2.3.2.3 Simplified Tsai Wu's criterion

The simplified Tsai Wu's failure surface is shown in Figure 2-5 and expressed as:

$$\left(\frac{\tilde{\sigma}_{11}}{X}\right)^2 + \left(\frac{\tilde{\sigma}_{22}}{Y}\right)^2 + \left(\frac{\tilde{\sigma}_{12}}{S}\right)^2 = 1 \qquad \text{Eq. 2-10}$$

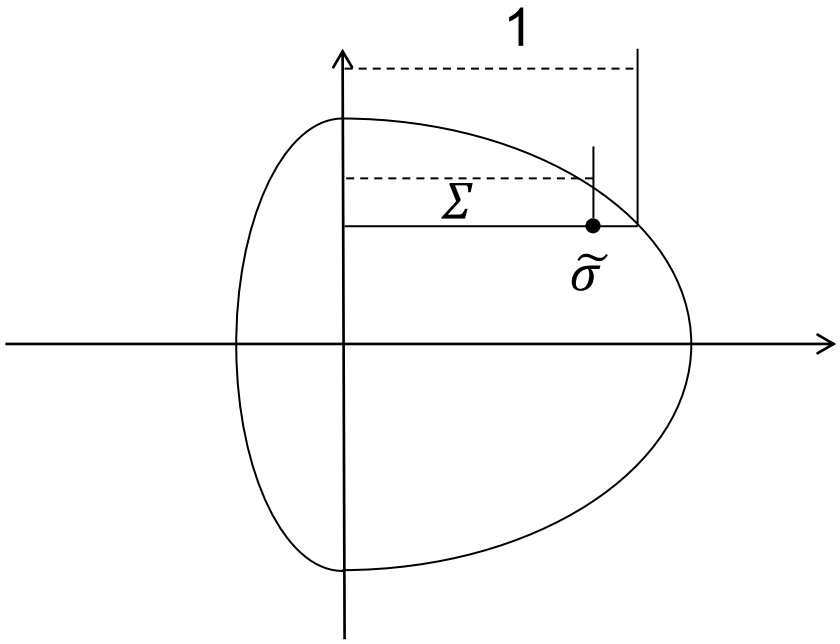

Figure 2-5 : simplified Tsai Wu's failure surface

where S is the in-plane shear stress limit before failure.

The fatigue failure components are computed by solving the following two-degree polynomial equations:

$$\begin{aligned}
\left(\frac{\tilde{\sigma}_{11}}{X\Sigma_{11}}\right)^2 + \left(\frac{\tilde{\sigma}_{22}}{Y}\right)^2 + \left(\frac{\tilde{\sigma}_{12}}{S}\right)^2 &= 1 \\
\left(\frac{\tilde{\sigma}_{11}}{X}\right)^2 + \left(\frac{\tilde{\sigma}_{22}}{Y\Sigma_{22}}\right)^2 + \left(\frac{\tilde{\sigma}_{12}}{S}\right)^2 &= 1 \\
\left(\frac{\tilde{\sigma}_{11}}{X}\right)^2 + \left(\frac{\tilde{\sigma}_{22}}{Y}\right)^2 + \left(\frac{\tilde{\sigma}_{12}}{S\Sigma_{12}}\right)^2 &= 1
\end{aligned} \qquad \text{Eq. 2-11}$$

Thus:

$$\begin{aligned}
\Sigma_{11} &= \frac{|\tilde{\sigma}_{11}|}{X\sqrt{1 - \left(\frac{\tilde{\sigma}_{22}}{Y}\right)^2 - \left(\frac{\tilde{\sigma}_{12}}{S}\right)^2}} \\
\Sigma_{22} &= \frac{|\tilde{\sigma}_{22}|}{Y\sqrt{1 - \left(\frac{\tilde{\sigma}_{11}}{X}\right)^2 - \left(\frac{\tilde{\sigma}_{12}}{S}\right)^2}} \\
\Sigma_{12} &= \frac{|\tilde{\sigma}_{12}|}{S\sqrt{1 - \left(\frac{\tilde{\sigma}_{11}}{X}\right)^2 - \left(\frac{\tilde{\sigma}_{22}}{Y}\right)^2}}
\end{aligned} \qquad \text{Eq. 2-12}$$

2.3.2.4 Maximum stress criterion

The computation of the fatigue failure indices is based on the maximum stress failure criterion:

$$\Sigma_{11} = \frac{|\tilde{\sigma}_{11}|}{X}$$
$$\Sigma_{22} = \frac{|\tilde{\sigma}_{22}|}{Y} \qquad \text{Eq. 2-13}$$
$$\Sigma_{12} = \frac{|\tilde{\sigma}_{12}|}{S}$$

2.3.3 Evolution law of the fatigue damage in a unidirectional ply

The laws for the evolution of fatigue damage are defined as follows:

$$\frac{d(d_{11}^{+})}{dN} = c_{1,11}\left(1 + i_c\, {D_{12}^{f}}^2\right)\Delta\Sigma_{11}^{+}\exp\left(-c_{2,11}\frac{d_{11}^{+}}{\sqrt{\Delta\Sigma_{11}^{+}}\,(1 + i_c D_{12}^2)}\right) + c_{3,11}d_{11}^{+}{\Delta\Sigma_{11}^{+}}^2\exp\left(c_{5,11}\langle\Delta\Sigma_{11}^{+} - c_{4,11}\rangle\right)$$

$$\frac{d(d_{11}^{-})}{dN} = \left[c_{1,11}\left(1 + i_c {D_{12}^{f}}^2\right)\Delta\Sigma_{11}^{-}\exp\left(-c_{2,11}\frac{d_{11}^{-}}{\sqrt{\Delta\Sigma_{11}^{-}}(1 + icD_{12}^2)}\right)\right]^{1+2\exp\left(-i_c {D_{12}^{f}}^2\right)} + c_{3,11}d_{11}^{-}{\Delta\Sigma_{11}^{-}}^2\exp\left(\frac{c_{5,11}}{3}\langle\Delta\Sigma_{11}^{-} - c_{4,11}\rangle\right) \qquad \text{Eq. 2-14}$$

$$\frac{d(d_{22}^{+})}{dN} = c_{1,22}\left(1 + {D_{12}^{f}}^2\right)\Delta\Sigma_{22}^{+}\exp\left(-c_{2,22}\frac{d_{22}^{+}}{\sqrt{\Delta\Sigma_{22}^{+}}\,(1 + D_{12}^2)}\right) + c_{3,22}d_{22}^{+}{\Delta\Sigma_{22}^{+}}^2\exp\left(c_{5,22}\langle\Delta\Sigma_{22}^{+} - c_{4,22}\rangle\right)$$

$$\frac{d(d_{22}^{-})}{dN} = \left[c_{1,22}\left(1 + {D_{12}^{f}}^2\right)\Delta\Sigma_{22}^{-}\exp\left(-c_{2,22}\frac{d_{22}^{-}}{\sqrt{\Delta\Sigma_{22}^{-}}(1 + D_{12}^2)}\right)\right]^{1+2\exp\left(-{D_{12}^{f}}^2\right)} + c_{3,22}d_{22}^{-}{\Delta\Sigma_{22}^{-}}^2\exp\left(\frac{c_{5,22}}{3}\langle\Delta\Sigma_{22}^{-} - c_{4,22}\rangle\right) \qquad \text{Eq. 2-15}$$

$$\frac{d(d_{12}^{+})}{dN} = c_{1,12}(1 + (d_{12}^{-})^2)\Delta\Sigma_{12}^{+}\exp\left(-c_{2,12}\frac{d_{12}^{+}}{2\sqrt{\Delta\Sigma_{12}^{+}}(1 + (d_{12}^{-})^2)}\right) + c_{3,12}d_{12}^{+}{\Delta\Sigma_{12}^{+}}^2\exp\left(c_{5,12}\langle\Delta\Sigma_{12}^{+} - c_{4,12}\rangle\right)$$

$$\frac{d(d_{12}^{-})}{dN} = c_{1,12}(1 + (d_{12}^{+})^2)\Delta\Sigma_{12}^{-}\exp\left(-c_{2,12}\frac{d_{12}^{-}}{2\sqrt{\Delta\Sigma_{12}^{-}}(1 + (d_{12}^{+})^2)}\right) + c_{3,12}d_{12}^{-}{\Delta\Sigma_{12}^{-}}^2\exp\left(c_{5,12}\langle\Delta\Sigma_{12}^{-} - c_{4,12}\rangle\right) \qquad \text{Eq. 2-16}$$

where

- $c_{i,j}$ (i=1,5 and j=11, 22 or 12) are material coefficients,
- i_c is a user parameter that activates coupling between $d_{11}^{\pm}$ and D_{12}^{f},
- and:

$$\Delta\Sigma_{ij}^{+} = \max_{t}\left(\Sigma_{ij}\frac{\langle\sigma_{ij}\rangle}{|\sigma_{ij}|}\right) - i_{ffi}\min_{t}\left(\Sigma_{ij}\frac{\langle\sigma_{ij}\rangle}{|\sigma_{ij}|}\right)$$
$$\Delta\Sigma_{ij}^{-} = \max_{t}\left(\Sigma_{ij}\frac{\langle-\sigma_{ij}\rangle}{|\sigma_{ij}|}\right) - i_{ffi}\min_{t}\left(\Sigma_{ij}\frac{\langle-\sigma_{ij}\rangle}{|\sigma_{ij}|}\right)$$ Eq. 2-17

where i_{ffi} is a user parameter to choose between maximum or range fatigue failure index by cycle.

2.4 Summary of the inter-laminar damage model implemented in Simcenter Samcef

The inter-laminar damage model[45] is based on the cohesive zone model approach. In the FE implementation, the cohesive behaviour is reduced to the mid-surface $\bar{S}$ between the upper surface, S^+, and the lower surface, S^- (see Figure 2-6). Thus, the deformed mid-surface is defined as the average distance between the two initially coincident delamination surfaces. The cohesive variables are calculated at the integration points, located on the mid-surface, and decomposed into mode I component (following the normal $\vec{e}_3$-direction to the midsurface) and shear components (following two tangential $\vec{e}_1$ and $\vec{e}_2$-directions to the mid-surface).

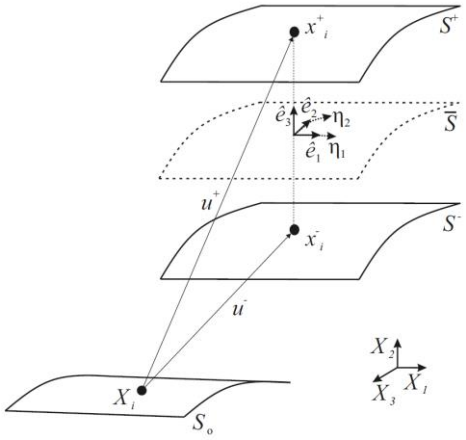

Figure 2-6. Description of the deformed element mid-surface, $\bar{S}$. [46]

The behaviour law is:

$$\sigma_i = K\{(1-d)\delta_i - d\langle-\delta_3\rangle\} \text{ for } i = 1,2$$
$$\sigma_3 = K\{(1-d)\delta_3 - d\langle-\delta_3\rangle\}$$ Eq. 2-18

where K is the penalty stiffness, d is the damage variable and $\langle\cdot\rangle$ are the Macaulay brackets.

The norm of the jump displacement is:

$$\lambda = \sqrt{\delta_I^2 + \delta_s^2} \text{ where } \delta_I = \langle\delta_3\rangle;\ \delta_s^2 = \delta_1^2 + \delta_2^2$$ Eq. 2-19

The local mixed-mode ratio is computed as:

$$B = \frac{\delta_s^2}{{\delta_I}^2 + \delta_s^2}$$ Eq. 2-20

The fracture toughness (G_c) is mode-dependent. This implies that the propagation criterion needs to be formulated in terms of the pure mode fracture toughnesses and the mixed mode ratio. The interaction between loading modes is done using the B-K criterion[47]:

$$G_c = G_{Ic} + (G_{IIc} - G_{Ic})B^{\eta}$$ Eq. 2-21

where G_{Ic} is the mode I fracture toughness, G_{IIc} the fracture toughness under shear loading, η is the B-K interaction parameter and B is the mixed-mode ratio. Note that, since mode III fracture toughness is often higher than that of mode II loading, as a conservative approach, the fracture properties of mode II are generally attributed to any combination of shear mode.

The onset criterion also needs to be interpolated through the different loading modes. In this model, the propagation and initiation criteria are linked, such that the criterion for delamination onset is also based on the B-K criterion[48]:

$$\mu_0 = \sqrt{(\tau_{Io})^2 + ((\tau_{IIh\,o})^2 - (\tau_{Io})^2)(B)^\eta} \qquad \text{Eq. 2-22}$$

where μ_o is the equivalent one-dimensional interlaminar strength, τ_{Io} is the mode I inter-laminar strength and $\tau_{II\,o}$ is the shear mode inter-laminar strength. Since it is assumed that the penalty stiffness (k) is mode independent[49], the relation between cohesive properties must fulfil:

$$\frac{\tau_{sh\,o}}{\tau_{Io}} = \sqrt{\frac{\mathcal{G}_{sh\,c}}{\mathcal{G}_{Ic}}} \qquad \text{Eq. 2-23}$$

The displacement jump for the initiation, λ_0, and final decohesion, λ_c, are related to the parameters of the cohesive law:

$$\lambda_0 = \frac{\mu_0}{K}, \lambda_c = \frac{2G_c}{\mu_0} \qquad \text{Eq. 2-24}$$

In order to improve convergence, two features are usually used for all continuous damage laws implemented in Simcenter Samcef:

1. An upper limit (d_{max}) for the stiffness-degrading damage ($\mathcal{D}^k$) that is very close but lower than 1. This is done to avoid elements with null stiffness. Thus, the implemented d reads:

$$\mathcal{D}^k = \max\left(\min\left(\frac{\lambda_c\langle\lambda-\lambda_0\rangle}{\lambda(\lambda_c-\lambda_0)}, d_{max}\right), \omega\right) \qquad \text{Eq. 2-25}$$

where r is the historical maximum value of d, or current damage threshold.

Secondly, a delayed damage strategy that smoothens the transition from the elastic behaviour to damage by applying a low viscosity effect.

$$\dot{\mathcal{D}^k} = \frac{1}{\tau_c}\{1 - exp(-a_c\langle\omega - d\rangle)\} \qquad \text{where } \omega = \frac{\lambda_c\langle\lambda-\lambda_o\rangle}{\lambda(\lambda_c-\lambda_o)} \qquad \text{Eq. 2-26}$$

where τ_c is a time delay characteristic parameter and a_c is a delay coefficient.

2.4.1 Evolution law of the fatigue damage at the interface

The simulation of fatigue damage follows an envelope load approach. Thus, the number of cycles is discretized and the energy-based damage variable, $\mathcal{D}^e$, is updated for each equilibrium step. The damage at a given number of cycles is determined by integration of the damage rate $\left({d\mathcal{D}^e}/{dN}\right)$. The damage rate is linked to the crack growth rate $\left({da}/{dN}\right)$ as:

$$\frac{d\mathcal{D}^e}{dN} = \frac{\partial\mathcal{D}^e(B,\lambda)}{\partial a}\frac{da}{dN} = \left(\frac{\partial\mathcal{D}^e}{\partial B}\frac{\partial B}{\partial a} + \frac{\partial\mathcal{D}^e}{\partial\lambda}\frac{\partial\lambda}{\partial a}\right)\frac{da}{dN} \qquad \text{Eq. 2-27}$$

where the partial derivatives $\frac{\partial\mathcal{D}^e}{\partial B}$ and $\frac{\partial\mathcal{D}^e}{\partial\lambda}$ depend on the quasi-static cohesive zone model formulation and the current displacement field. These derivatives are further developed in references[45,38,46]. The factors $\frac{\partial B}{\partial a}$ and $\frac{\partial\lambda}{\partial a}$ relate the propagation of the crack front to the local pointwise change of the mode-

mixity (B) and the equivalent one-dimensional displacement jump (λ), respectively. Therefore, these derivatives can be interpreted as the link between the local damage evolution and the crack propagation.

The strength of this method is that, any phenomenological expression for the da/dN that is a function of the energy release rate (G) can be easily included in the simulation. In this case, the crack growth rate is evaluated by:

$$\frac{da}{dN} = \begin{cases} A\left(\frac{G_{max}\,(1-R)}{G_c}\right)^p & \text{for} \quad G_{th} < G_{max} < G_c \\ 0 & \text{for} \quad G_{max} \leq G_{th} \end{cases} \qquad \text{Eq. 2-28}$$

where G_{max} is the maximum cyclic energy release rate measured using the *J*-integral approach (more information can be found in Reference[50]), R is the load ratio, defined as:

$$R = \sqrt{\frac{G_{min}}{G_{max}}} \qquad \text{Eq. 2-29}$$

and $\mathcal{G}_{th}$ is the energy release rate threshold below which no propagation occurs.

The dependency of the Paris' law-based parameters (A and p) with the mode mixity is evaluated in terms of the energy release rate. The formulation from Reference[51] is used:

$$p = \Phi^2(p_{sh} - p_I - p_m) + \Phi\, p_m + p_I \qquad \text{Eq. 2-30}$$

$$\log(A) = \Phi^2 \log\left(\frac{A_{sh}}{A_m A_I}\right) + \Phi \log(A_m) + \log(A_I) \qquad \text{Eq. 2-31}$$

where p_I and A_I are the parameters for pure mode I, p_{sh} and A_{sh} are the parameters for shear mode, and p_m and A_m are mode interpolation parameters.

The global measure of the mode-mixity is defined as:

$$\Phi = \frac{G_{sh}}{G_I + G_{sh}} \qquad \text{Eq. 2-32}$$

where $\mathcal{G}_I$ and $\mathcal{G}_{sh}$ are the energy release rates associated to mode I and shear loading. In this model, the evaluation of the energy release rates is made by means of the *J*-integral approach.

Finally, the energy-based damage variable is related to the stiffness-degrading damage variable, $\mathcal{D}^k$, and the norm of the displacement jump, λ, as:

$$\mathcal{D}^e = 1 - \frac{\lambda_c\left(1-\mathcal{D}^k\right)K\lambda}{2\mathcal{G}_c} \qquad \text{Eq. 2-33}$$

3 Experimental observations from Task 5.2

During task 5.2, GFRP specimens were tested using a four-point loading configuration under static and fatigue loading. Further details on the testing set-up are given in deliverable D5.2. The specimens consisted of a stacking sequence of UD non-crimp fabric (NCF) layers that were infused with an epoxy resin. The NCF itself consists of 90 wt.% of high-modulus (HM) glass fibre roving (or bundles) that are stitched together. The nominal cured ply thickness was approximately 1 mm. Five specimens of the six laminate stacking sequences listed in Table 3-1 were tested. The first five laminates were reserved to generate test data for the parameter identification of the intra-laminar fatigue model. The sixth laminate was reserved for validation of the identified parameters and overall model performance.

Table 3-1. Laminate stacking sequences.

Test order	Reference code	Description	Stacking sequence	Purpose
1	U	Unidirectional	$[0°]_{2S}$	
2	O45	±45° off-axis	$[\pm45°]_S$	Model
3	T	Transverse	$[90°]_{2S}$	parameter
4	X	Cross-ply	$[0°/90°]_S$	identification
5	O30	±30° off-axis	$[\pm30°]_S$	
6	Q	Quasi-isotropic	$[0°/\pm45°/90°]_S$	Model validation

The coupon and loading geometries of the first five laminates are loosely based on specimen Class III and Annex A of ISO 14125[52]. The nominal thickness of 4 mm requires a doubling of proportions and spans. In addition, the prescribed width was increased to 20 mm such as to include a minimum of five fibre bundles across the width of 0° plies to ensure representative results that are reproducible between coupons. Table 3-2 lists the coupon and loading configuration geometries. A ply misalignment of 1.51° with a standard deviation of 0.142° (16 measurements) was calculated using Fiji's ImageJ software package[53] and a high-resolution scan of the bottom surface of U coupons. The misalignment was taken as the angle created by longitudinal stiches running in parallel to cut-off fibre bundles and the longitudinal coupon edges. It is attributed to operator error during manual layup and resin flow during the infusion process[54]. Despite this source of error, the specimen dimensions were all within the tolerances specified in ISO 14125[52], and the inner and outer spans were set with a coefficient of variation of less 1% from nominal values for all tested coupons.

Table 3-2. Coupon and loading configuration geometries.

Nominal values (mm)	Laminate	
	U, O45, T, X, and O30	Q
Thickness, h	4	8
Width, b	20*	20*
Length, l	150*	150*
Outer span, L	90	120*
Inner span, L'	30	40*
Outer span-to-thickness ratio, L/h	22,5	15*
Inner span to thickness ratio, L'/h	7,5	5*

* Deviation from the ISO 14125 standardized test method[52].

The speed of quasi-static loading ramp was set to 1 mm/min for all tests. The mean flexural modulus, E_f, and the strength at break, σ_{fB}, were the main material properties determined for each sample. Static failure, characterized by a small load drop on the load-deflection curve due to matrix cracking and fibre breakage, was defined as the onset of damage rather than full coupon rupture.

The fatigue testing was performed in load control with constant load ratio $R = 0.1$. The upper load limit was derived from the selected loading fraction for a given laminate, which is the ratio of the maximum applied flexural stress and the laminate's flexural strength. The loading was chosen sufficiently low as to avoid imparting static damage during the first fatigue cycle but high enough to reduce the test duration to less than one day or approximately 50k cycles. The cycle frequency was set to 2 Hz. Prior to launching the sinusoidal cyclic loading, the operator checked that no static damage is imparted during the first loading cycle by stopping the test and inspecting the load-deflection data.

In deliverable D5.2, it was reported that a varying albeit significant degree of inter-laminar damage was observed in coupons from all six laminates under static loading. The stiffer configurations, U and Q, failed in compression including some inter-laminar shear delamination and localized fibre crushing from the inner rollers. The exception is configuration X, which failed in inter-laminar shear at the 0°/90° interfaces likely spurred by matrix micro-cracking in the central 90° plies. In turn, the two off-axis configurations, O45 and O30, failed in tension including some inter-laminar shear delamination. Lastly, the weakest configuration, T, failed cleanly in tension.

It was observed much more pronounced inter-bundle cracking and inter-laminar delamination in coupons of all six configurations under fatigue loading, including changes in failure mode compared to the corresponding quasi-static. Figure 3-1 presents schematics of the representative failure modes for each configuration. Configuration U failed in compression under the loading rollers with extensive fibre delamination in the top ply between the upper rollers. However, slightly misaligned fibre bundles on the bottom ply and interrupted by the longitudinal coupon edges also began to peel-off. The three weakest configurations, O45, T and O30, presented with extensive inter-laminar delamination between the fibre bundles in bottom plies with some bundles peeling-off at the coupon edges. The greatest change in failure mode was the configuration Q, which failed in inter-laminar shear with cracking initiating in the central 90° plies and suddenly propagating at the ±45°/90° interfaces. The only configuration with a failure mode that was unchanged was configuration X, which also failed suddenly in delamination.

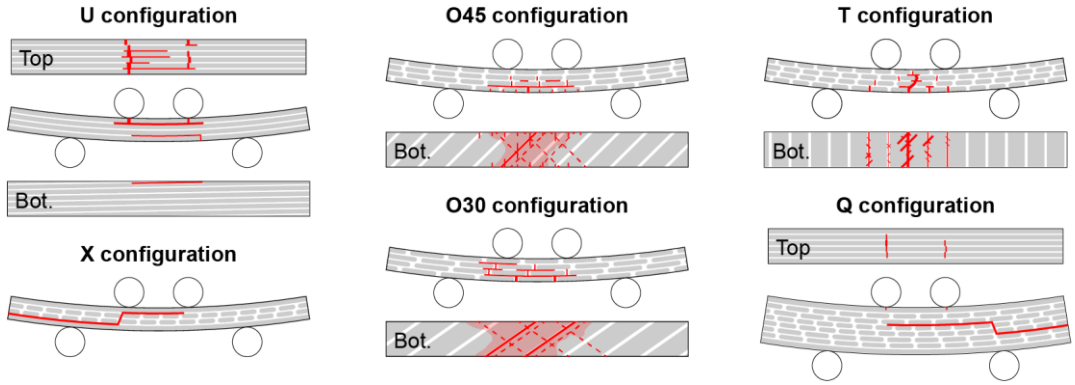

Figure 3-1. Schematics of the representative failure mode for the cross-ply specimens of Task 5.2.

The numbers of cycles at break were marked by large scatters (see Figure 3-2), which many previous experimental and modelling studies and reviews have documented including Reference[43] about the fatigue intra-laminar damage model implemented in Simcenter Samcef. The remainder of the scatter can be explained by intrinsic variations in static strength properties. Similar discontinuities (sharp upward kinks) can be observed in the fatigue curves of the U, T and Q configurations, whereby the mode of matrix-cracking changes from intra-ply (inter-bundle) to inter-ply delamination.

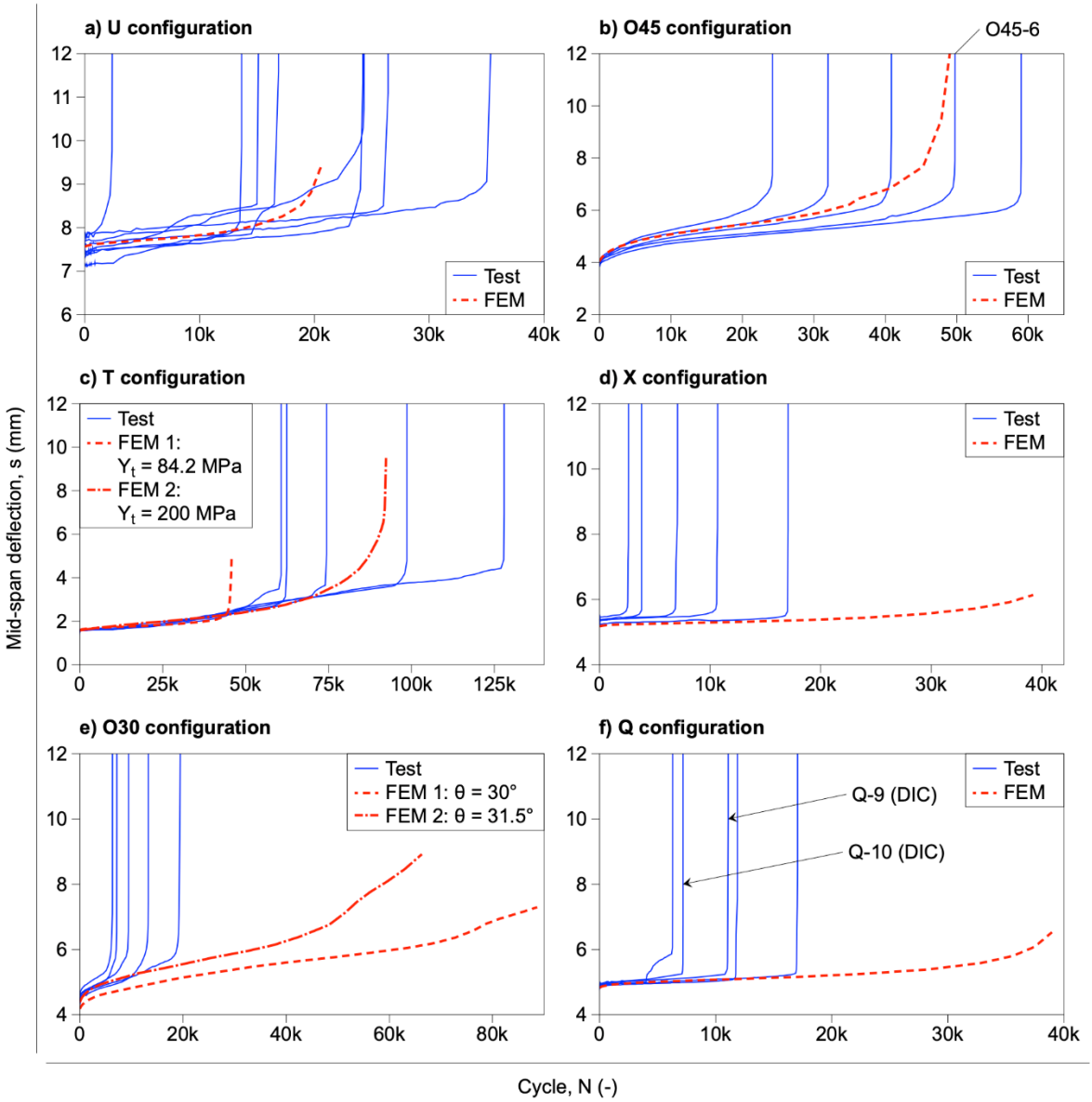

Figure 3-2. History curve of the maximum mid-span deflection per cycle and the corresponding FEM prediction only using the intra-laminar damage model for the cross-ply specimens of Task 5.2.

The relatively complex meso-structure present in all six laminates adds an additional element of randomness. Figure 3-3 presents a microscopy cross-section of the quasi-isotropic laminate (Q). Fibre bundles are delimited by a distinct interstitial resin network, the bulk of which is intraply. The NCF stitching is also clearly discernible as it threads through resin-rich pockets (Figure 3-3.a-c). The intra-laminar heterogeneity results in matrix cracks forming between fibre bundles at the bundle or stitching interface rather than within bundles. Delamination cracks eventually ensue as these inter-bundle cracks reach adjacent inter-laminar interfaces. Moreover, the presence of superimposed fibre bundles through-the-thickness, notably in the case of the T and X configurations, is thought to significantly aid the out-of-plane crack propagation.

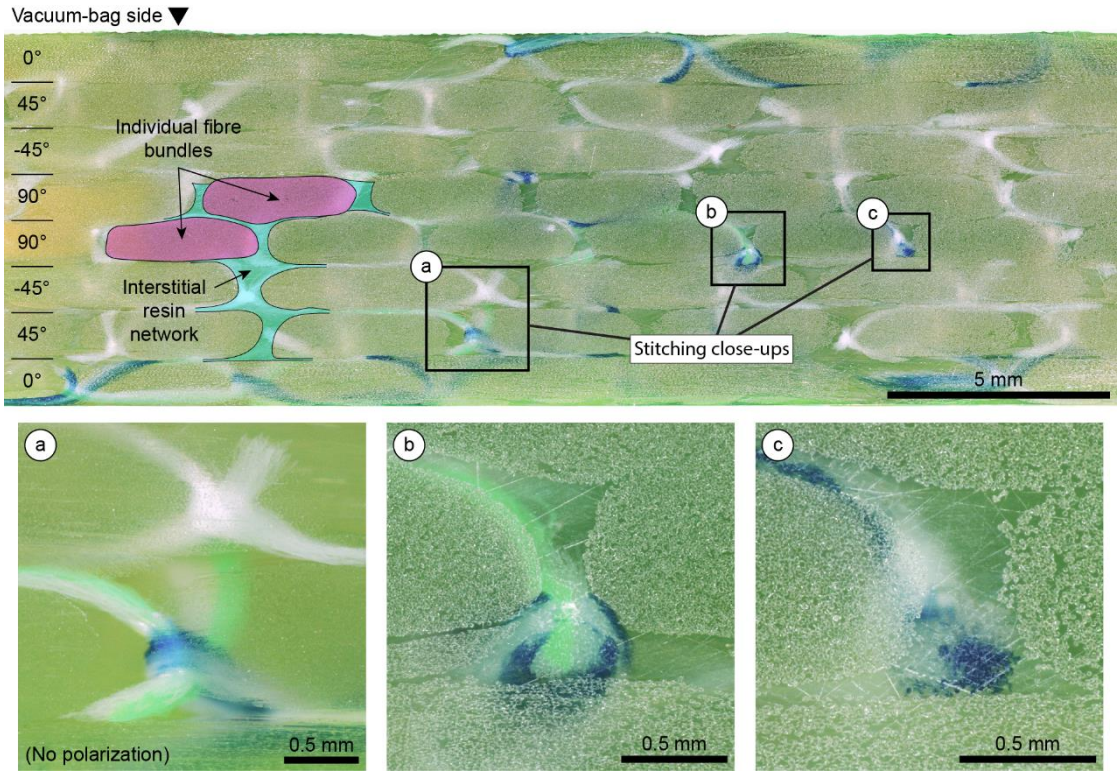

Figure 3-3. Stitched micrographic cross-section of the quasi-isotropic laminate—Q (brightfield illumination; 2-9x magnification; 15° angle slice from the 0° fibre orientation—x axis; strong polarization).

To sum up, three main conclusions can be drawn from the observation of the experimental results obtained during task 5.2:

1 Even though a more comprehensive fractographic analysis is warranted to better understand the onset and evolution of different failure modes, their interplay and the impact of the meso-structure, it can be confirmed that there is a strong interaction between matrix cracks and delamination.

2 The intra-laminar fatigue damage model implemented in the Simcenter Samcef solver is restricted to damage occurring at the region within the ply (matrix cracking, fibre/matrix debonding, fibre pull-out, etc.)[43]. The model aims at simulating the three stages of stiffness degradation, including final failure (see Figure 2-3). However, it does not aim at capturing the effects on the stiffness reduction due to delamination because the driving mechanisms that cause delamination differ from those that cause intra-laminar damage. While in-plane longitudinal, transverse and shear stresses are mostly responsible for damage within the ply, out-of-plane normal and shear stresses are predominantly responsible for damage at the interfaces between plies. Thus, the laminate configurations and loading conditions should be selected such that the test data used for the parameter identification of the intra-laminar fatigue model is not affected by the occurrence of delaminations.

In deliverable D5.2, it is reported that extensive inter-laminar delamination in coupons of all six configurations under fatigue loading was observed through inspection of the failed specimen surfaces. The identified model parameters were fitted using all range data, including stiffness degradation due to the occurrence of delamination. However, the only parameters to be correctly identified correspond to the onset and evolution of intra-laminar damage during stages I and II. Conversely, the values for the parameters governing failure (stage III) were identified but the

dominant mode of failure changed from intra-laminar to inter-laminar, which the model was not developed to handle. This has two main implications:

- The numerical predictions showed in Figure 3-2 overshot the observed numbers of cycles at break because the model is not aimed at reproducing sudden failure in delamination.
- It is not possible to predict final failure due to pure intra-laminar damage using the current model parameters.

3 The NCF presents a relatively complex architecture and the mechanical behaviour and failure mode are highly dominated by the meso-structure of the material. However, the continuum damage model approach followed in Reference[43] is aimed to describe the material behaviour in an averaged sense, assuming local homogeneity of the damage distribution. This implies that the failure events occurring at the mesoscale due to stress concentrations at stitching-matrix interfaces or other architectural elements cannot be described with the current modelling approach.

4 Unified model intra- and inter- laminar damage

4.1 Objective

Failure of laminated composite materials is usually caused by fracture developments at the microstructure. In the case of the physical problem being analysed in this work, the stress concentrations at the tips of transverse matrix cracks when they reach the ply interfaces promote initiation of local delaminations (see Section 2.1 for a description of the physical problem).

Accurate modelling of the described phenomenon could be obtained if the observation scale was reduced to that close to the microstructural damage. In order to reproduce the physical matrix cracks, one could built a high fidelity continuum finite element model as showed in Figure 4-1.a. Using a continuum approach to fracture, damage would be understood as the progressive local loss of material integrity. When the damage becomes critical (i.e. approaches to 1), the material cannot sustain any stress and a crack is formed. However, CDMs do not properly describe the mechanical behaviour when the model scale approaches that of the microstructure of the material because the main assumption of these continuum models is local homogeneity of the microstructure. This is because the concept of continuum damage aims at describing the mechanical behaviour of the material in an averaged manner, even though the deformation processes at the microscale dominate the mechanical response of the material. In fact, upon mesh refinement, CDMs converge to damage localization in a volume set by the discretization size, while the properties of the surrounding material remain unaltered. As a result, instead of the intended progressive loss of material properties, the response approaches to perfectly brittle facture behaviour as the size of the discretization mesh tends to zero[55].

In this work, a coupled residual stiffness and strength model[43] is used to describe the deterioration of the composite material due to intra-laminar damage (transverse matrix cracks, diffused matrix cracking and fibre-matrix debonding). The reader is referred to Section 2.3 for a resume of the formulation governing the fatigue damage model. The macroscopic damage variables represent the structural changes at the microscale, measured through the degradation of the macroscopic stiffness. The final stage of failure is predicted using a fatigue failure index based on a modified use of the Tsai–Wu static failure criterion. Damage is considered to be uniform within the thickness of the ply (see Figure 4-1.b). A nonlocal approach is used in order to remove the above-mentioned mesh sensitivity of the CDM. The nonlocal variable is the fatigue failure index, which is added as an additional degree of freedom (see Section 5.1). By using the nonlocal approach, a length scale parameter is added to the continuum modelling, the nonlocal radius c, which is related to the spatial extension of the damage micro-processes.

In order to capture the delamination event, the interfaces between plies are modelled using cohesive elements (represented as blue lines in see Figure 4-1.b). The cohesive zone model formulation implemented into the interface elements is briefly described Section 2.4. The interfacial constitutive behavior is described in terms of the separation between the two initially coincident surfaces bounding the plies and the associated cohesive tractions that act to tie the surfaces together. Stiffness degradation is governed by a damage variable that is a function of the relative separation between plies.

From the observation of the physical damage process describe in Section 2.1, it is seen that at the regions with high density of matrix cracks the coalescence of micro-delaminations arising from matrix crack tips leads to a macroscopic delamination. These regions with significant matrix cracking are modelled with a high degree of intra-laminar damage, following the CDM approach (red-shadowed ply elements in Figure 4-1.b). If the two models are employed without a direct coupling between the damage evolving in both regions, the stiffness degradation due to intra-laminar damage will lead to high deformations within the ply. The neighbouring interface elements will not open and, thus, will not damage.

The development of an interaction formulation between the intra- and inter-laminar models aims at decreasing the apparent stiffness of the interface elements when they are close to a damaged ply

region (see Figure 4-1.c). As a result of intra-laminar damage, when the apparent stiffness of the interface element is reduced to zero a macro-delamination is formed. If, eventually, some out-of-plane loading is applied, the relative separation between plies will increase due to reduced interfacial stiffness and some inter-laminar damage will be generated. From this point on, the delamination will propagate (see Figure 4-1.d) due to progressive damage growth and stress redistribution at the region in front of the delamination front tip.

It is worth noting that, even though the developed formulation has only been applied to fatigue damage in the present work, it is not precluded from being also applied to quasi-static damage models.

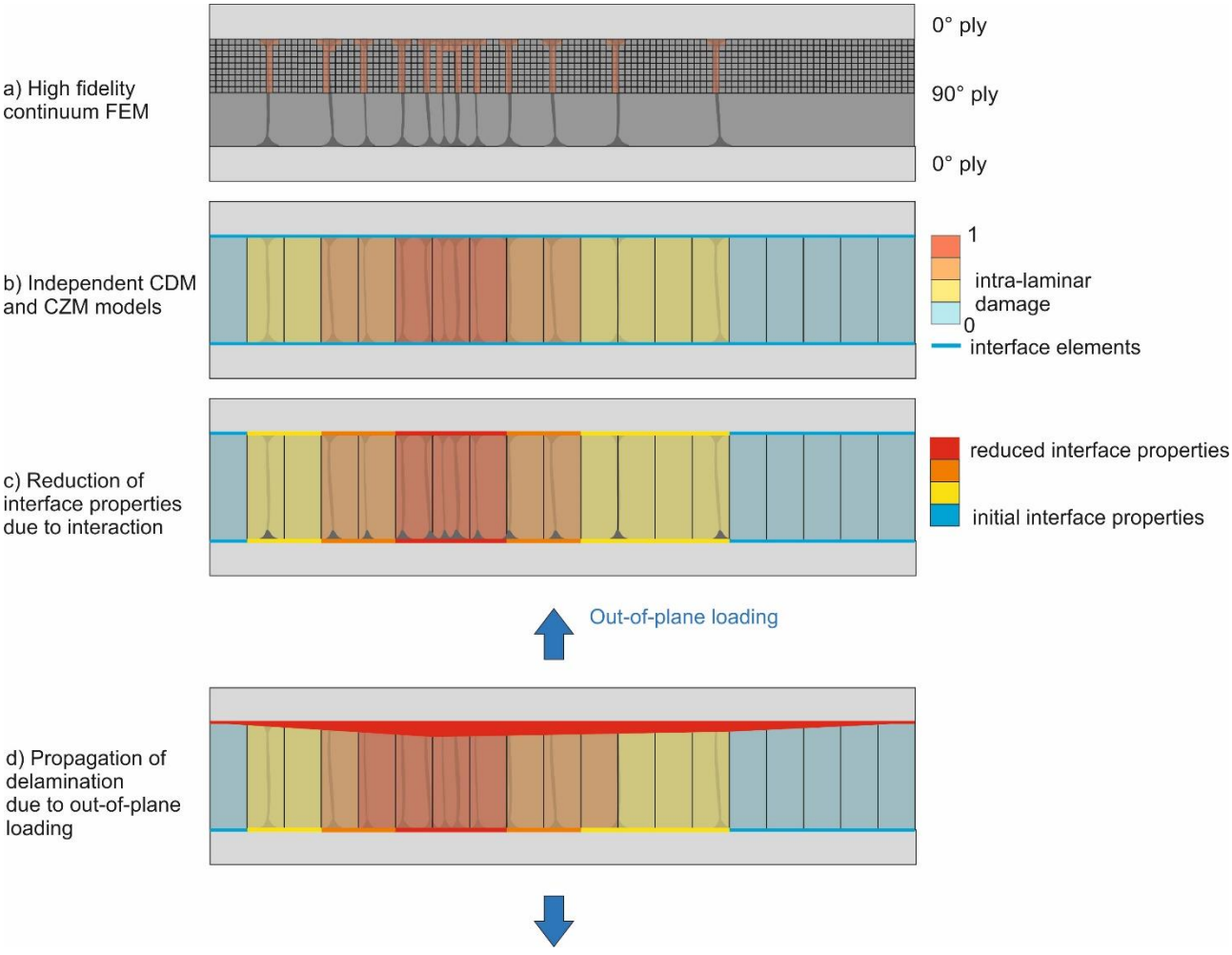

Figure 4-1. Modelling approach and desired fracture behaviour

4.2 Interaction criterion

The interaction criterion aims at linking the apparent stiffness of the interface elements to the damage at the surrounding ply elements. To do so, the performance of the interface element is compared to that of a system of springs in series (see Figure 4-2). One spring (coh) represents the cohesive behaviour according to the formulation presented in Section 2.4. The other spring (mat) represents the contribution of the matrix damage occurring at the surrounding ply elements. In each opening mode direction $i = 1,3$ (see Section 2.4), the total displacement jump of the ensemble is the sum of the displacement jumps of the individual springs:

$$\delta^i_{inter} = \delta^i_{coh} + \delta^i_{mat} \qquad \text{Eq. 4-1}$$

and the equivalent stiffness is calculated as:

$$k_{inter}^{i} = \frac{k_{coh} k_{mat}^{i}}{k_{coh} + k_{mat}^{i}} \qquad \text{Eq. 4-2}$$

where k_{coh} is the stiffness computed according to the cohesive zone model formulation presented in Section 2.4 and k_{mat}^{i} is the stiffness that is directly linked to the damage at the surrounding ply elements.

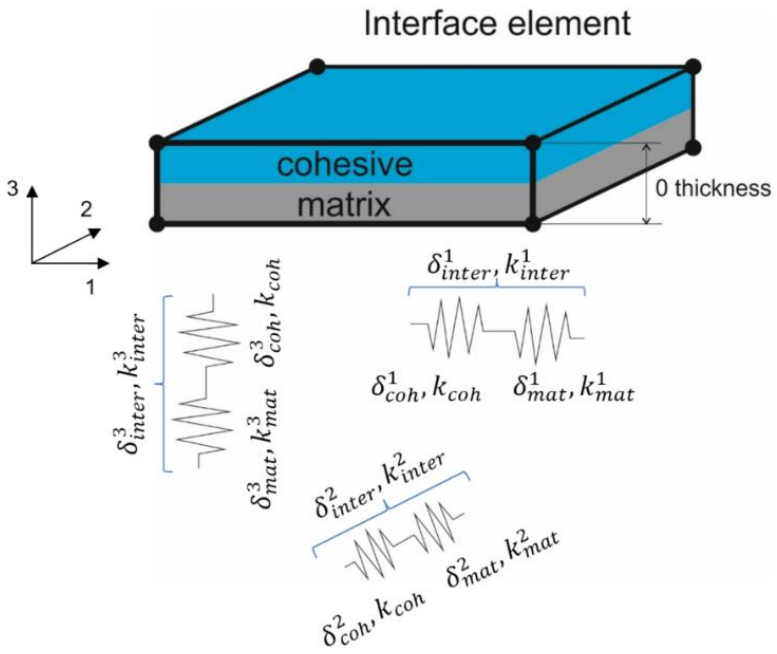

Figure 4-2. Schematic of a 8-node interface element with the effective stiffness and displacement jump in each mode direction represented as a simile with series springs

The stiffness of the cohesive zone model, k_{coh}, is mode-independent (see Eq. Eq. 2-18) and equal to:

$$k_{coh} = \left(1 - \mathcal{D}^{k}\right) K \qquad \text{Eq. 4-3}$$

where K is the penalty stiffness. On the contrary, k_{mat}^{i} is mode-dependent and it is computed as:

$$k_{mat}^{i} = \left(1 - \frac{D_{22}}{A_3}\right)^{\alpha_i} \left(1 - \frac{D_{12}}{A_4}\right)^{\beta_i} K \qquad \text{for } i = 1{,}2$$

$$k_{mat}^{3} = \left(1 - \frac{D_{22}}{A_1}\right)^{\alpha_3} \left(1 - \frac{D_{12}}{A_2}\right)^{\beta_3} K \qquad \text{Eq. 4-4}$$

where D_{22} is the transverse intra-laminar damage (i.e. in-plane normal to the fibre direction) and D_{12} is the in-plane shear intra-laminar damage. In the implementation of the coupled intra- and inter-laminar fatigue damage model, the user decides whether it is the maximum D_{22} and D_{12} between the two subsequent plies or the mean value. The exponents α_i and β_i for $i = 1{,}3$ and coefficients A_j for $j = 1{,}4$ are fitting parameters that serve to adjust the interaction behaviour to the experimental observations. Note that k_{mat}^{i} for $i = 1{,}3$ acts to decrease the stiffness of the interface element as a function of the damage state at the surrounding ply elements. However, the stiffness of the cohesive zone model, k_{coh}, remains unchanged and so the damage variable, $\mathcal{D}^{k}$. In other words, the apparent

stiffness of the interface is decreased only due to surrounding matrix damage. This causes the interface to open and the crack opening governs the damage state at the interface according to the CZM formulation. Thus, the energy dissipated at the interface is only due to cohesive failure.

According to the CZM formulation presented in Section 2.4, the damage variable, $\mathcal{D}^k$, is a function of the components of the displacement jump. Thus, in order to update the damage state at the interface, $\mathcal{D}^k$, which is only due to cohesive failure, the total displacement jumps δ_{inter}^i must be decomposed into the matrix damage contributing opening, δ_{mat}^i, and the displacement jump due to cohesive failure, δ_{coh}^i. By using the relation between the two springs connected in series, δ_{coh}^i is computed as :

$$\delta_{coh}^i = \delta_{inter}^i \frac{k_{mat}^i}{k_{coh} + k_{mat}^i} \qquad \text{Eq. 4-5}$$

Note that the components of the displacement jump depend on the stiffness of the cohesive zone model, $\delta_{coh}^i = f(k_{coh})$, which, in turn, depends on the damage variable, $\mathcal{D}^k$. Thus, in the finite element implementation, a Newton-Raphson method is used in order to integrate the behaviour law and update the damage at the next pseudo-time increment (see Section 5.2).

5 Implementation into Simcenter Samcef

In tasks 5.1 and 5.2, inter- and intra-fatigue damage models were implemented in Simcenter Samcef solver via two behaviour laws (FATIUP and FATINT). In this task 5.3, both models are coupled into a unified formulation that allows interaction between the damage states at the two regions.

5.1 Communication of intra-laminar damage to interface element

To communicate the fatigue damage state from the ply to the interface element, the non-local feature is used. It enables to communicate the material parameters of the ply elements and the nonlocal variable to the interface element. The non-local variable is the fatigue failure index described in Section 2.3.2. With the available information of material parameters and fatigue failure index, the damage variable is recalculated at the interface element level by integrating the equations of the damage rates (see equations Eq. 2-14 - Eq. 2-16) over the cycle jump.

$$\frac{\mathrm{dd}_{\mathrm{ij}}^{\pm}}{dN} = f(\Sigma_{ij}^{nloc}) \qquad \text{Eq. 5-1}$$

$$\begin{cases} \int \delta\underline{\varepsilon}\underline{\sigma} dV = \delta\underline{q}F \\ \int \delta\nabla\underline{\Sigma} c^2 \nabla\underline{\Sigma} + \delta\underline{\Sigma}^{nloc}\left(\underline{\Sigma}^{nloc} - \underline{\Sigma}\right) dV = 0 \end{cases} \qquad \text{Eq. 5-2}$$

where c is the non-local radius

$$\begin{bmatrix} d\underline{\sigma} \\ -d\underline{\Sigma} \end{bmatrix} = \begin{bmatrix} \underline{\underline{H}}\,\underline{\underline{S}}^{-1}\underline{\underline{H}} & 0 \\ -\dfrac{\partial\underline{\Sigma}}{\partial\underline{\varepsilon}} & 0 \end{bmatrix} \begin{bmatrix} d\underline{\varepsilon} \\ d\underline{\Sigma}^{nloc} \end{bmatrix} \qquad \text{Eq. 5-3}$$

$$\frac{\partial\Sigma_{ij}}{\partial\varepsilon_{kl}} = \frac{\partial\Sigma_{ij}}{\partial\tilde{\sigma}_{kl}} \frac{\partial\tilde{\sigma}_{mn}}{\partial\sigma_{op}} \frac{\partial\sigma_{op}}{\partial\varepsilon_{st}} \qquad \text{Eq. 5-4}$$

$$\left[\frac{\partial\underline{\Sigma}}{\partial\underline{\tilde{\sigma}}}\right] = \begin{bmatrix} \dfrac{sign(\sigma_{11})}{X\sqrt{1-\left(\frac{\tilde{\sigma}_{22}}{Y}\right)^2-\left(\frac{\tilde{\sigma}_{12}}{S}\right)^2}} & \dfrac{\tilde{\sigma}_{22}|\tilde{\sigma}_{11}|}{XY^2\left(1-\left(\frac{\tilde{\sigma}_{22}}{Y}\right)^2-\left(\frac{\tilde{\sigma}_{12}}{S}\right)^2\right)^{\frac{3}{2}}} & \dfrac{\tilde{\sigma}_{12}|\tilde{\sigma}_{11}|}{XS^2\left(1-\left(\frac{\tilde{\sigma}_{22}}{Y}\right)^2-\left(\frac{\tilde{\sigma}_{12}}{S}\right)^2\right)^{\frac{3}{2}}} \\ \dfrac{\tilde{\sigma}_{11}|\tilde{\sigma}_{22}|}{YX^2\left(1-\left(\frac{\tilde{\sigma}_{11}}{X}\right)^2-\left(\frac{\tilde{\sigma}_{12}}{S}\right)^2\right)^{\frac{3}{2}}} & \dfrac{sign(\sigma_{22})}{Y\sqrt{1-\left(\frac{\tilde{\sigma}_{11}}{X}\right)^2-\left(\frac{\tilde{\sigma}_{12}}{S}\right)^2}} & \dfrac{|\tilde{\sigma}_{22}|\tilde{\sigma}_{12}}{YS^2\left(1-\left(\frac{\tilde{\sigma}_{11}}{X}\right)^2-\left(\frac{\tilde{\sigma}_{12}}{S}\right)^2\right)^{\frac{3}{2}}} \\ \dfrac{\tilde{\sigma}_{11}|\tilde{\sigma}_{12}|}{S\left(1-\left(\frac{\tilde{\sigma}_{11}}{X}\right)^2-\left(\frac{\tilde{\sigma}_{22}}{Y}\right)^2\right)^{\frac{3}{2}}} & \dfrac{\tilde{\sigma}_{22}|\tilde{\sigma}_{12}|}{S\left(1-\left(\frac{\tilde{\sigma}_{11}}{X}\right)^2-\left(\frac{\tilde{\sigma}_{22}}{Y}\right)^2\right)^{\frac{3}{2}}} & \dfrac{sign(\sigma_{12})}{S\sqrt{1-\left(\frac{\tilde{\sigma}_{11}}{X}\right)^2-\left(\frac{\tilde{\sigma}_{22}}{Y}\right)^2}} \end{bmatrix} \qquad \text{Eq. 5-5}$$

$$Diag\left(\frac{\partial\underline{\Sigma}}{\partial\underline{\tilde{\sigma}}}\right) = < \frac{sign(\sigma_{11})}{X} \quad \frac{sign(\sigma_{22})}{Y} \quad \frac{sign(\sigma_{12})}{S} > \qquad \text{Eq. 5-6}$$

5.2 Integration of the behavior law

In case of coupling, it is necessary to apply a Newton Raphson method to integrate the behaviour law, as explained in Section 4.2. The chosen unknowns are:

$$\underline{\beta} = \underline{\Sigma} = \underline{\tau}$$

$$p_i = \delta_{i,\mathrm{coh}} = \delta_i^{inter} - \frac{\beta_i}{k_{ii}^{mat}} \qquad \text{Eq. 5-7}$$

The residual equations are:

$$\underline{R}_{\beta} = \underline{\beta} - k\{(1-\mathcal{D}^k)\mathrm{p_i} - \mathcal{D}^k\langle -p_3\rangle\delta_{3i}\}$$

$$R_{pi} = p_i + \frac{\beta_i}{k_{ii}^{mat}} - \delta_i^{inter} \qquad \text{Eq. 5-8}$$

The non-null derivatives of the residual are:

$$\frac{\partial \underline{R}_{\beta}}{\partial \underline{\beta}} = \underline{\underline{I}}$$

$$\frac{\partial R_{\beta_i}}{\partial p_j} = -\mathrm{k}\left[\left(1-\mathcal{D}^k\right)\delta_{\mathrm{ij}} + \frac{\partial \mathcal{D}^k}{\partial \mathrm{p_j}}(p_i - \langle -p_3\rangle\delta_{3i}) - \mathrm{d}\left(\frac{\langle -p_3\rangle}{|p_3|}\delta_{3\mathrm{j}}\delta_{3\mathrm{i}}\right)\right]$$

$$\frac{\partial \underline{R}_{\beta}}{\partial \underline{\varepsilon}} = 0$$

$$\frac{\partial k_{lm}^{coh}}{\partial p_j} = -\mathrm{k}\left(1 + \delta_{3m}\frac{\langle -\delta_3^{coh}\rangle}{\delta_3^{coh}}\right)\frac{\partial \mathcal{D}^k}{\partial p_j}\delta_{lm} \qquad \text{Eq. 5-9}$$

$$\frac{\partial R_{pi}}{\partial p_j} = \delta_{ij}$$

$$\frac{\partial R_{pi}}{\partial \varepsilon_j} = -\delta_{\mathrm{ij}}$$

$$\frac{\partial R_{pi}}{\partial \beta_j} = \frac{1}{k_{ii}^{mat}}\delta_{\mathrm{ij}}$$

$$\frac{\partial \underline{\underline{\Sigma}}}{\partial \underline{\beta}} = \underline{\underline{I}}$$

For the first iteration, it is assumed a non-evolution of damage that enables to compute the displacement jump at the interface element and, thus, the cohesive stress.

5.3 Keywords

To activate the coupling, the ply region must be modelled with the non-local elements:

.HYP NON LOCAL *<element selection>*

The nonlocal method is activated with the command:

.AEL *<element selection>* NLOC *1|2|3*

where:

- **NLOC 1**: the fatigue failure index is constant over the element thickness, linear over the element surface and continuous from one element to the next one. The fatigue failure indices are linked to the "vertical" edges of the element.
- **NLOC 2**: the fatigue failure index is constant over the element thickness, constant (1st degree element) or linear (2nd order element) over element surface and not continuous from one element to the next one. Radius c is taken equal to 0. The fatigue failure indices are linked to the element.
- **NLOC 3**: this is the local version of the element.

The value of non-local radius, c, is set via the command:

.MAT	I material_number	
	NOM “material_name”	
	BEHA “FATIUP”	Behavior selection
	QYT c	

The additional material parameters for the inter-laminar behaviour law due to interaction are:

.MAT	I material_number	
	NOM “material_name”	
	BEHA “FATINT2”	Behavior selection
	EXPM α_I α_{II} α_{III}	Coupling exponents
	EXPN β_I β_{II} β_{III}	Coupling exponents
	COEC A_1 A_2 A_3 A_4	Coupling coefficients

5.4 Post processing

The available results in the post–processing module and their attributed code value are:

- X556 Fatigue damage components
    1. D_{11}
    2. D_{22}
    3. D_{12}

where X can have the values:

- 1: for node-based field output
- 3: for element-based field output
- 9: for element-based field output that is a function of time

5.5 Shared cycle jump strategy

Samtech has developed an equivalent procedure to the cycle-jump approach described in Reference[44] to perform the fatigue analysis in a more computationally efficient manner in terms of CPU time. The simulation skips cycles over which negligible stiffness degradation is deemed to occur. The damage evolution is instead updated at cycle increments, over which significant damage occurs, using an explicit computational scheme. The stress and stiffness matrices are computed during each significant cycle assuming constant damage throughout a given cycle jump. The inter- and intra-laminar damage models implemented in the Simcenter Samcef code only account for fatigue damage generated by mechanical loading applied in blocks of constant amplitude and frequency. An envelope load approach is used because it is more computationally efficient for high-cycle fatigue applications. Thus, it only models the maximum absolute cyclic load.

For the intra-laminar damage model, the number of cycles to jump, $\mathrm{NJUMP1}$, is estimated for each integration point according to the derivative, $\mathrm{dD/dN}$. The significant damage growth criterion, $\Delta \mathrm{D}$, is proposed in Reference[44] as a one dimensional state:

$$\Delta D = D_{N+NJUMP1} - D_N = \begin{cases} 10^{-20} \text{ if } D = 0 \\ 0.5D \text{ if } 0 < D \leq 0.2 \\ 0.1 \text{ if } D > 0.2 \end{cases} \quad \text{Eq. 5-10}$$

$$NJUMP1 = \frac{\Delta D}{\left.\frac{dD}{dN}\right|_N} \quad \text{Eq. 5-11}$$

The computation of NJUMP1 only considers the most dominant of three intra-laminar components (D_{11}, D_{12} and D_{13}). The damage accumulation and rate are the respective sum of d_{ij}^{+} and d_{ij}^{-} and their corresponding rates.

For the inter-laminar damage model, the computation of cycle jump, NJUMP1, at each integration point is obtained by dividing a target crack length extension, Δa, by the local crack growth rate, $\frac{da}{dN}$, at all the integration points in the model:

$$NJUMP1 = \frac{\Delta a}{\frac{da}{dN}} \quad \text{Eq. 5-12}$$

Once it is computed, NJUMP1 is stored for every integration point of the ply and interface elements. In order to avoid too small cycle jumps, which would be computationally ineffective, and to avoid too large cycle jumps to preserve numerical stability and accuracy, a statistical strategy is used. A maximum cycle jump, NCYMAX, is selected by the user, as well as the number of intervals in which the range from 0 to NCYMAX is divided. A NJUMP1 distribution is made by counting the number of integration points in the model with a NJUMP1 within each interval. All NJUMP1 that are higher than NCYMAX are not taken into account.

From this distribution, a repartition function (see Figure 5-1) is built. The global cycle jump, NJUMP, is the value such that a given percentage (PERCYC) of integration points is below NJUMP.

In order to compute between which intervals NJUMP will be, NJ1 and NJ2 are the number of jumps at the beginning and end of the interval and NP1 and NP2 the ordinate at the beginning and end of the interval. Then, NJUMP is computed as:

NJUMP = NJ1 + (PERCYC*NPOINT - NP1) * (NJ2 - NJ1) / (NP2 - NP1) Eq. 5-13

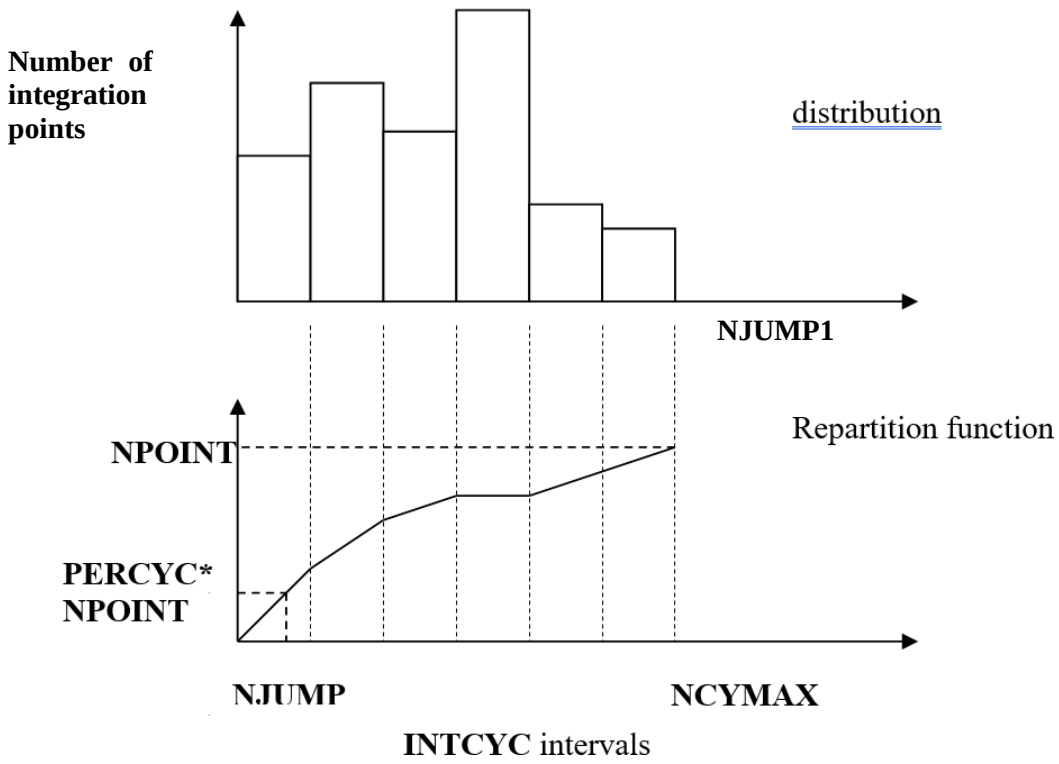

Figure 5-1: Distribution and repartition function used to identify the global cycle jump, NJUMP

6 Numerical case studies

6.1 Unit Test

Two composite volume unit elements linked with an interface element have boundary conditions in order to have a uniaxial stress state (see

Figure 6-1). The non-local aspect is set with the option NLOC 1. The fibers are oriented along X direction.

Case 6.1.1: A normal loading is applied to all faces located at Y = 1 mm with a value of 42.1 MPa in opposite Y-direction at a rate of 1 MPa/sec. After this loading ramp, the load remains constant to model a cyclic loading-unloading (envelope approach) with an amplitude of 42.1 MPa and a period of 1 s (see Figure 6-2). The material parameters are listed in Table 6-1.

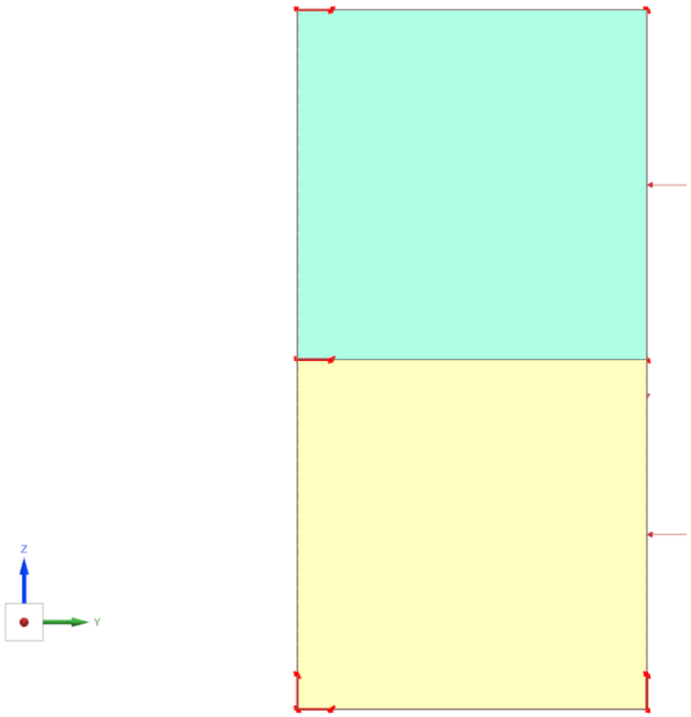

Figure 6-1. Unit test FEM

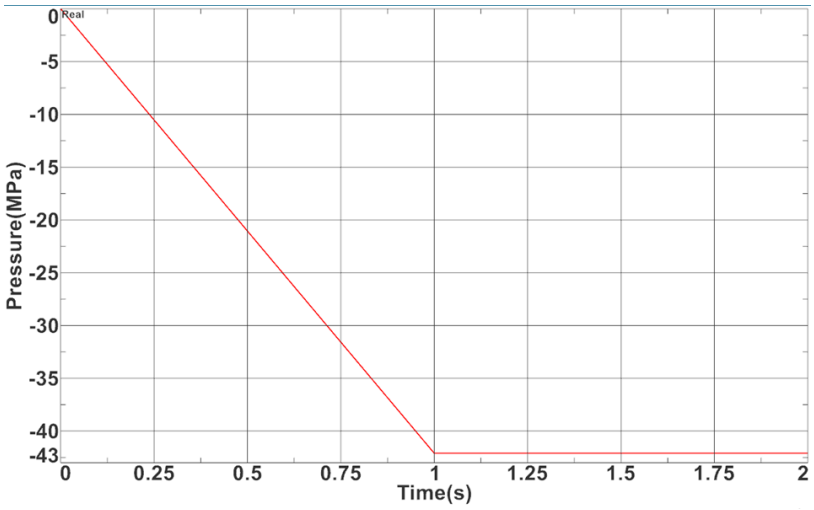

Figure 6-2: Applied pressure to unit test

Table 6-1: Material parameters of the ply

Laminate material properties			
E_{11} (MPa)	45000	c_{111}	10^{-4}
E_{22} (MPa)	13303	c_{112}	80.
E_{33} (MPa)	13303	c_{113}	4.10^{-4}
G_{11} (MPa)	4150	c_{114}	0.92
G_{23} (MPa)	1102	c_{115}	560
G_{13} (MPa)	2200	c_{221}	5.10^{-4}
ν_{12}	0.31	c_{222}	20
ν_{23}	0.28	c_{223}	10^{-4}
ν_{13}	0.25	c_{224}	0.0
X_T (MPa)	1102	c_{225}	0.0
X_C (MPa)	824	c_{121}	4.10^{-4}
Y_T (MPa)	84.2	c_{122}	30
Y_C (MPa)	167.8	c_{123}	10^{-6}
S (MPa)	107.5	c_{124}	0.9
		c_{125}	10000
		c_9	1.74
		D_{max}	0.999
		h	0.2

Table 6-2: Cohesive parameters of the interface

Cohesive law properties (FATINT)	
YT (k)	10^5
XT (τ_{Io}, τ_{sho})	10, 31.62
DCOU (η)	2
GC ($\mathcal{G}_{Ic}$, $\mathcal{G}_{shc}$)	0.3, 3
TAU (τ_c)	0.001
ADEL (a_c)	1
DDEN (d_{max})	1
YT (k)	10^5

Figure 6-3 shows the evolution of intra-laminar fatigue damage computed at both volume elements and at the interface element using the non-local option. The computed damage values at the three

different elements are equivalent, which validates the communication of damage from the ply to the interface element.

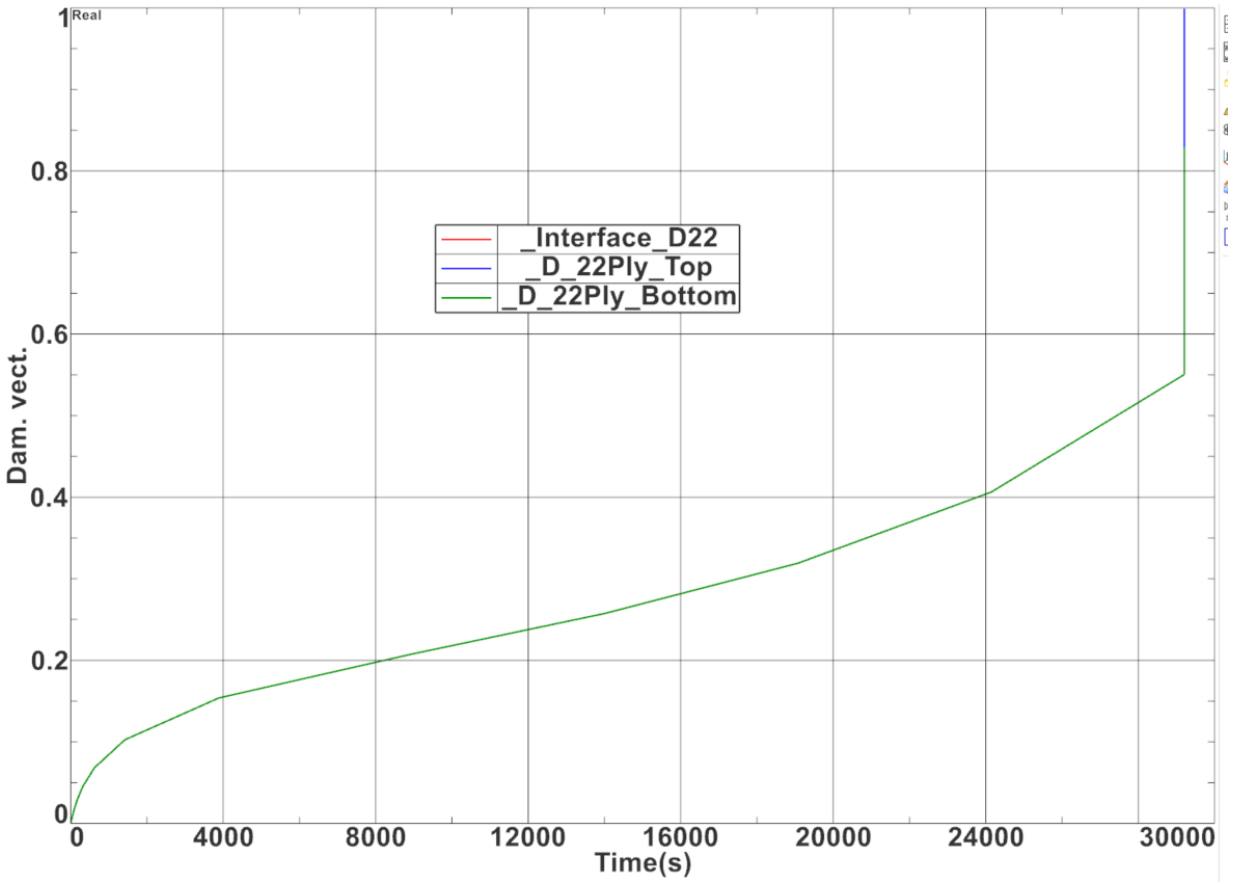

Figure 6-3: Evolution of interlaminar fatigue damage in all elements

Case 6.1.2: A displacement is applied on the top surface along Z direction. The value increases linearly from 0 to its maximum value of 0.1 mm during 1 second (see Figure 6-4). The coupled material model BEHA "FATINT2" is used with the extra parameters listed in Table 6-3, added to the ones listed in Table 6-1.

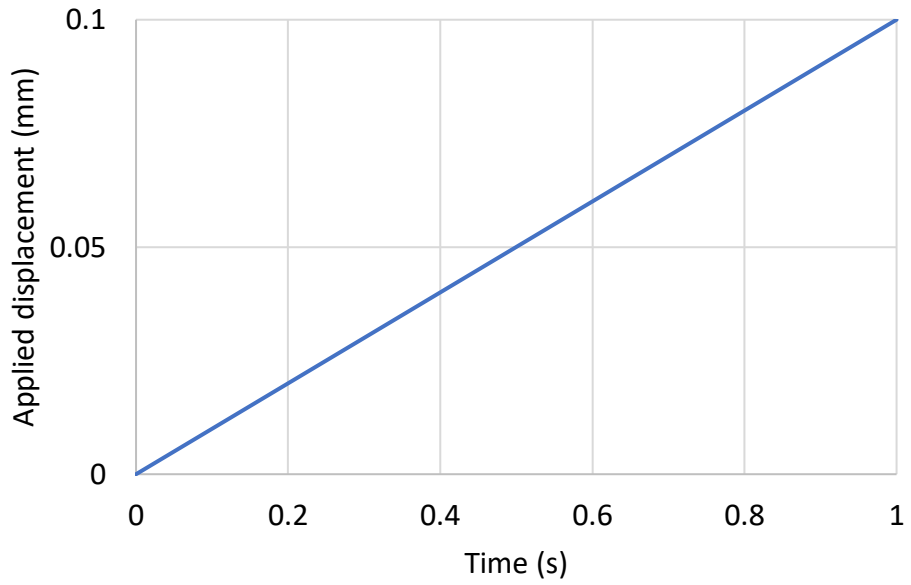

Figure 6-4: Applied displacement in unit test case 2

Table 6-3: Interaction parameters of the interface

Interaction parameters (FATINT2)	
$\alpha_I, \alpha_{II}, \alpha_{IIII}$	1, 1, 1
$\beta_I, \beta_{II}, \beta_{IIII}$	0, 0, 0
A_1, A_2, A_3, A_4	1, 1, 1, 1

Figure 6-5 shows the interlaminar stress τ_{33} vs. the equivalent displacement jump with (FATINT2) and without (FATINT) the coupling aspect. The two curves are superposed which reveals that the new material law with coupled aspect reproduces the interface behavior law correctly.

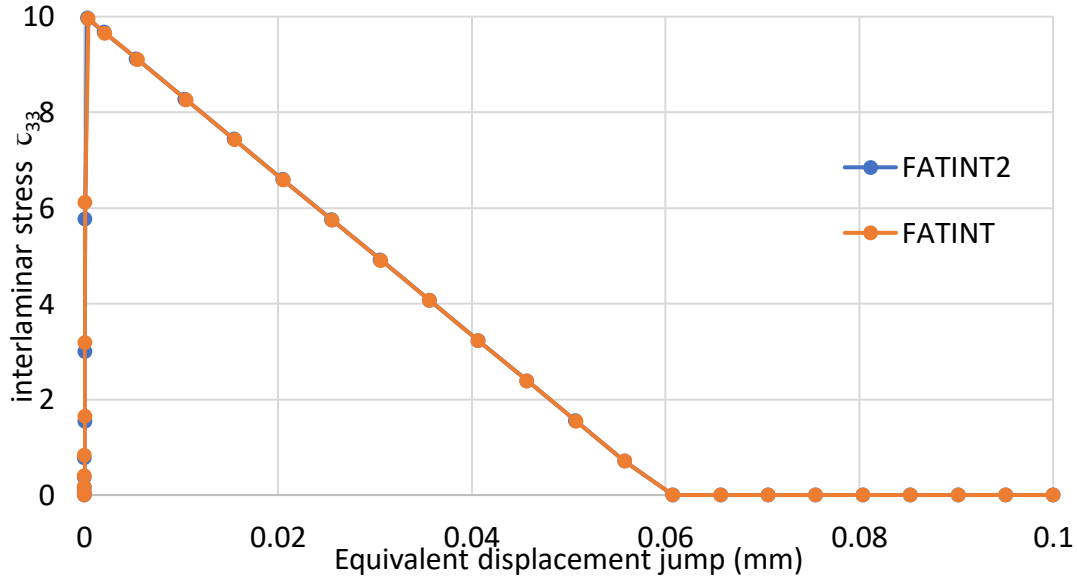

Figure 6-5: Equivalent displacement jump vs. interlaminar stress curves

Case 6.1.3: This case is performed in order to verify the effect of intra-laminar damage D_{22} on the global behavior of the interface element. First, the fatigue loading on the faces at Y = 1 mm described in Case 6.1.1 is applied. The fatigue analysis is stopped after 25 000 cycles. The intra-laminar fatigue damage D_{22} at this point is equal to 0.43. Then, the displacement loading along Z direction described in Case 6.1.2 is applied during 1 second to promote inter-laminar damage.

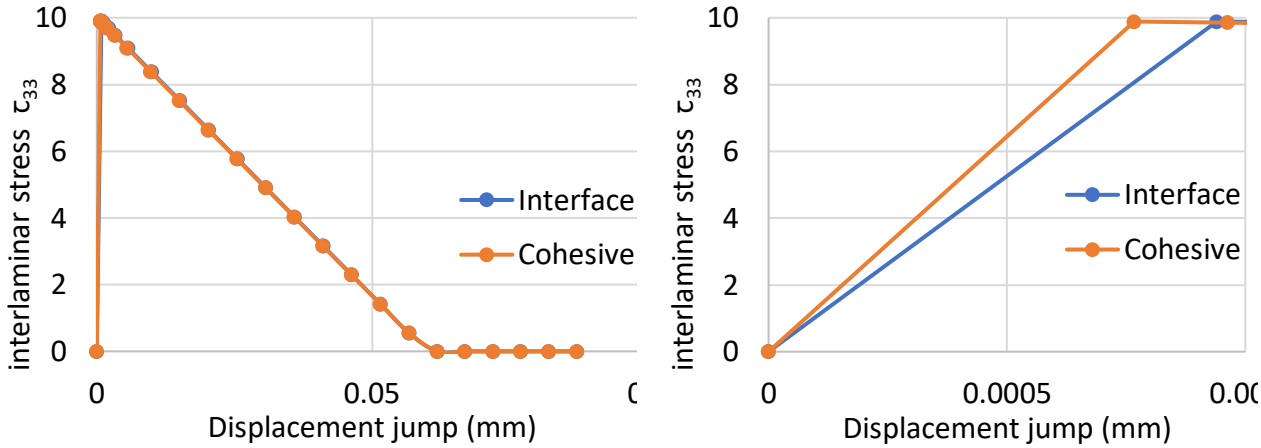

Figure 6-6 shows the evolution of the inter-laminar stress τ_{33} vs. the jump displacement of the cohesive part in the normal direction to the interface (δ_3^{coh}) and the total displacement jump of the interface element in the normal direction (δ_3^{int}). It can be observed that the cohesive softening is well reproduced using both displacement jumps. The initial stiffness of the interface element is calculated using the stress and the damage state. At the first converged time increment, as the D_{22} =0.43 and D_k =0.871, using the formulation given in Section 4.2, $k^{mat} = 56936\ MPa, k^{coh} = 12900\ MPa$, $k^{int} = 10518\ MPa$. These values are in agreement with the slopes of the two curves.

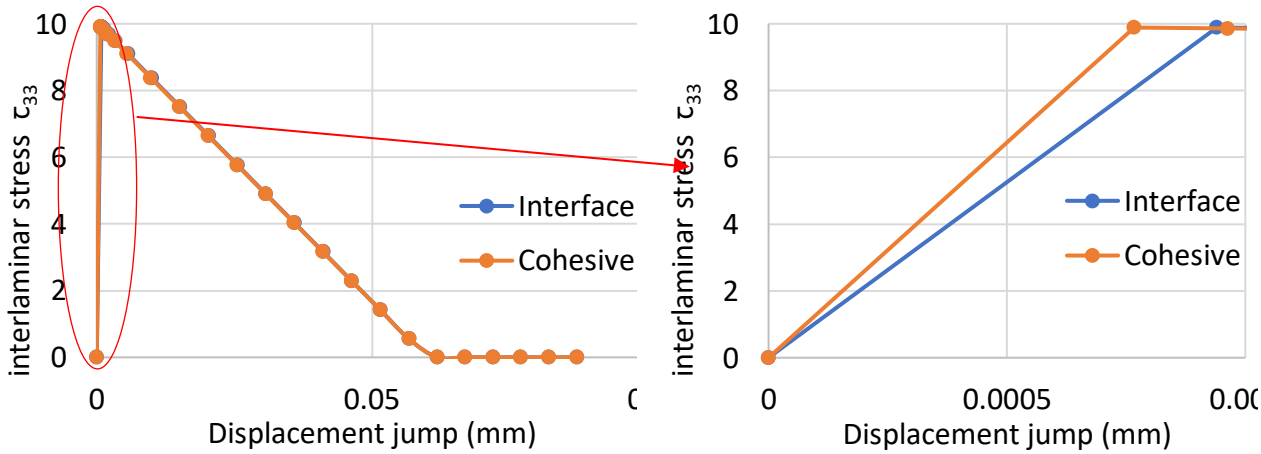

Figure 6-6: Equivalent displacement jump vs. interlaminar stress curves

6.2 Open hole tensile test

The sample dimensions are 108x36 mm with a hole diameter of 6 mm. The layup is $[90/0]_s$. The ply thickness is 1 mm. Only 1/8 of the sample is modeled due to symmetry. Each layer is modelled by an element thickness. The fixations correspond to the symmetry conditions. The displacement is prescribed at the top edge in the longitudinal direction with a displacement rate of 1mm/sec and an amplitude of 0.22 mm during 1 s and then a constant displacement is applied to model a cyclic loading-unloading with a frequency of 1 Hz by an envelope method until total failure of the sample.

Case 6.2.1. **The open hole specimen is modelled without interface elements between plies. The non-local aspect is applied with the option .AEL NLOC 1. The characteristic length c is equal to 0.5 mm. The results are compared to those obtained without the non-local aspect. To check the mesh effect on both cases (local and non-local), two mesh sizes are used (see Mesh1 Mesh2**

Figure 6-7). To sum up, the four simulation configurations analyzed in this case study are listed in Table 6-4.

Table 6-4. Simulations performed in Case 6.2.1.

Local	Mesh1 (coarse)	Represented in blue in Figure 6-8
Local	Mesh2 (fine)	Represented in green in Figure 6-8
Non-local	Mesh1 (coarse)	Represented in red in Figure 6-8
Non-local	Mesh2 (fine)	Represented in yellow in Figure 6-8

Figure 6-8 shows the evolution of the reaction force with respect to time. The local simulations show the impact of the mesh on the results. The fine mesh (green line) fails sooner than the coarse one (blue line). On the contrary, the two non-local simulations show equivalent results. Thus, showing to be mesh-independent. The non-local fine mesh simulation (yellow line) continues longer than the coarse one (red line) because the damage reaches the coarse mesh zone on the top of the specimen before. Figure 6-8 to Figure 6-12 show the evolution of the transversal damage in the 90° ply for the different simulations. The simulations with the non-local aspect show that the damage propagates from the hole (due stress concentration at the hole) to the rest of the specimen as the simulation advances. On the contrary, in the simulations without the non-local aspect, apart from showing mesh dependence, the distribution of damage does not propagate from the hole but it occurs at unconnected parts of the specimen. This is due to a numerical artifact probably caused by damage localization (see Section 4.1).

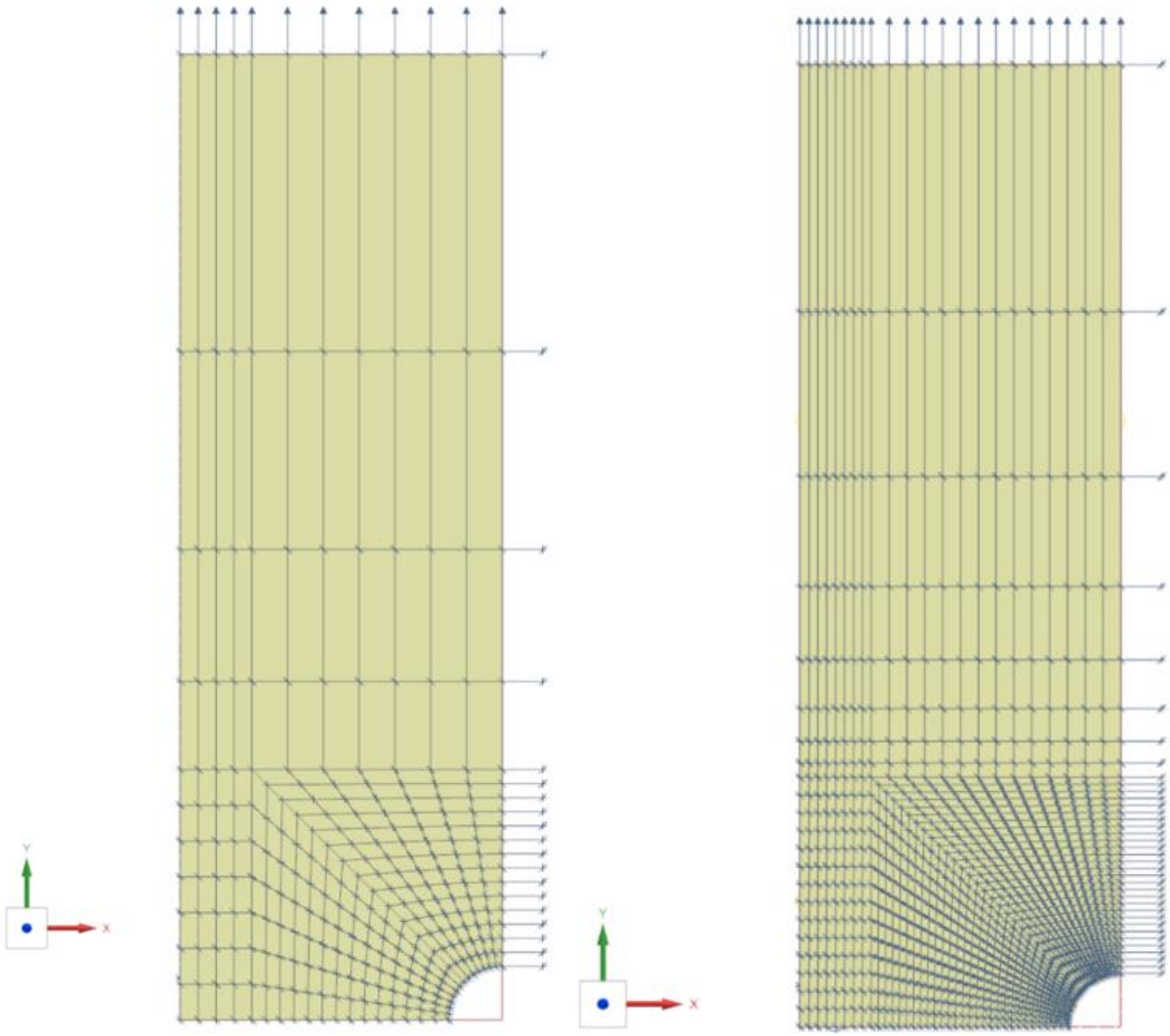

Mesh1 **Mesh2**

Figure 6-7. The two mesh sizes used in Case 6.1.1.

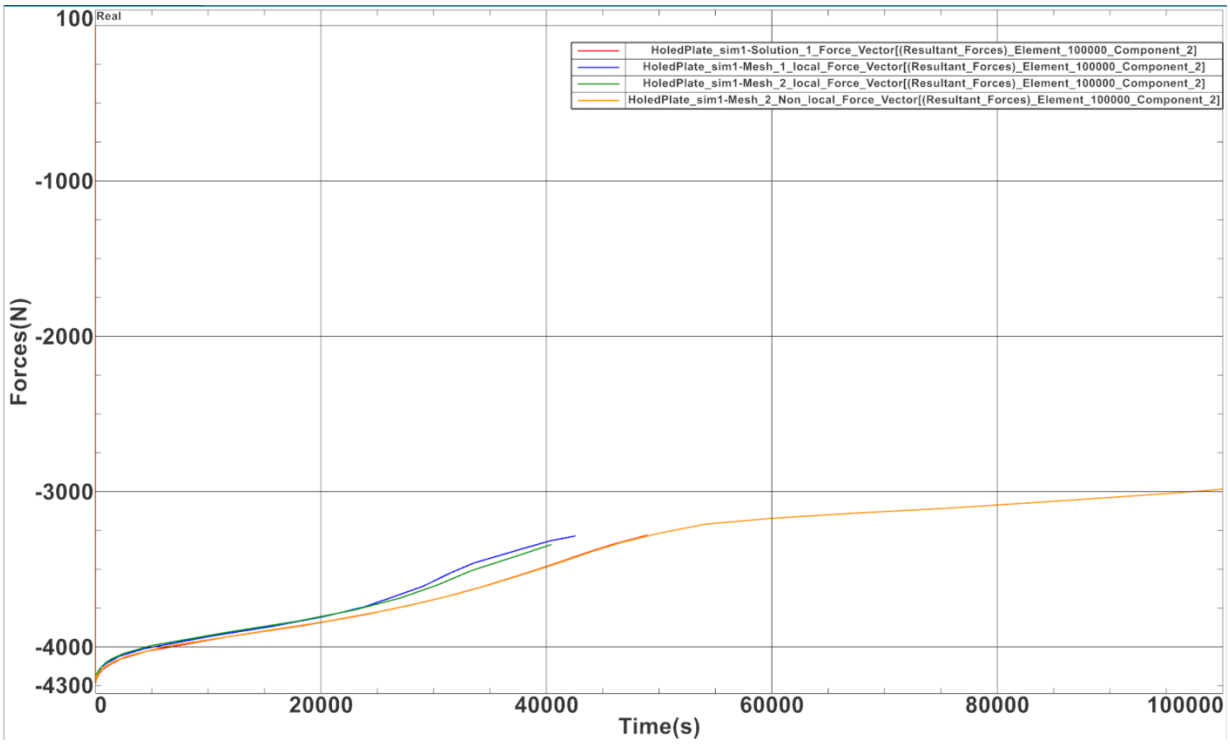

Figure 6-8: Evolution of the reaction in respect with the time

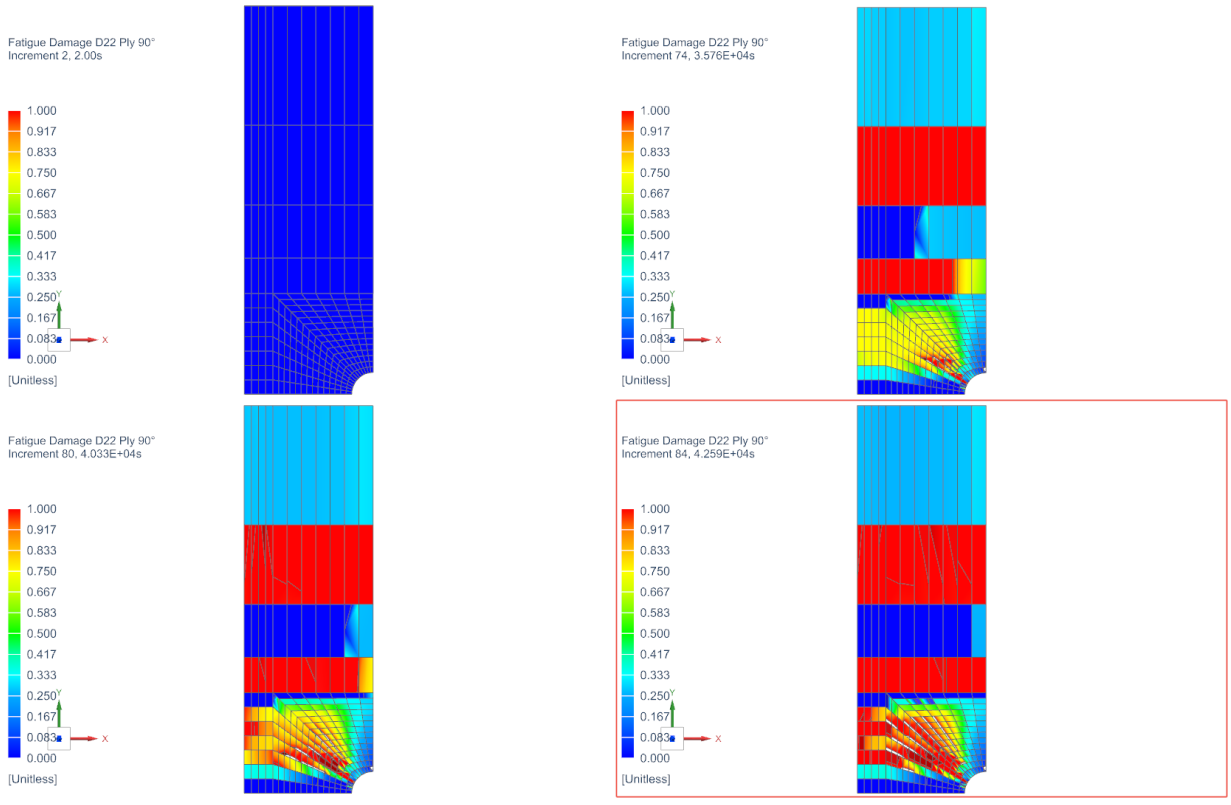

Figure 6-9: Evolution of Fatigue damage ply in 90° for Mesh 1 and local case

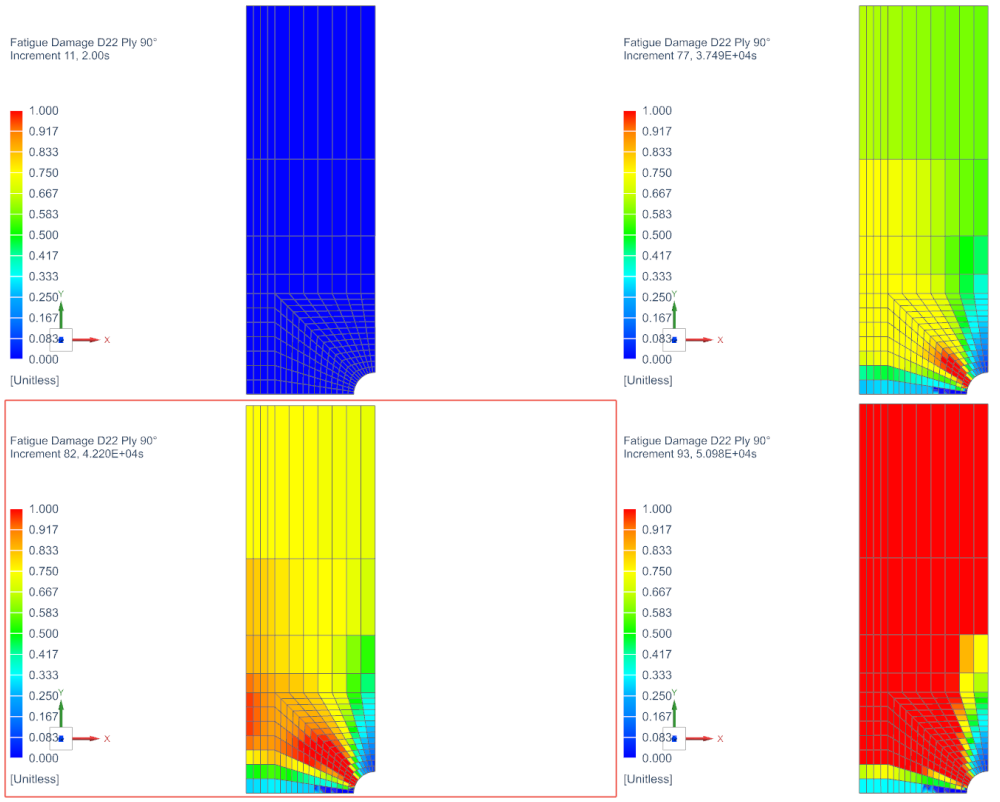

Figure 6-10: Evolution of Fatigue damage ply in 90° for Mesh 1 and non-local case

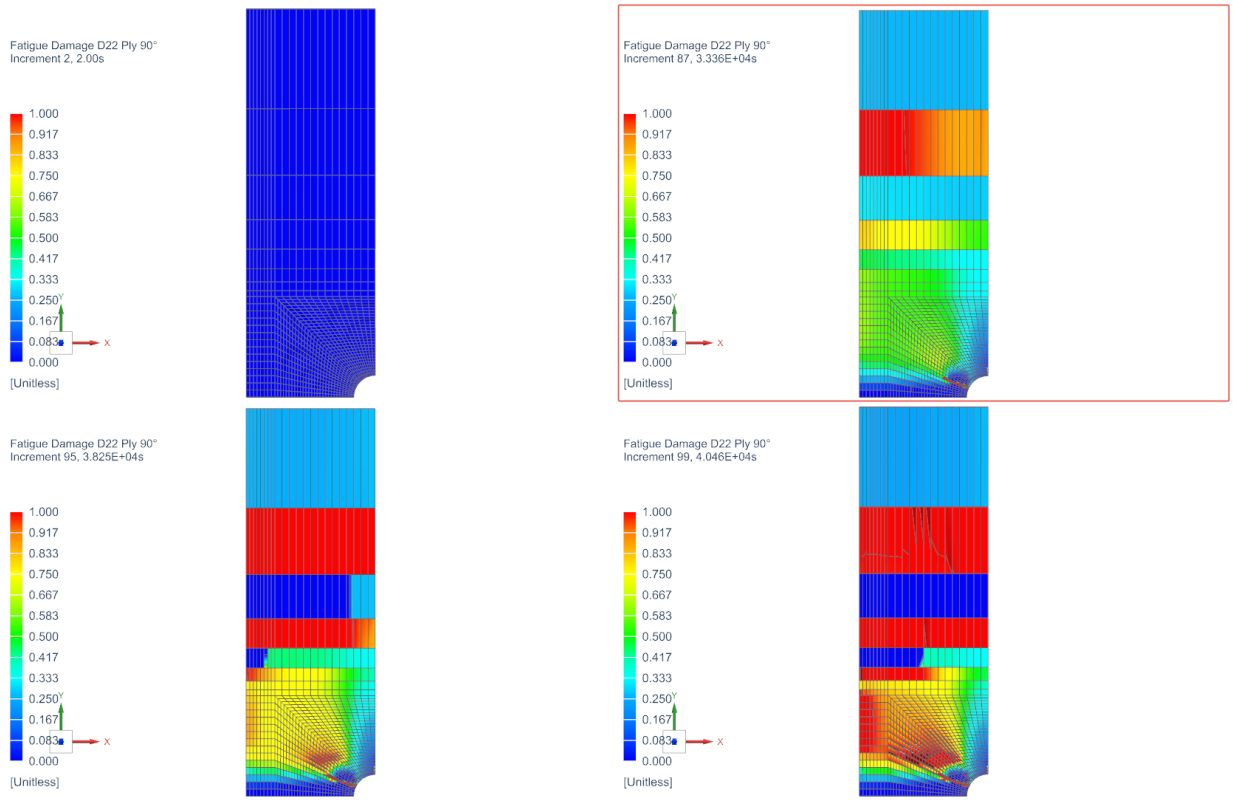

Figure 6-11: Evolution of Fatigue damage ply in 90° for Mesh 2 and local case

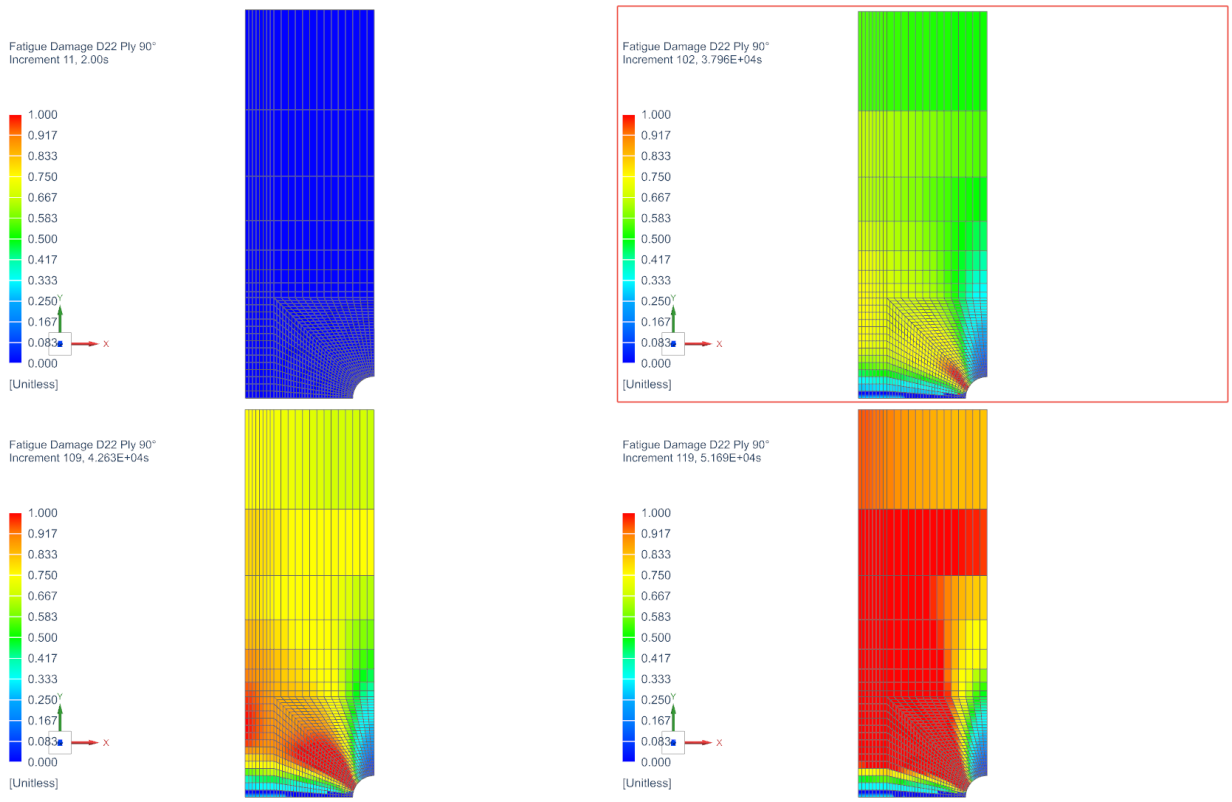

Figure 6-12: Evolution of Fatigue damage ply in 90° for Mesh 2 and non-local case

Case 6.2.2. The open hole specimen is modelled with interface elements between plies. The non-local aspect is always applied. The characteristic length c is equal to 0.5 mm. The fine mesh (Mesh2 in Figure 6-7) is used. The material properties of the plies are listed in Table 6-1. Different cohesive and interaction parameters of the interface are used to analyze the sensitivity of the results on the model parameters. The analysis has been performed without interface elements, with interface elements without and with interaction between the intra- and inter-laminar models (FATINT and FAINT2), with two different cohesive properties (M1-stronger, M2-weaker) and with different α-exponents in Eq. 4-4 (A01 – α_i = 0.1, A1 - α_i = 1, A10 - α_i = 10). The effect of the α-exponent on the reduction of the stiffness of the interface as a function of the ply damage (D22) is shown in Figure 6-13.

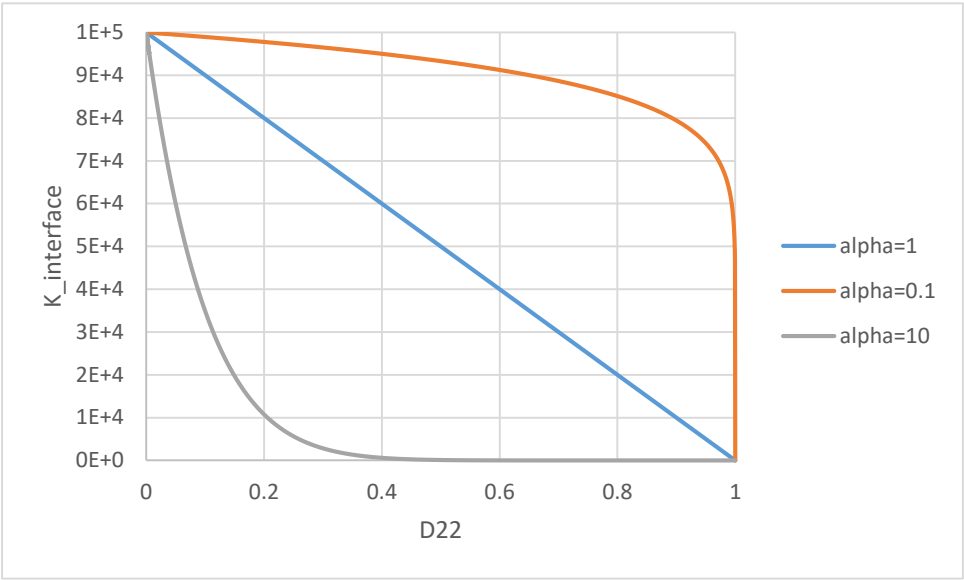

Figure 6-13. Effect of the α-exponent on the reduction of the stiffness of the interface.

The different simulation configurations of this case study are listed in Table 6-5.

Table 6-5. Simulations performed in Case 6.2.2.

Configuration ID	Cohesive law properties	Fatigue properties	Interaction properties
Without interface (Represented in yellow in Figure 6-14)	–	–	–

Configuration ID	Cohesive law properties		Fatigue properties		Interaction properties
FATINT_M1_OFAT (Represented in solid red in Figure 6-14)	YT (k)	10^5	CPAR (A_I, A_{sh}, A_m)	0.001, 0.001, 0.001	No interaction
	XT (τ_{Io}, τ_{sho})	10, 31.62	MPAR (p_I, p_{sh}, p_m)	1, 1, 1	
	DCOU (η)	2			
	GC ($\mathcal{G}_{Ic}$, $\mathcal{G}_{shc}$)	0.3, 3			
	TAU (τ_c)	0.001			
	ADEL (a_c)	1			
	DDEN (d_{max})	1			

Configuration ID	Cohesive law properties		Fatigue properties		Interaction properties
FATINT_M2_OFAT (Represented in dashed red with squared marker in Figure 6-14)	YT (k)	10^5	CPAR (A_I, A_{sh}, A_m)	0.001, 0.001, 0.001	No interaction
	XT (τ_{Io}, τ_{sho})	5, 10	MPAR (p_I, p_{sh}, p_m)	1, 1, 1	
	DCOU (η)	2			
	GC ($\mathcal{G}_{Ic}$, $\mathcal{G}_{shc}$)	0.1, 0.4			
	TAU (τ_c)	0.001			
	ADEL (a_c)	1			
	DDEN (d_{max})	1			

Configuration ID	Cohesive law properties		Fatigue properties		Interaction properties	
FATINT2_M1_OFAT_A01 (Represented in solid green with rounded marker in Figure 6-14)	YT (k)	10^5	CPAR (A_I, A_{sh}, A_m)	0.001, 0.001, 0.001	EXPM ($\alpha_I, \alpha_{II}, \alpha_{III}$)	0.1, 0.1, 0.1
	XT (τ_{Io}, τ_{sho})	10, 31.62	MPAR (p_I, p_{sh}, p_m)	1, 1, 1	EXPN ($\beta_I, \beta_{II}, \beta_{III}$)	0,0,0
	DCOU (η)	2			COEC (A_1, A_2, A_3, A_4)	1,1,1,1
	GC ($\mathcal{G}_{Ic}$, $\mathcal{G}_{shc}$)	0.3, 3				
	TAU (τ_c)	0.001				
	ADEL (a_c)	1				
	DDEN (d_{max})	1				

Configuration ID	Cohesive law properties		Fatigue properties		Interaction properties	
FATINT2_M1_OFAT_A1 (Represented in solid green in Figure 6-14)	YT (k)	10^5	CPAR (A_I, A_{sh}, A_m)	0.001, 0.001, 0.001	EXPM ($\alpha_I, \alpha_{II}, \alpha_{III}$)	1, 1, 1
	XT (τ_{Io}, τ_{sho})	10, 31.62	MPAR (p_I, p_{sh}, p_m)	1, 1, 1	EXPN ($\beta_I, \beta_{II}, \beta_{III}$)	0,0,0
	DCOU (η)	2			COEC (A_1, A_2, A_3, A_4)	1,1,1,1
	GC ($\mathcal{G}_{Ic}$, $\mathcal{G}_{shc}$)	0.3, 3				
	TAU (τ_c)	0.001				
	ADEL (a_c)	1				
	DDEN (d_{max})	1				

Configuration ID	Cohesive law properties		Fatigue properties		Interaction properties	
FATINT2_M1_OFAT_A10 (Represented in solid green with crossed marker in Figure 6-14)	YT (k)	10^5	CPAR (A_I, A_{sh}, A_m)	0.001, 0.001, 0.001	EXPM ($\alpha_I, \alpha_{II}, \alpha_{III}$)	10, 10, 10
	XT (τ_{Io}, τ_{sho})	10, 31.62	MPAR (p_I, p_{sh}, p_m)	1, 1, 1	EXPN ($\beta_I, \beta_{II}, \beta_{III}$)	0,0,0
	DCOU (η)	2			COEC (A_1, A_2, A_3, A_4)	1,1,1,1
	GC ($\mathcal{G}_{Ic}$, $\mathcal{G}_{shc}$)	0.3, 3				
	TAU (τ_c)	0.001				
	ADEL (a_c)	1				
	DDEN (d_{max})	1				

Configuration ID	Cohesive law properties		Fatigue properties		Interaction properties	
FATINT2_M2_OFAT_A1 (Represented in solid blue in Figure 6-14)	YT (k)	10^5	CPAR (A_I, A_{sh}, A_m)	0.001, 0.001, 0.001	EXPM ($\alpha_I, \alpha_{II}, \alpha_{III}$)	1, 1, 1
	XT (τ_{Io}, τ_{sho})	5, 10	MPAR (p_I, p_{sh}, p_m)	1, 1, 1	EXPN ($\beta_I, \beta_{II}, \beta_{III}$)	0,0,0
	DCOU (η)	2			COEC (A_1, A_2, A_3, A_4)	1,1,1,1
	GC ($\mathcal{G}_{Ic}$, $\mathcal{G}_{shc}$)	0.1, 0.4				
	TAU (τ_c)	0.001				
	ADEL (a_c)	1				
	DDEN (d_{max})	1				

Configuration ID	Cohesive law properties		Fatigue properties		Interaction properties	
FATINT2_M2_OFAT_A10 (Represented in dashed blue with squared marker in Figure 6-14)	YT (k)	10^5	CPAR (A_I, A_{sh}, A_m)	0.001, 0.001, 0.001	EXPM ($\alpha_I, \alpha_{II}, \alpha_{III}$)	10, 10, 10
	XT (τ_{Io}, τ_{sho})	5, 10	MPAR (p_I, p_{sh}, p_m)	1, 1, 1	EXPN ($\beta_I, \beta_{II}, \beta_{III}$)	0,0,0
	DCOU (η)	2			COEC (A_1, A_2, A_3, A_4)	1,1,1,1
	GC ($\mathcal{G}_{Ic}$, $\mathcal{G}_{shc}$)	0.1, 0.4				
	TAU (τ_c)	0.001				
	ADEL (a_c)	1				
	DDEN (d_{max})	1				

Figure 6-14 shows the evolution of the reaction force with respect to the number of cycles for all simulation configurations listed in Table 6-5. It can be observed that all the simulations show nearly the same structural response. However, some of them stop before the others due to convergence problems. The ones that run longer are with interface elements but without interaction between the intra- and inter-laminar models (FATINT).

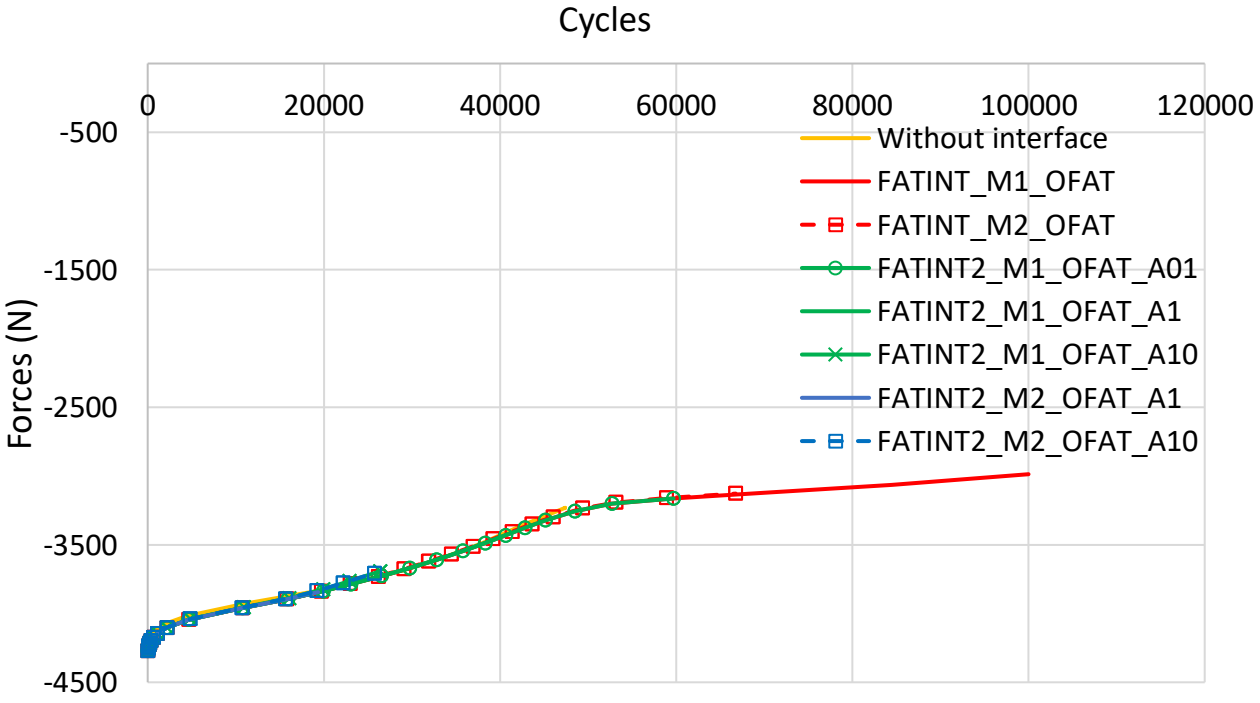

Figure 6-14. Evolution of the reaction force with respect to the number of cycles

In the following, the results without (FATINT) and with interaction (FATINT2) are compared for the different cohesive parameters and α-exponents listed in Table 6-5.

Table 6-6 shows the comparison without and with interaction using material M1 (with stronger cohesive properties than M2) and with α-exponent equal to 1. The first row of images shows the results are of the relative displacement at the interface in the global Y-direction (direction of the applied displacement at the top edge). The second row shows the damage at the ply (D22). The third row shows the cohesive damage variable (Dk), which reduces the cohesive stiffness of the interface (k_{coh}) due to pure inter-laminar damage. Finally, the fourth row shows the apparent stiffness of the interface. It can be observed that, for identical D22 and similar Dk, the model with the interaction criterion active shows an apparent interface damage evolution proportional to D22. The damage of the interface is equal to 1 at those regions where D22 is also equal to 1, thus introducing a pre-crack at the interface due to intra-laminar damage. On the contrary, the damage of the interface is not altered by intra-laminar damage when there is no interaction between the intra- and inter-laminar models. This might lead to too optimistic results if eventually some out-of-plane loading is applied since the structural resistance to delamination can be affected by the length of the interfacial pre-crack.

Table 6-6. FATINT-M1-OFAT and FATINT2-M1-OFAT-A1

<table>
<tr><td colspan="2">Relative displacement in Y direction (global frame)</td></tr>
<tr><td>FATINT-M1-OFAT</td><td>FATINT2-M1-OFAT-A1</td></tr>
<tr><td> 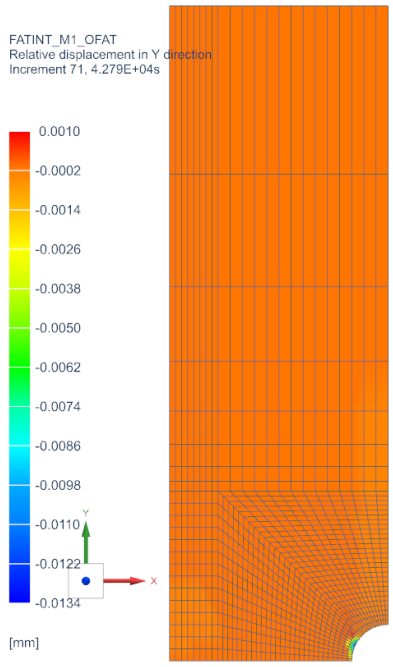
</td><td> 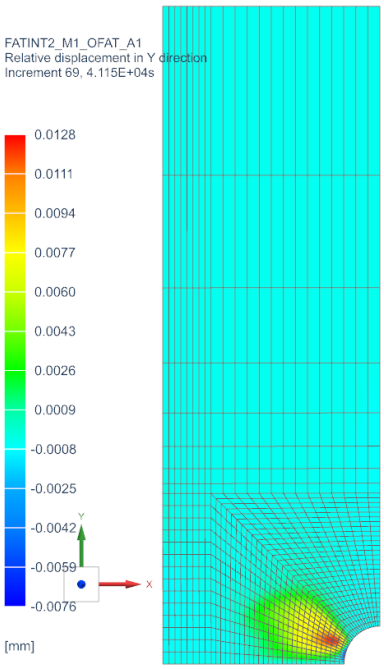
</td></tr>
<tr><td colspan="2">Matrix damage D22</td></tr>
<tr><td>FATINT-M1-OFAT</td><td>FATINT2-M1-OFAT-A1</td></tr>
</table>

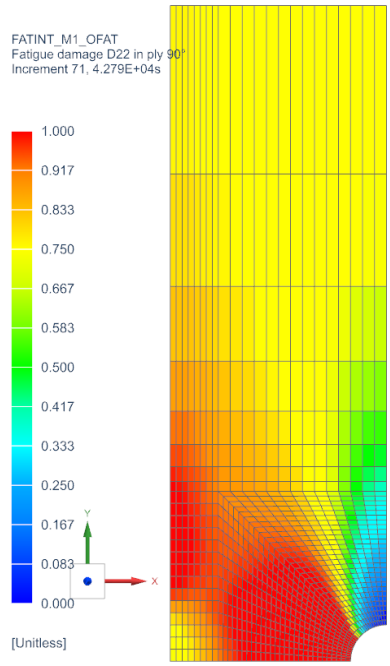

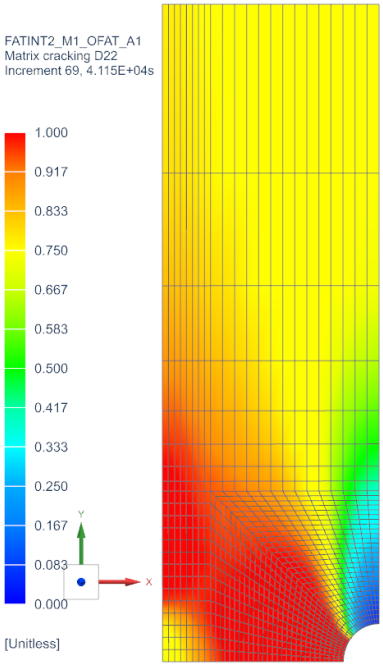

Interlaminar damage Dk

FATINT-M1-OFAT	FATINT2-M1-OFAT-A1

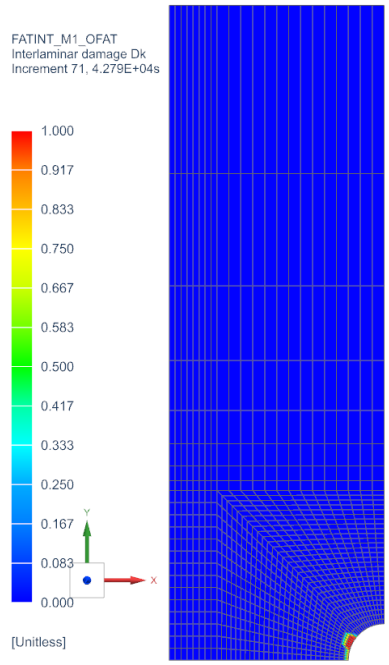

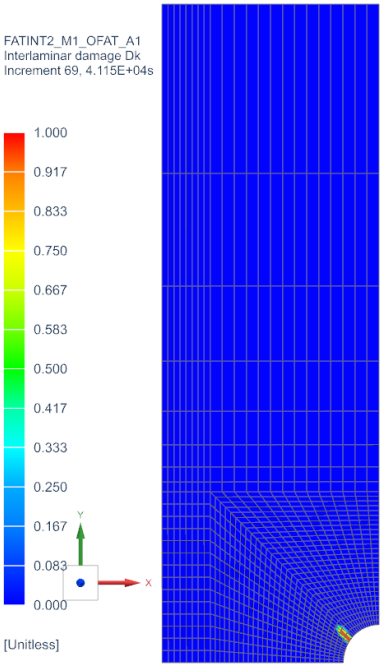

Damage of interface

FATINT-M1-OFAT	FATINT2-M1-OFAT-A1

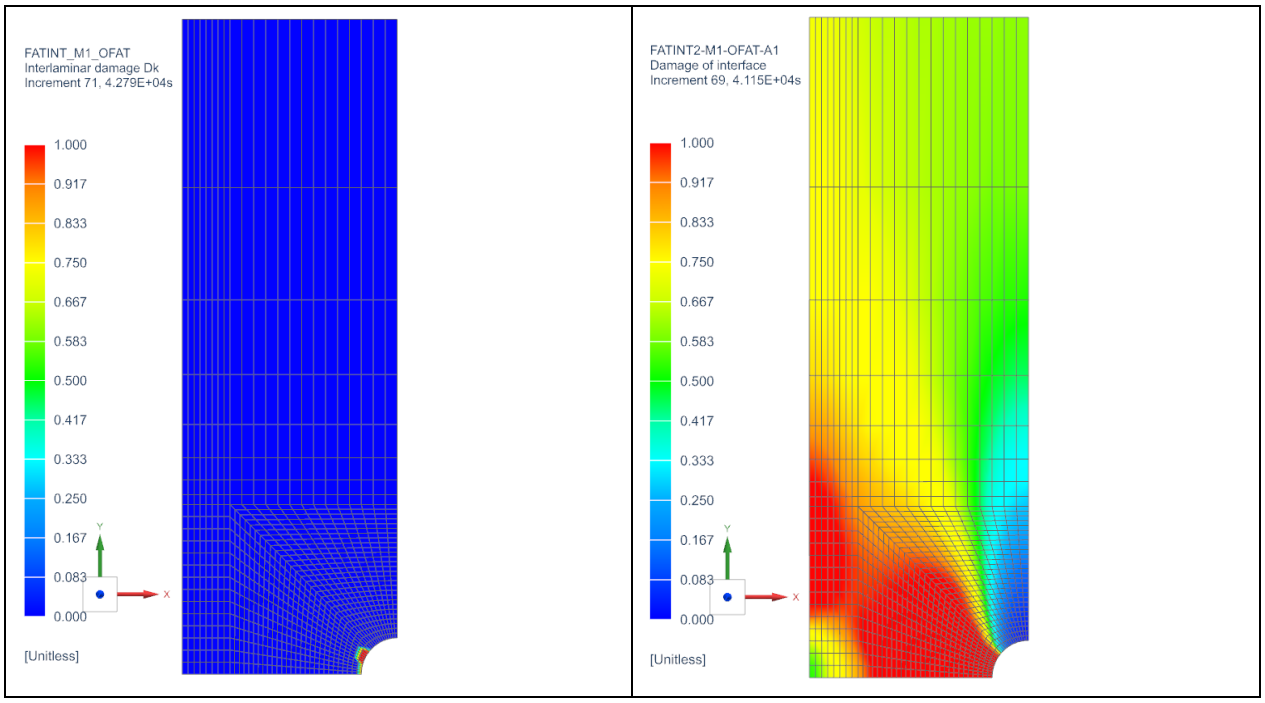

Table 6-7 shows the comparison without and with interaction using material M1 (with stronger cohesive properties than M2) and with α-exponent equal to 10. There is, again, similar D22 and Dk results between both simulations. In this case, the effect of D22 on the apparent stiffness reduction of the interface is accentuated by using a high α-exponent. It can be observed in Figure 6-13 that for low values of D22 the stiffness of the interfaces is already reduced to 0. This is in agreement with the plot of damage of the interface in the fourth row of Table 6-7 with the interaction activated. In this case, the premature reduction of the interface stiffness led to convergence problems and the simulation stopped at the half of the number of cycles compared to the previous one.

Table 6-7. FATINT-M1-OFAT and FATINT2-M1-OFAT-A10

Relative displacement in Y direction (global frame)	
FATINT-M1-OFAT	FATINT2-M1-OFAT-A10
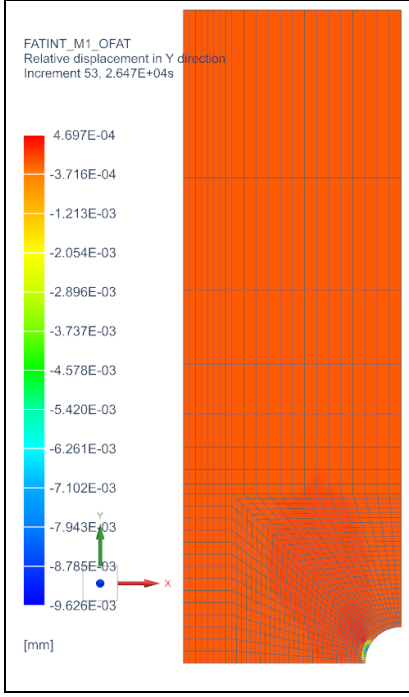	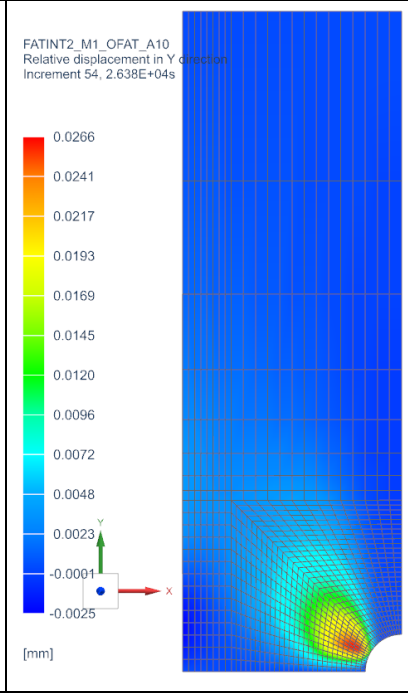

Matrix damage D22	
FATINT-M1-OFAT	FATINT2-M1-OFAT-A10
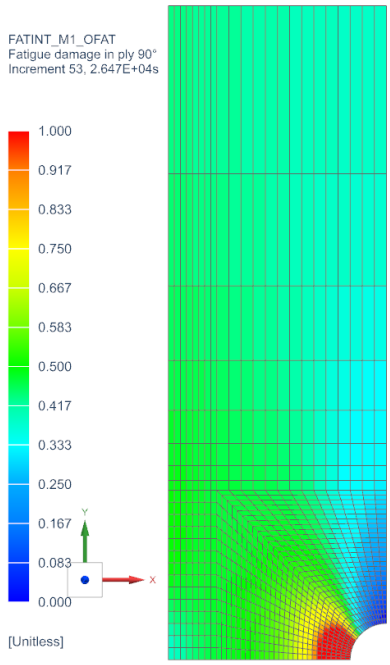	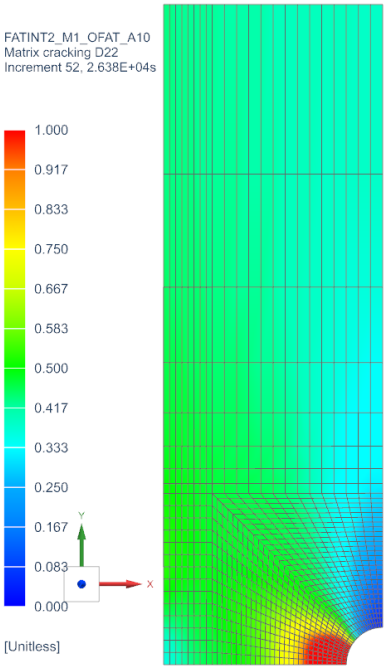
Interlaminar damage Dk	
FATINT-M1-OFAT	FATINT2-M1-OFAT-A10
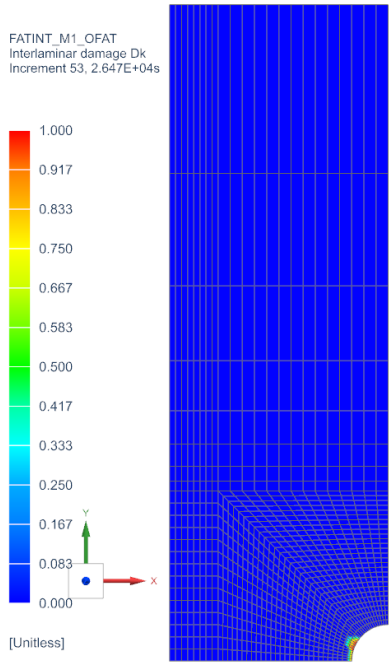	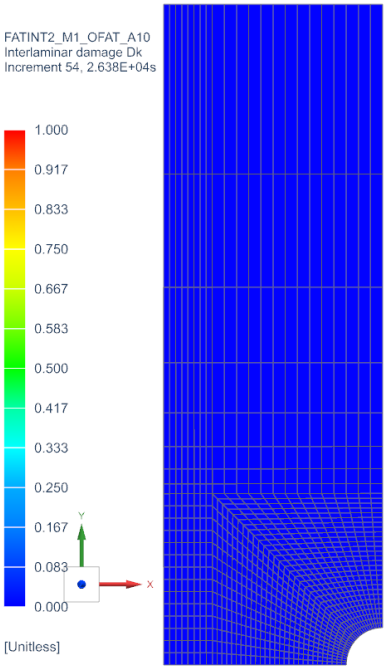
Damage of interface	
FATINT-M1-OFAT	FATINT2-M1-OFAT-A10

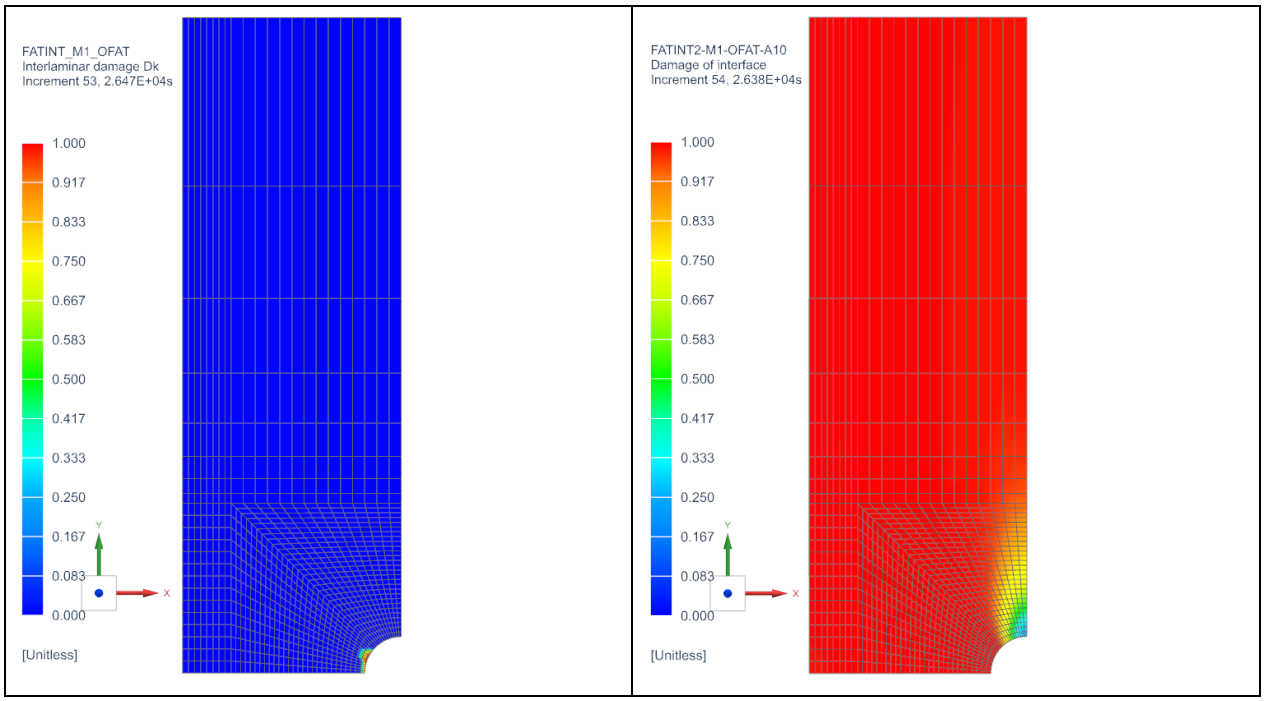

Table 6-8 shows the comparison without and with interaction using material M2 (with weaker cohesive properties than M1) and with α-exponent equal to 1. The results of D22 and Dk are similar between both simulations. In this case, the weak cohesive properties of the interface produce higher cohesive damage close the open hole and also at the specimen edge in the case without interaction. The effect of the interaction between the intra- and inter-laminar models on the apparent stiffness of the interface can be observed in the fourth row of images. While in the case without interaction the stiffness is only reduced due to cohesive failure, in the case of interaction, there is a reduction that spans the whole specimen at different degrees, likewise the distribution of D22.

Table 6-8. FATINT-M2-OFAT and FATINT2-M2-OFAT-A1

Relative displacement in Y direction (global frame)	
FATINT-M2-OFAT	FATINT2-M2-OFAT-A1
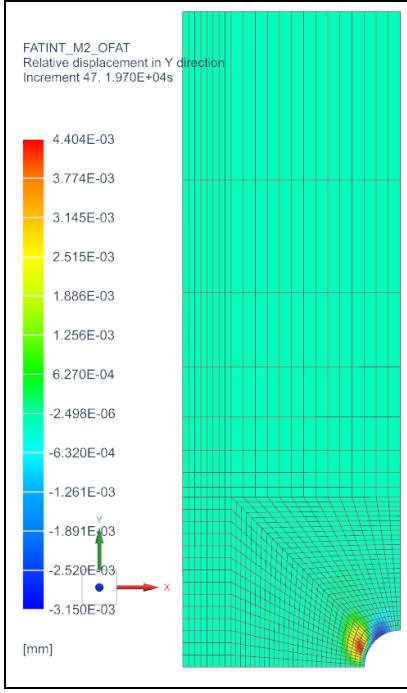	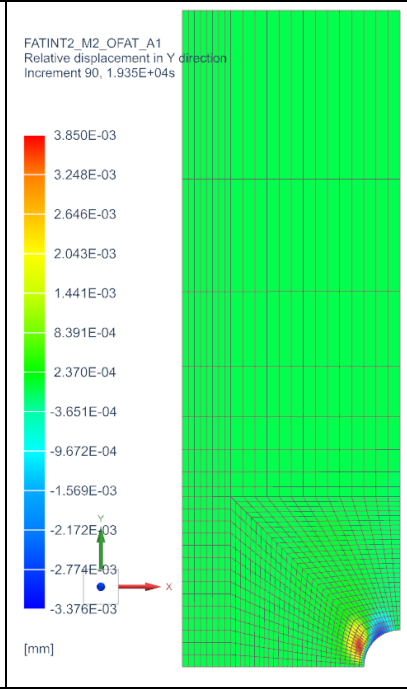

Matrix damage D22	
FATINT-M2-OFAT	FATINT2-M2-OFAT-A1
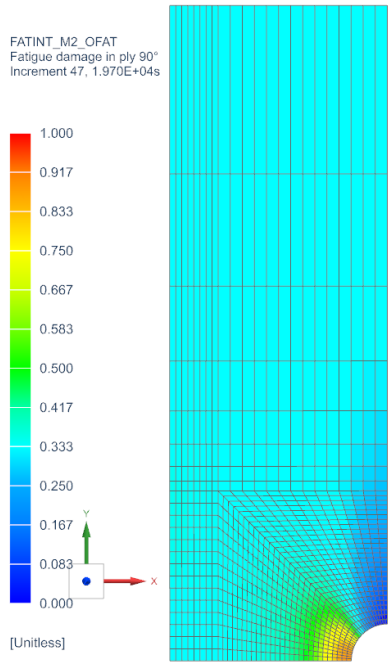	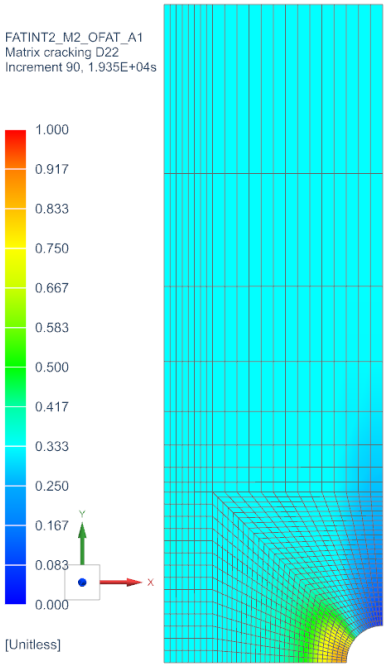
Interlaminar damage Dk	
FATINT-M2-OFAT	FATINT2-M2-OFAT-A1
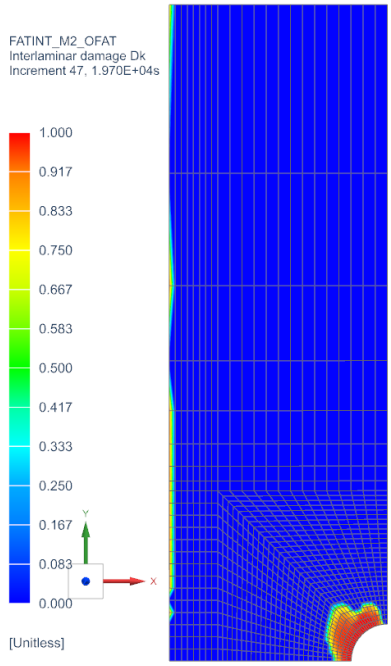	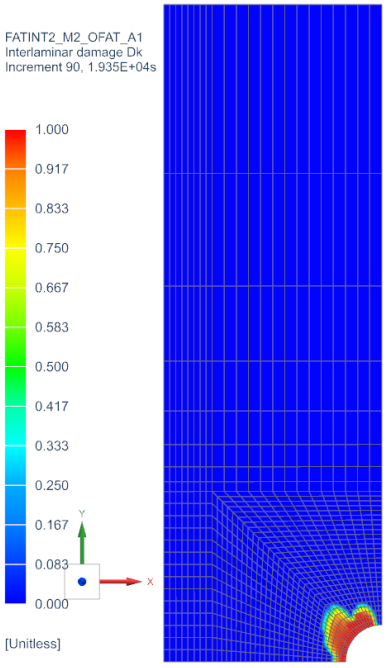
Damage of interface	
FATINT-M2-OFAT	FATINT2-M2-OFAT-A1

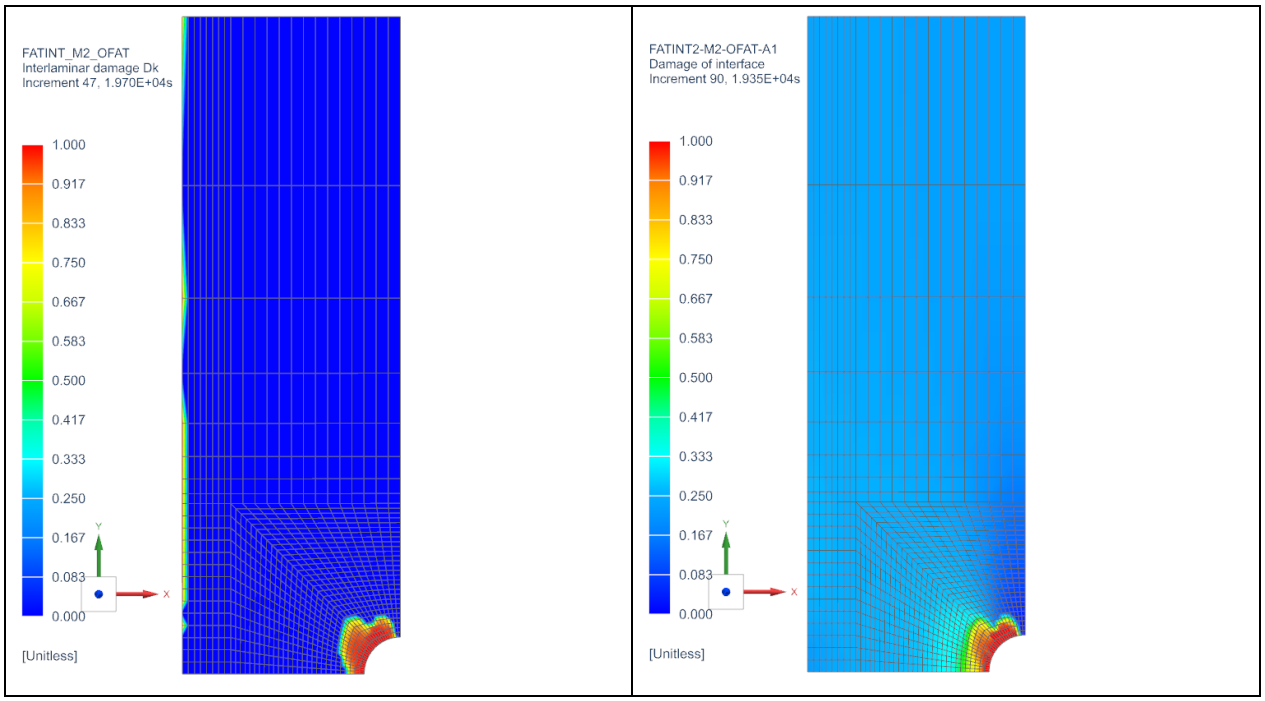

Table 6-9 shows the comparison without and with interaction using material M2 (with weaker cohesive properties than M1) and with α-exponent equal to 10. The results are close to those observed in Table 6-7, where low values of D22 have a high impact on the reduction of the apparent stiffness of the interface. Since the cohesive properties used in this simulation are weak, it can also be observed a bigger zone suffering delamination close to the open hole, like in Table 6-8.

Table 6-9. FATINT-M2-OFAT and FATINT2-M2-OFAT-A10

Relative displacement in Y direction (global frame)	
FATINT-M2-OFAT	FATINT2-M2-OFAT-A10
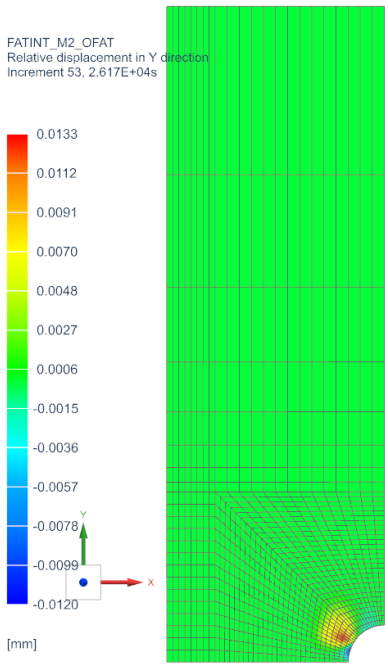	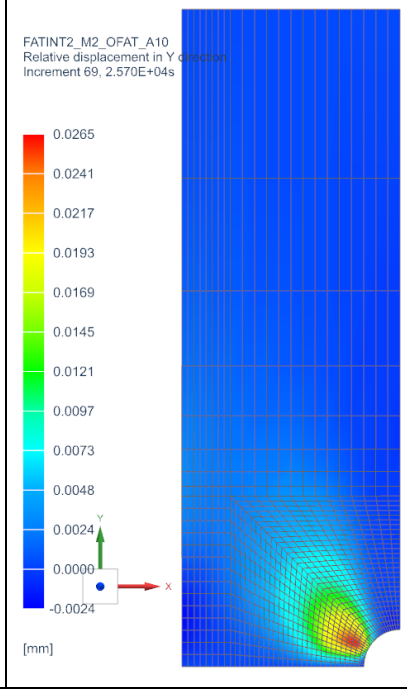
Matrix damage D22	

FATINT-M2-OFAT	FATINT2-M2-OFAT-A10
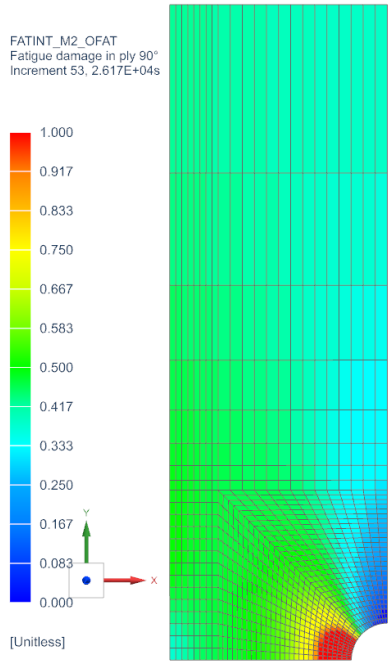	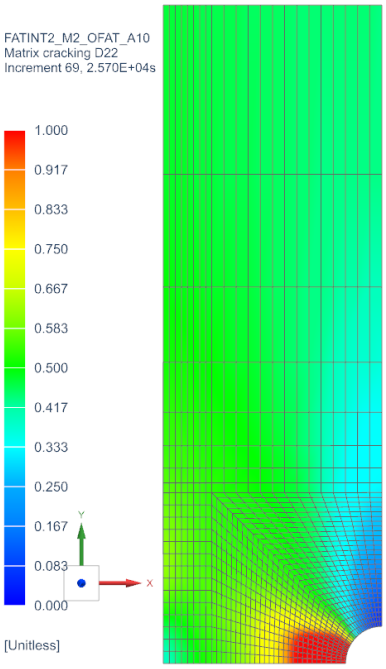
Interlaminar damage Dk	
FATINT-M2-OFAT	FATINT2-M2-OFAT-A10
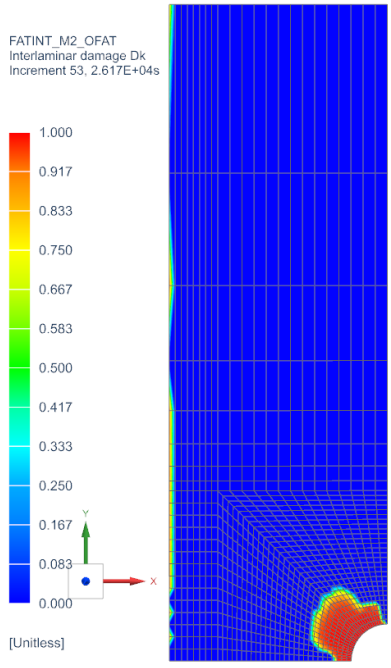	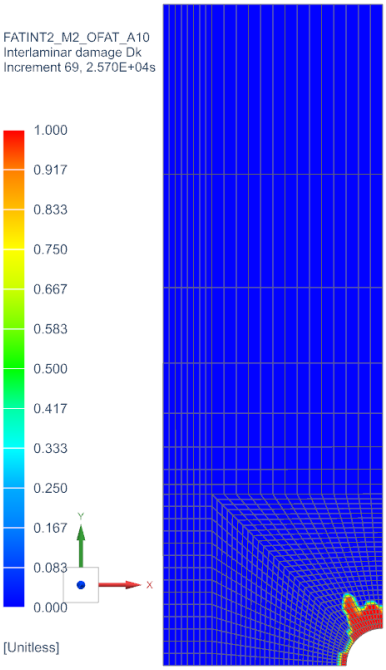
Damage of interface	
FATINT-M2-OFAT	FATINT2-M2-OFAT-A10

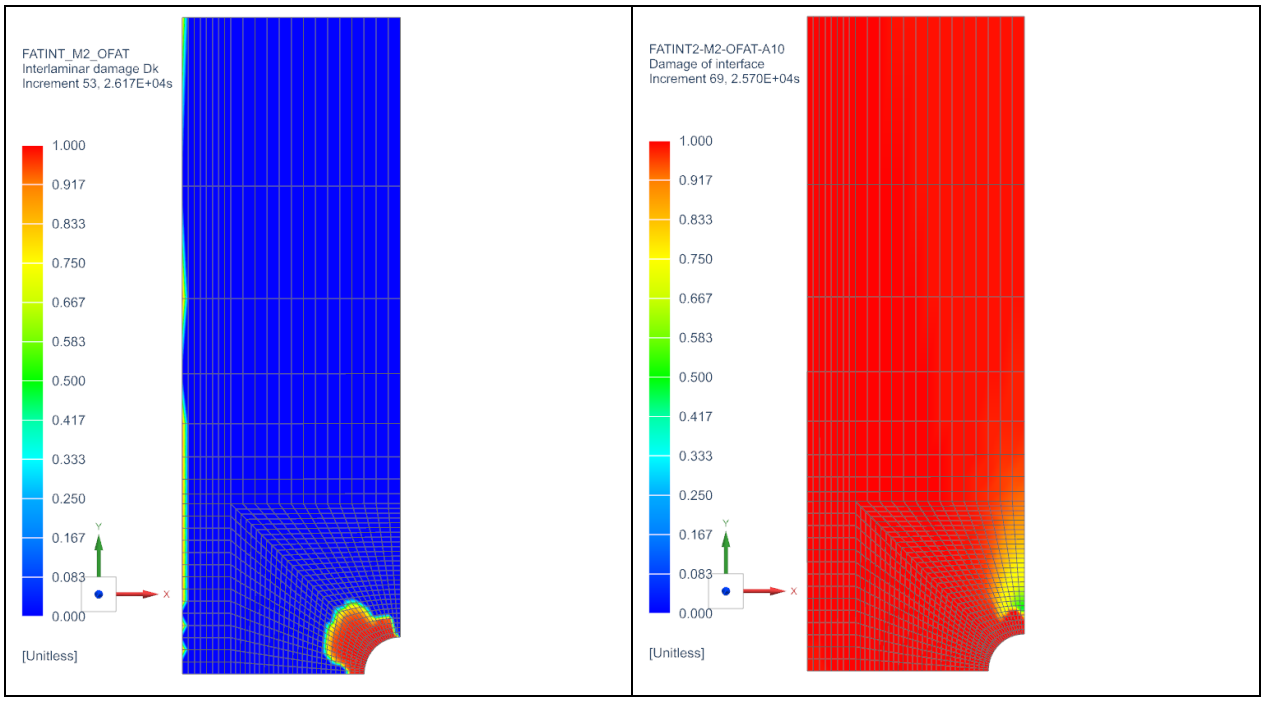

Finally, Table 6-10 shows the comparison without and with interaction using material M1 (with stronger cohesive properties than M2) and with α-exponent equal to 0.1. Similar D22 and Dk results are obtained from both simulations. High ply damage D22 is proceed all along the specimen because the simulation was run for a longer number of cycles, letting the ply damage due to fatigue loading develop further. Likewise in Table 6-6 and Table 6-7 there is very small amount of cohesive failure because the cohesive properties used in this case are strong. It can be observed that the effect of D22 on the reaction of the apparent stiffness of the interface is delayed due to a low α-exponent. This is in agreement with the relation represented in Figure 6-13. Even though, the resultant damage of the interface is increased with respect to the simulation without interaction, using low α-exponent might lead to non-conservative results.

Table 6-10. FATINT-M1-OFAT and FATINT2-M1-OFAT-A01

Relative displacement in Y direction (global frame)	
FATINT-M1-OFAT	FATINT2-M1-OFAT-A01

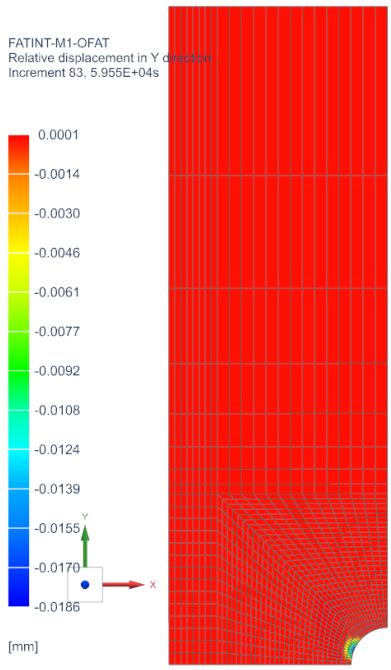

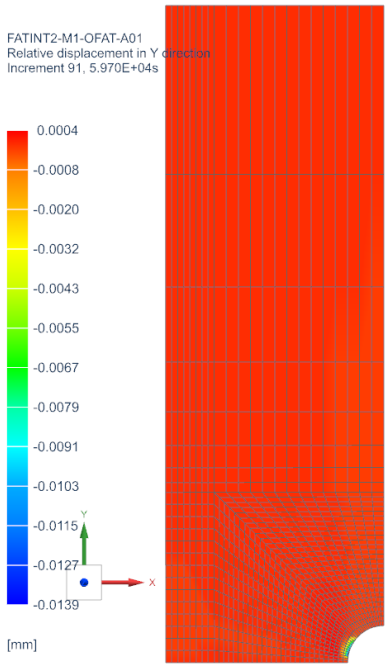

Matrix damage D22

FATINT-M1-OFAT	FATINT2-M1-OFAT-A01

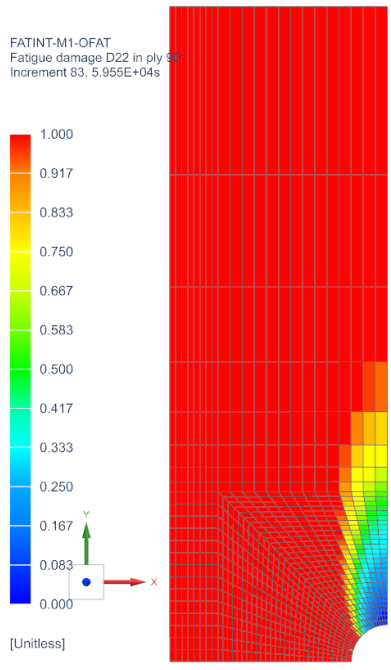

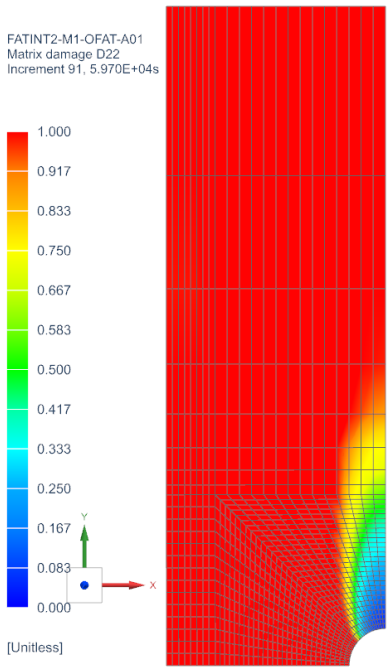

Interlaminar damage Dk

FATINT-M1-OFAT	FATINT2-M1-OFAT-A01

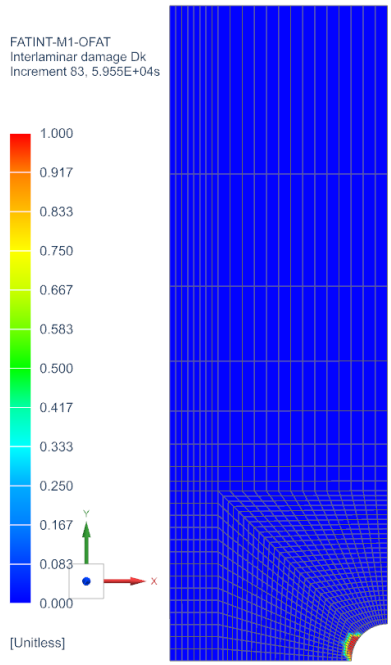

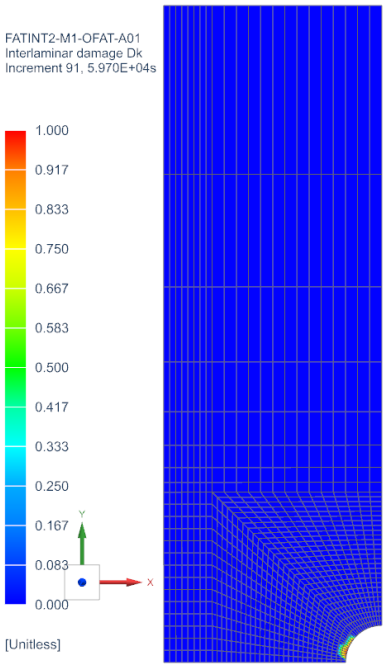

Damage of interface

FATINT-M1-OFAT	FATINT2-M1-OFAT-A01

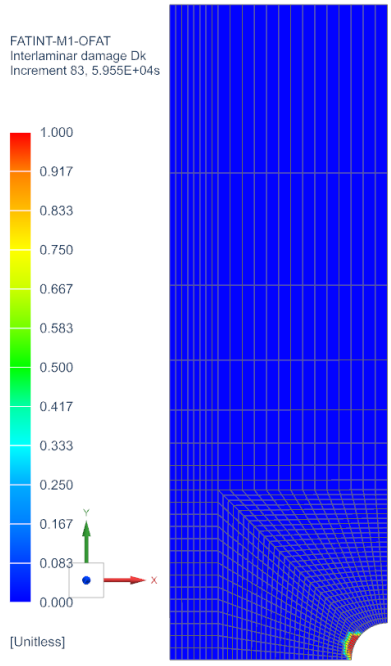

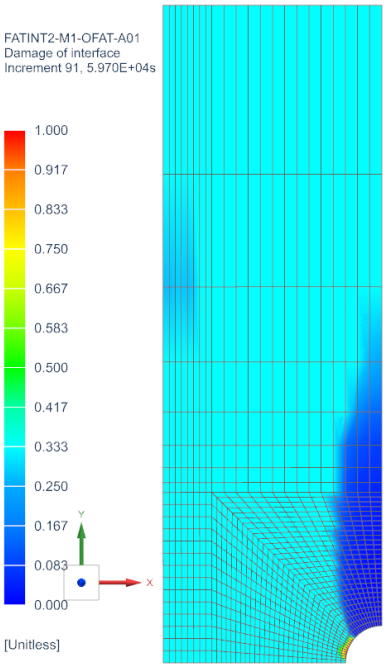

7 Conclusions

The two models for fatigue damage in laminated composite materials developed in WP5 and implemented in the Simcenter Samcef solver during task 5.1 (for inter-laminar damage) and task 5.2 (for intra-laminar damage) have been coupled. To this end, and interaction criterion and a shared cycle jump approach have been developed.

The existing modelling approaches in the literature that aim to capture the effect of matrix cracking in delamination initiation have been revised. From the review, it is concluded that some further investigation is required, especially in the case of fatigue loading. If a combination of a CDM to model damage at the ply region and a CZM to model damage at the interface is used, an interaction between the two independent models is needed. Otherwise, the local homogenization of the stress field in the CDM prevents that a delamination originates as a consequence of the presence of matrix cracks.

In this work, a relation between the ply damage and the reduction of the apparent stiffness of the interface is postulated. This enables to create a delamination (complete reduction of interfacial stiffness) at those regions with high intra-laminar damage. This occurs independently of the evolution of the inter-laminar damage due to cohesive failure. Thus, the stiffness of the interface can be reduced solely due to in-plane stresses. This would never occur if no interaction was defined. The reduction of the interface stiffness creates an interfacial pre-crack that can be crucial if eventually some out-of-plane loading is applied since it can dramatically reduce the delamination resistance of the structure.

The whole modelling approach has been implemented in the Simcenter Samcef solver. To verify the implementation, a unit test consisting on two plies with one element per ply and an interface element joining the two plies has been analysed. The performance of the developed formulation is shown in an open hole specimen test run with different material and interaction parameters. The results show that the fracture behaviour of the specimen corresponds to the one for which the interaction was designed for (explained in Section 4.1).

8 References

1. Takeda, N. & Ogihara, S. In situ observation and probabilistic prediction of microscopic failure processes in CFRP cross-ply laminates. *Compos. Sci. Technol.* **52**, 183–195 (1994).
2. Takeda, N. & Ogihara, S. Initiation and growth of delamination from the tips of transverse cracks in CFRP cross-ply laminates. *Compos. Sci. Technol.* **52**, 309–318 (1994).
3. Garrett, K. W. & Bailey, J. E. Multiple transverse fracture in 90 cross-ply laminates of a glass fibre-reinforced polyester. *J. Mater. Sci.* **12**, 157–168 (1977).
4. Berthelot, J.-M. Transverse cracking and delamination in cross-ply glass-fiber and carbon-fiber reinforced plastic laminates: static and fatigue loading. *Appl. Mech. Rev.* **56**, 111–147 (2003).
5. Hu, P., Pulungan, D. & Lubineau, G. An enriched cohesive law using plane-part of interfacial strains to model intra/inter laminar coupling in laminated composites. *Compos. Sci. Technol.* **200**, 108460 (2020).
6. Hallett, S. R., Jiang, W.-G., Khan, B. & Wisnom, M. R. Modelling the interaction between matrix cracks and delamination damage in scaled quasi-isotropic specimens. *Compos. Sci. Technol.* **68**, 80–89 (2008).
7. Carraro, P. A., Maragoni, L. & Quaresimin, M. Characterisation and analysis of transverse crack-induced delamination in cross-ply composite laminates under fatigue loadings. *Int. J. Fatigue* **129**, 105217 (2019).
8. Pagano, N. J. & Schoeppner, G. A. Delamination of polymer matrix composites: problems and assessment. (2000).
9. Kashtalyan, M. & Soutis, C. Analysis of composite laminates with intra-and interlaminar damage. *Prog. Aerosp. Sci.* **41**, 152–173 (2005).
10. Sun, X. C. & Hallett, S. R. Barely visible impact damage in scaled composite laminates: Experiments and numerical simulations. *Int. J. Impact Eng.* **109**, 178–195 (2017).
11. Wisnom, M. R. & Hallett, S. R. The role of delamination in strength, failure mechanism and hole size effect in open hole tensile tests on quasi-isotropic laminates. *Compos. Part A Appl. Sci. Manuf.* **40**, 335–342 (2009).
12. Krueger, R. Virtual crack closure technique: history, approach, and applications. *Appl. Mech. Rev.* **57**, 109–143 (2004).
13. Krueger, R. The virtual crack closure technique for modeling interlaminar failure and delamination in advanced composite materials. in *Numerical modelling of failure in advanced composite materials* 3–53 (Elsevier, 2015).
14. Griffits, A. A. The phenomena of rupture and flow in solids. *Philos. Trans. R. Soc. A Math. Phys. Eng. Sci.* **221**, 167–198 (1920).
15. Dugdale, D. S. Yielding of steel sheets containing slits. *J. Mech. Phys. Solids* **8**, 100–104 (1960).
16. Barenblatt, G. I. The mathematical theory of equilibrium cracks in brittle fracture. *Adv. Appl. Mech.* **7**, 55–129 (1962).
17. O'brien, T. K. Characterization of delamination onset and growth in a composite laminate. in *Damage in composite materials: basic mechanisms, accumulation, tolerance, and characterization* (ASTM International, 1982).
18. Schellekens, J. C. J. & De Borst, R. A non-linear finite element approach for the analysis of mode-I free edge delamination in composites. *Int. J. Solids Struct.* **30**, 1239–1253 (1993).
19. Camanho, P. P., Davila, C. G. & De Moura, M. F. Numerical simulation of mixed-mode progressive delamination in composite materials. *J. Compos. Mater.* **37**, 1415–1438 (2003).

20. Turon, A., Camanho, P. P., Costa, J. & Renart, J. Accurate simulation of delamination growth under mixed-mode loading using cohesive elements: definition of interlaminar strengths and elastic stiffness. *Compos. Struct.* **92**, 1857–1864 (2010).

21. Sun, X. C., Wisnom, M. R. & Hallett, S. R. Interaction of inter-and intralaminar damage in scaled quasi-static indentation tests: Part 2–Numerical simulation. *Compos. Struct.* **136**, 727–742 (2016).

22. Daum, B., Feld, N., Allix, O. & Rolfes, R. A review of computational modelling approaches to compressive failure in laminates. *Compos. Sci. Technol.* **181**, 107663 (2019).

23. Higuchi, R., Okabe, T. & Nagashima, T. Numerical simulation of progressive damage and failure in composite laminates using XFEM/CZM coupled approach. *Compos. Part A Appl. Sci. Manuf.* **95**, 197–207 (2017).

24. Vigueras, G. *et al.* An XFEM/CZM implementation for massively parallel simulations of composites fracture. *Compos. Struct.* **125**, 542–557 (2015).

25. Chen, B. Y., Pinho, S. T., De Carvalho, N. V, Baiz, P. M. & Tay, T. E. A floating node method for the modelling of discontinuities in composites. *Eng. Fract. Mech.* **127**, 104–134 (2014).

26. Chen, B. Y., Tay, T. E., Pinho, S. T. & Tan, V. B. C. Modelling the tensile failure of composites with the floating node method. *Comput. Methods Appl. Mech. Eng.* **308**, 414–442 (2016).

27. Zhi, J. & Tay, T.-E. Explicit modeling of matrix cracking and delamination in laminated composites with discontinuous solid-shell elements. *Comput. Methods Appl. Mech. Eng.* **351**, 60–84 (2019).

28. Zhi, J., Chen, B.-Y. & Tay, T.-E. Geometrically nonlinear analysis of matrix cracking and delamination in composites with floating node method. *Comput. Mech.* **63**, 201–217 (2019).

29. Le, M. Q., Bainier, H., Néron, D., Ha-Minh, C. & Ladevèze, P. On matrix cracking and splits modeling in laminated composites. *Compos. Part A Appl. Sci. Manuf.* **115**, 294–301 (2018).

30. Moës, N., Dolbow, J. & Belytschko, T. A finite element method for crack growth without remeshing. *Int. J. Numer. Methods Eng.* **46**, 131–150 (1999).

31. Belytschko, T., Gracie, R. & Ventura, G. A review of extended/generalized finite element methods for material modeling. *Model. Simul. Mater. Sci. Eng.* **17**, 43001 (2009).

32. Ladeveze, P. & LeDantec, E. Damage modelling of the elementary ply for laminated composites. *Compos. Sci. Technol.* **43**, 257–267 (1992).

33. Allix, O. & Ladevèze, P. Interlaminar interface modelling for the prediction of delamination. *Compos. Struct.* **22**, 235–242 (1992).

34. Marsal, D., Ladevèze, P. & Lubineau, G. On the out-of-plane interactions between ply damage and interface damage in laminates. in *IUTAM Symposium on Multiscale Modelling of Damage and Fracture Processes in Composite Materials* 97–104 (Springer, 2006).

35. Degrieck and, J. & Van Paepegem, W. Fatigue damage modeling of fibre-reinforced composite materials. *Appl. Mech. Rev.* **54**, 279–300 (2001).

36. Carreras, L. *et al.* A simulation method for fatigue-driven delamination in layered structures involving non-negligible fracture process zones and arbitrarily shaped crack fronts. *arXiv* https://arxiv.org/abs/1905.05000 (2019).

37. Turon, A., Costa, J., Camanho, P. P. & Dávila, C. G. Simulation of delamination in composites under high-cycle fatigue. *Compos. Part A Appl. Sci. Manuf.* **38**, 2270–2282 (2007).

38. Bak, B. L. V., Turon, A., Lindgaard, E. & Lund, E. A simulation method for high-cycle fatigue-driven delamination using a cohesive zone model. *Int. J. Numer. Methods Eng.* **106**, 163–191 (2016).

39. Harper, P. W. & Hallett, S. R. A fatigue degradation law for cohesive interface elements–development and application to composite materials. *Int. J. Fatigue* **32**, 1774–1787 (2010).

40. Bak, B. L. V., Sarrado, C., Turon, A. & Costa, J. Delamination Under Fatigue Loads in Composite Laminates: A Review on the Observed Phenomenology and Computational Methods. *Appl. Mech. Rev.* **66**, 060803 (2014).

41. May, M. & Hallett, S. R. A combined model for initiation and propagation of damage under fatigue loading for cohesive interface elements. *Compos. Part A Appl. Sci. Manuf.* **41**, 1787–1796 (2010).

42. May, M. & Hallett, S. R. An advanced model for initiation and propagation of damage under fatigue loading–part I: Model formulation. *Compos. Struct.* **93**, 2340–2349 (2011).

43. Van Paepegem, W. & Degrieck, J. A new coupled approach of residual stiffness and strength for fatigue of fibre-reinforced composites. *Int. J. Fatigue* **24**, 747–762 (2002).

44. Van Paepegem, W. *Development and finite element implementation of a damage model for fatigue of fibre-reinforced polymers.* (GUAP, 2002).

45. Carreras, L. *et al.* A simulation method for fatigue-driven delamination in layered structures involving non-negligible fracture process zones and arbitrarily shaped crack fronts. *Compos. Part A Appl. Sci. Manuf.* **122**, 107–119 (2019).

46. Carreras, L., Bak, B. L. V., Turon, A., Renart, J. & Lindgaard, E. Point-wise evaluation of the growth driving direction for arbitrarily shaped delamination fronts using cohesive elements. *Eur. J. Mech. A/Solids* **72**, 464–482 (2018).

47. Benzeggagh, M. L. & Kenane, M. Measurement of mixed-mode delamination fracture toughness of unidirectional glass/epoxy composites with mixed-mode bending apparatus. *Compos. Sci. Technol.* **56**, 439–449 (1996).

48. Turon, A., Camanho, P. P., Costa, J. & Dávila, C. G. A damage model for the simulation of delamination in advanced composites under variable-mode loading. *Mech. Mater.* **38**, 1072–1089 (2006).

49. Turon, A., González, E. V., Sarrado, C., Guillamet, G. & Maimí, P. Accurate simulation of delamination under mixed-mode loading using a cohesive model with a mode-dependent penalty stiffness. *Compos. Struct.* **184**, 506–511 (2018).

50. Carreras, L., Lindgaard, E., Renart, J., Bak, B. L. V. & Turon, A. An evaluation of mode-decomposed energy release rates for arbitrarily shaped delamination fronts using cohesive elements. *Comput. Methods Appl. Mech. Eng.* **347**, 218–237 (2019).

51. Blanco, N., Gamstedt, E. K., Asp, L. E. & Costa, J. Mixed-mode delamination growth in carbon–fibre composite laminates under cyclic loading. *Int. J. Solids Struct.* **41**, 4219–4235 (2004).

52. ISO14125:1998. Fibre-reinforced plastic composites — Determination of flexural properties. *Int. Organ. Stand.* (2004).

53. Schindelin, J. *et al.* Fiji: an open-source platform for biological-image analysis. *Nat. Methods* **9**, 676–682 (2012).

54. Potter, K., Khan, B., Wisnom, M., Bell, T. & Stevens, J. Variability, fibre waviness and misalignment in the determination of the properties of composite materials and structures. *Compos. Part A Appl. Sci. Manuf.* **39**, 1343–1354 (2008).

55. Peerlings, R. H. J. d, De Borst, R., Brekelmans, W. A. M. & Geers, M. G. D. Localisation issues in local and nonlocal continuum approaches to fracture. *Eur. J. Mech.* **21**, 175–189 (2002).